UNIVERSITÀ DEGLI STUDI DI PADOVA

UNIVERSITÀ DEGLI STUDI DI PADOVA

DIPARTIMENTO DI FISICA E ASTRONOMIA 'GALILEO GALILEI'

SCUOLA DI DOTTORATO DI RICERCA IN FISICA

CICLO XXVII

3D physics, turbulence and transport in the plasma boundary of RFX-mod

Direttore della Scuola: Ch.mo Prof. Andrea VITTURI

Supervisor: Ch.mo Prof. Piero MARTIN

Co-supervisor: Dott. Emilio MARTINES

Co-supervisor: Dott. Nicola VIANELLO

Dottoranda: Cristina REA

Contents

Abstract

The increasing demand for new energy production has become the constant *leitmotif* of the society we live in. The impossibility of meeting such request in an economically feasible and environmentally friendly manner within the existing portfolio of options is now a global self-awareness. The International Energy Agency has been thoroughly documenting through its reports during the last years that the known reserves of natural gas and oil will be exhausted in decades, due to overpopulation and increasing energy demand. Consequently, a crucial issue will soon concern supply problems. This is where the research on fusion as energy source enters the picture.
In order to demonstrate the feasibility of fusion as an energy source, the international scientific community has devoted countless efforts to the research on controlled thermonuclear fusion. The main and biggest experiment under construction, ITER, is the result of the cooperation among many countries throughout the world and it will be a test bench for fusion physics and fusion engineering.
Among the different magnetic configurations suitable for fusion devices, the reversed-field pinch has demonstrated to be an excellent tool for plasma physics studies, although it is not accounted as a viable device for commercial energy production.
The RFX-mod experiment hosted by Consorzio RFX in Padova is the biggest RFP device in the world. The research activity that will be presented in this thesis has been developed mainly at RFX-mod in Padova but has also involved the participation to an experimental campaign on the COMPASS tokamak in Prague.

The research activity that will be presented in this thesis focuses on the characterization of 3D effects on transport mechanisms at the edge region of fusion plasmas in RFX-mod. The device is highly versatile: it can be operated both in reversed-field pinch and in tokamak magnetic configuration. A detailed description of transport properties

at the plasma edge in both configurations will be given in the development of the thesis. The approach that will be followed can be described in terms of a twofold itinerary shared between the investigation of electrostatic fluctuations of transport properties through insertable probes and the study of magnetic topology modifications due to spontaneous 3D processes.

The thesis is organized as follows:

Part I, Introduction.
In the first part of the thesis, all the background information needed for the development of the work will be introduced. In **chapter 1** the concept of plasma and fusion physics will be discussed together with a detailed description of the two magnetic configurations for fusion devices relevant for analyses: reversed-field pinch (RFP) and tokamak. In **chapter 2** the RFP dynamics will be described in details by introducing Taylor relaxation theory and the two main topologies also experimentally observed: the Single Helicity (SH) and the Multiple Helicity (MH) states. Then, RFX-mod edge region will be specifically described and the main tools used in the analyses will be introduced. The chapter will close with the introduction of a comparison between RFP and tokamak's edge region through the analogy of a common 3D structure when external magnetic perturbations are applied.

Part II, Transport analysis.
In **chapter 3** the two experimental configurations in which RFX-mod operates will be presented. The insertable *U-probe* used in the experiments will be described together with the theory upon which the collection of measurements relies. The investigation of electrostatic fluctuations of transport properties at the edge will be discussed. Studies on transport mechanism around different topological regions in presence of an externally applied magnetic perturbation will be shown for both reversed-field pinch and tokamak configuration in the RFX-mod device.

Part III, Topology analysis.
The study of magnetic topology modifications develops through analyses of spontaneous magnetic reconnection events in reversed-field pinch magnetic configuration. In **chapter 4** reconnection models will be briefly discussed. Then, *crash* events in RFX-mod will be presented and the adopted analysis technique will be thoroughly explored. In the second part of the chapter the *ion energy analyzer* will be described together

with its application in measurements of ion temperature profile in COMPASS tokamak and in RFX-mod.

Part IV, Conclusions.
In **chapter 5** the results of the thesis are collected and discussed. In conclusion, a section entitled *Summary and future perspectives* is added where the main results are tautly summarized in view of future perspectives of research.

Part V, Appendixes.
In **Appendix A** a detailed description of *MagnetoHydroDynamics* framework for plasma physics is given. In **Appendix B** transport equations will be treated in details.

Riassunto

Il crescente aumento nella richiesta di produzione energetica è diventato un costante *leitmotif* che caratterizza la società in cui viviamo. L'impossibilità di riuscire a soddisfare tali richieste sfruttando opzioni già esistenti che siano economicamente vantaggiose ed al contempo rispettino l'ambiente, è ormai una consapevolezza globalmente diffusa. La International Energy Agency ha esaustivamente documentato attraverso i suoi report annuali che le riserve di gas naturale e combustibile fossile si esauriranno nel giro di qualche decade a causa della sempre più crescente richiesta di energia. Come provvedere a soddisfare le esigenze energetiche di una popolazione mondiale in continuo aumento diventerà ben presto un problema critico. È all'interno di questo quadro globale che entra in gioco la ricerca sulla fusione come risorsa energetica.
Al fine di poter dimostrare la sfruttabilità della fusione nucleare quale risorsa energetica, la comunità scientifica internazionale ha da anni continuato ad investire nella ricerca sulla fusione termonucleare controllata. Ad oggi è nelle fasi finali di costruzione il più grande esperimento che coinvolga trasversalmente ricercatori da ogni parte del mondo. L'esperimento è denominato ITER (International Thermonuclear Experimental Reactor) e rappresenterà un banco di prova per la fisica della fusione e l'ingegneria. Tra le possibili configurazioni magnetiche adottabili sperimentalmente in una macchina da fusione, quella a campo magnetico rovesciato si è rivelata essere un eccellente strumento per studiare la fisica del plasma e le innumerevoli sfide scientifiche che essa pone. Tuttavia, per svariati motivi non è previsto l'utilizzo di tale configurazione in un reattore a fusione che produca energia a fini commerciali.
L'esperimento RFX-mod ospitato presso il Consorzio RFX a Padova è il *reversed-field pinch* (RFP) più grande al mondo. L'attività di ricerca che verrà presentata in questo lavoro di tesi è stata svolta principalmente a Padova su RFX-mod ma ha anche previsto e contemplato la partecipazione ad una campagna sperimentale sul tokamak COMPASS a Praga.

L'attività di ricerca che verrà presentata in questa tesi si concentra sulla caratterizzazione degli effetti 3D sui meccanismi di trasporto nella regione più esterna del plasma di RFX-mod. La macchina risulta essere estremamente versatile in quanto sono possibili operazioni in configurazione a campo rovesciato e in configurazione tokamak. Nello svolgimento della tesi verrà fornita una descrizione dettagliata delle proprietà di trasporto al bordo del plasma in entrambe le configurazioni magnetiche. L'approccio che verrà seguito può essere descritto in termini di un duplice percorso condiviso tra l'investigazione delle fluttuazioni elettrostatiche delle proprietà di trasporto effettuato attraverso l'utilizzo di sonde inseribili nel plasma e lo studio dei cambiamenti della topologia magnetica dovuti a meccanismi spontanei di tipo 3D.

La tesi viene così organizzata:

Parte I, Introduzione.
Nella prima parte della tesi verranno introdotte tutte le nozioni di base utili allo svolgimento del lavoro. Nel **capitolo 1** sarà discusso il concetto di plasma e fisica della fusione assieme ad una descrizione dettagliata delle due configurazioni magnetiche rilevanti ai fini delle analisi effettuate: la configurazione reversed-field pinch (RFP) e tokamak. Nel **capitolo 2** la dinamica di un RFP verrà dettagliatamente descritta attraverso la teoria di Taylor. Inoltre verranno discussi gli stati a singola e multipla elicità (stati SH e MH), caratteristici della dinamica di un RFP. Successivamente verrà descritta la regione più esterna del plasma di RFX-mod, anche attraverso gli strumenti principali utilizzati nelle analisi effettuate. Il capitolo si concluderà quindi con l'introduzione di una analogia, che sarà dominante in tutto il corpo della tesi, tra la regione esterna di un plasma di tipo RFP e di uno di tipo tokamak durante esperimenti che prevedano l'applicazione di perturbazioni magnetiche.

Parte II, Analisi di trasporto.
Il **capitolo 3** si apre con la presentazione delle due configurazioni sperimentali adottate per RFX-mod ai fini delle analisi di trasporto. Negli esperimenti è stata utilizzata la sonda inseribile *U-probe*, che verrà descritta successivamente assieme alla teoria su cui si basano le misure da essa raccolte. Verranno quindi discussi i risultati derivanti dall'investigazione delle fluttuazioni elettrostatiche nella regione di bordo del plasma. Verranno di seguito presentati gli studi sui meccanismi di trasporto in differenti regioni topologiche in presenza di una perturbazione magnetica esternamente applicata. Tali

risultati verranno mostrati per esperimenti condotti su RFX-mod sia in configurazione reversed-field pinch che in configurazione tokamak.

Parte III, Analisi topologiche.
Lo studio dei cambiamenti della topologia magnetica si sviluppa attraverso l'analisi di eventi spontanei di riconnessione magnetica in configurazione a campo rovesciato. Nel **capitolo 4** verranno inizialmente discussi alcuni modelli di riconnessione magnetica. Verranno quindi presentati i cosiddetti eventi di *crash* all'interno di RFX-mod e verrà dettagliatamente descritta la tecnica di analisi adottata. Nella seconda parte del capitolo verranno descritti gli esperimenti effettuati sul tokamak COMPASS e su RFX-mod sfruttando un'altra sonda inseribile che ha lo scopo di analizzare il profilo di temperatura ionica.

Parte IV, Conclusioni.
Nel **capitolo 5** sono raccolti e discussi i risultati della tesi. Infine, viene fornita una sezione in cui i principali risultati sono trattati sinteticamente insieme ai problemi rimasti aperti in vista di future prospettive di ricerca.

Parte V, Appendici.
In **Appendice A** è possibile trovare una descrizione dettagliata del formalismo della *Magnetoidrodinamica* mentre in **Appendice B** vengono trattate in dettaglio le equazioni per il trasporto utili ai fini della tesi.

Part I

Introduction

Chapter 1

Magnetic confinement and fusion devices

This first chapter aims at introducing fusion physics and fusion devices.
The *plasma* is a fluid made of partially or fully ionized particles that exhibit a collective behavior. A fully ionized plasma is a collection of positively charged ions and negatively charged electrons obtained by heating a gas to very high temperatures or running a current discharge through it. Plasma dynamics is hence dominated by a collective behavior with many degrees of freedom due to long-range electromagnetic interactions and global charge quasi-neutrality. Plasma is the most abundant form of ordinary matter in the Universe, most of which is in the rarefied intergalactic regions, particularly the intracluster medium, and in stars.
The framework used to describe plasma's equilibrium and stability is *MagnetoHydroDynamics* (MHD): the fundamental concept behind MHD is that magnetic fields can induce currents in a moving conductive fluid, which in turn creates forces on the fluid and also changes the magnetic field itself. The set of equations that describe MHD are a combination of fluid dynamics equations and Maxwell's equations of electromagnetism. These differential equations have to be solved simultaneously, either analytically (under strict assumptions) or numerically[1].

In the first section we are going to describe the reactions at the basis of thermonuclear fusion and the main mechanisms that let obtain plasma confinement in laboratories. Then we will focus on magnetic confinement and will depict the two configurations for

[1] A more detailed description of MHD can be found in Appendix A.

fusion devices that will be the environment for the development of the thesis. Eventually, we will accurately describe RFX-mod, the reversed-field pinch device operating in Padova.

1.1 Plasma confinement and thermonuclear fusion

Apart from the gravitational confinement in stars, there are basically two methods to obtain plasma confinement on Earth: *magnetic* and *inertial confinement*.

- *Magnetic confinement* fusion will be the framework of this thesis and it is based on the exploitation of magnetic fields to confine matter in the plasma state. Thanks to the Lorentz effect, that regulates the motion of charged particles in magnetic fields, it is possible to reach relatively long confinement times by using magnetic fields in a closed geometry, like in a torus.
- In *inertial confinement* fusion experiments ignition is reached by compressing and heating the fuel, with energy delivered to the outer layer of a solid target of deuterium and tritium using high-energy beams of laser light, electrons or ions. The heated outer layer explodes outward, producing a reaction force against the remainder of the target, accelerating it inwards, compressing the target. This process is designed to create shock waves that travel inward through the target. A sufficiently powerful set of shock waves can compress and heat the fuel at the center so much that fusion reactions occur. The energy released by these reactions will then heat the surrounding fuel, and if the heating is strong enough it can begin to undergo fusion. First results are coming in this direction [1] but the main approach used to reach plasma confinement is without any doubt that of magnetic confinement.

The fuel for fusion reactions consists of a mixture of deuterium and tritium. The main reactions involving these isotopes are reported below, together with their cross section as a function of the kinetic energy of incident particle in Figure 1.1:

$$\begin{aligned} D + D &\rightarrow {}^3He + n + 3.27\ MeV \\ D + D &\rightarrow T + p + 4.03\ MeV \\ D + {}^3He &\rightarrow \alpha + p + 18.3\ MeV \\ D + T &\rightarrow \alpha + n + 17.6\ MeV \end{aligned}$$

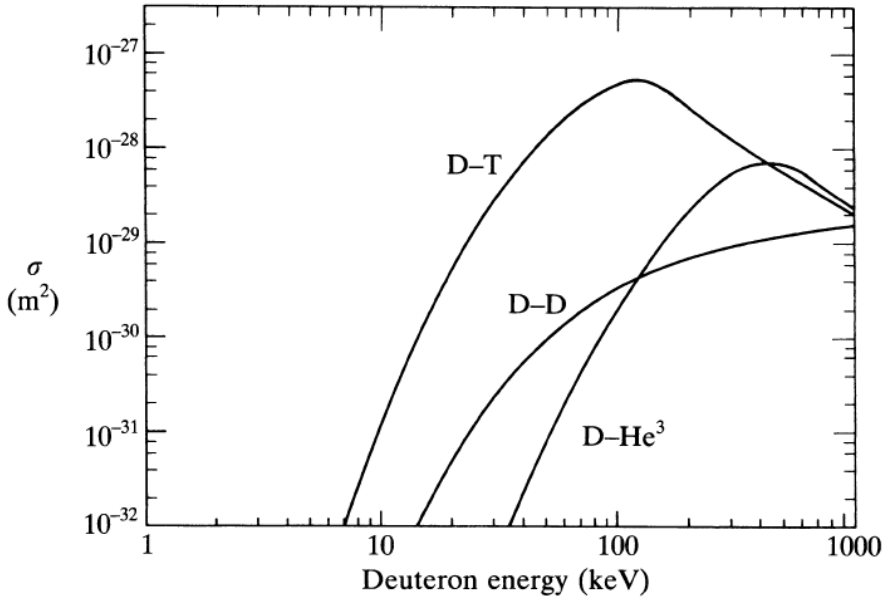

FIGURE 1.1: Cross section of reactions involving deuterium and tritium as a function of deuteron energy.

As we can see, the D-T reaction is preferred to other reactions due to largest fusion cross section, about 5 barns at a center of mass kinetic energy, $E \approx 120\ keV$. High kinetic energies are required in order to overcome the repulsive Coulomb force. Coulomb collisions, which are much more frequent than fusion collisions, also cause the plasma to relax to a Maxwellian distribution function. The combination of a Maxwellian distribution function and the experimentally measured D-T cross section enables one to evaluate the velocity-averaged cross-section $< \sigma v >$ as a function of temperature.

However, when considering a confined plasma characterized by density n, temperature T and a confinement time τ_E, it is important to give the definition of the criterion necessary to describe an *ignition condition*, the one that guarantees the plasma self-sustainement without external heating mechanism. This condition is ensured when power produced by alpha particles balances power loss due to radiation emission (*bremsstrahlung*) and transport processes[2]: $P_b + P_t \leq P_\alpha$ [2], where

$$\begin{aligned} P_b &= \alpha_b n^2 T^{1/2} \\ P_t &= \frac{3nT}{\tau_E} \\ P_\alpha &= \frac{1}{4} < \sigma v > E_\alpha \end{aligned} \tag{1.1}$$

[2]Since α particles are charged reaction products, they stay confined in the plasma and due to collisions contribute with their energy ($E_\alpha = 3.5\ MeV$) to plasma heating.

Eventually, taking explicitly into account all terms in Equation 1.1, the ignition condition is given by [3]:

$$n\tau_E \geq \frac{12T}{< \sigma v > E_\alpha - 4\alpha_b T^{1/2}} \tag{1.2}$$

where $\alpha_b = 5.35 \cdot 10^{-37}\ Wm^3 keV^{-1/2}$ is a constant parameter.

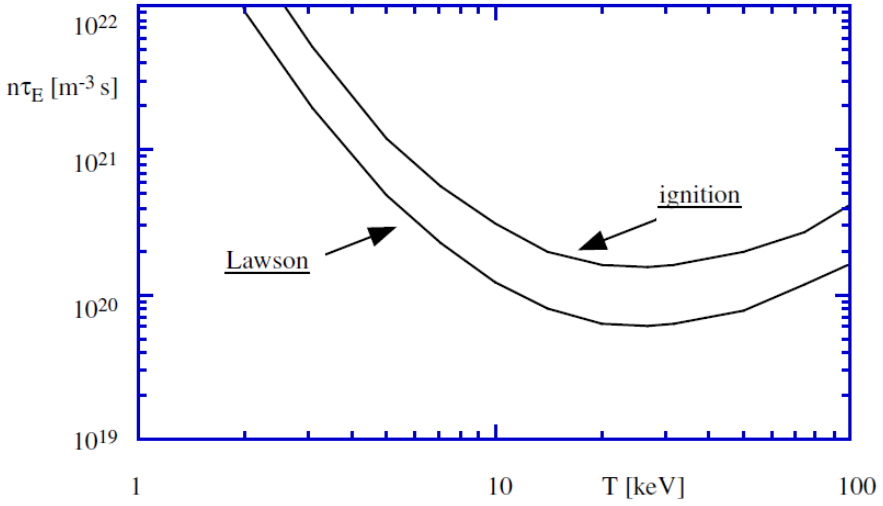

FIGURE 1.2: The minimum $n\tau_E$ curves for which the Lawson's and ignition condition are satisfied. The Lawson's curve refers to an efficiency of $\eta = 30\%$ and has a minimum at $T \approx 20\ keV$.

From Figure 1.1 above, we can see that the minimum of temperature required for ignition is $T \sim 10 - 20\ keV$. At this temperature we can neglect the radiation contribution and the ignition condition can be explicitly written in terms of the *triple product*:

$$nT\tau_E \geq 3 \times 10^{21}\ m^{-3} keV s \tag{1.3}$$

where $n\tau_E$ is identified as the *Lawson parameter*[3]. Equation 1.3 leads to an energy confinement time of $\tau_E = 3\ s$ when $T = 10\ keV$ and $n = 10^{20}\ m^{-3}$.

Different engineering issues influence the optimal working value for the density parameter: for a fusion power plant based on plasma confinement, the unavoidable plasma-wall interaction limits the density to values lower than $10^{20} m^{-3}$ so as to avoid plasma facing components to be targeted by an extreme power flux.

Another problem is the tritium supply. The solution is to breed tritium in the blanket surrounding the region of D-T fusion reactions. The chemical element that is most favorable for breeding tritium is lithium: $n +^6 Li \rightarrow \alpha + T$.

[3]Historically, the Lawson criterion considers also the efficiency of conversion of thermal power deriving from neutrons but completely neglects the possibility of a plasma heating through α particles. Nowadays, a much more refined version of this criterion is used to describe ignition condition.

1.2 Magnetic confinement

Plasma magnetic confinement is based on the exploitation of the effect of the Lorentz force on charged particles in a magnetic field, which gives rise to a spiral motion around the magnetic field lines that in turn results in the particles confinement itself in the direction perpendicular to the field on a space length of the Larmor radius [3]:

$$\rho_L = \frac{mv_\perp}{qB} \tag{1.4}$$

where m is the mass of the particle, q the charge, and $v_\perp$ the component of velocity perpendicular to the magnetic field B. For an ion in a deuterium plasma with a temperature $T_i = 10\ keV$, embedded in a magnetic field of $B = 3\ T$, if we take $v_\perp$ to be the ion thermal velocity $v_{th,i} \sim (T_i/m_i)^{1/2}$, we have $\rho_{L,i} \approx 5 \cdot 10^{-3}\ m$. The Larmor radius of the electrons, assuming $T_e = T_i$ (T_e being the electron temperature), is smaller by a factor $(m_e/m_i)^{1/2} \approx 1.7 \cdot 10^{-2}$.

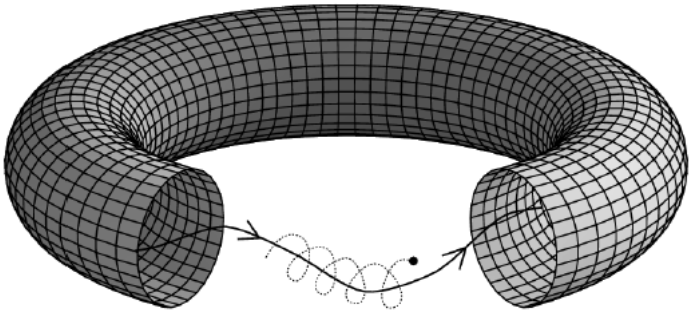

FIGURE 1.3: Spiral motion of a charged particle along a helical magnetic field line in a typical toroidal device.

In order to confine charged particles, an uniform magnetic field is indeed needed: this could be provided by a solenoid but it would confine the plasma only in two directions leaving the possibility of particles losses at the ends of the plasma column. Attempts (mirror, *pinch* configuration) to avoid losses have been made and in the end the most efficient option has revealed to be the use of toroidal devices which force the magnetic field lines to close on themselves, i.e. devices with toroidal geometry: tokamaks, RFPs and stellarators. Nevertheless, this toroidal magnetic field is not uniform since varies with $1/R$, where R is the torus radius, giving rise to drift motions that overlap with the spiral motion of the charged particles ultimately (vertical charge separation, vertical field formation) leading to a drift motion towards the outside of the torus ($\mathbf{v}_d = \frac{\mathbf{E}\times\mathbf{B}}{B^2}$) that deteriorates the confinement. The solution is to superimpose a *poloidal* magnetic

field to the toroidal one produced by the external coils (see Figure 1.4) that can counteract the toroidal expansion forces.
It is shown [2] that the critical property of the magnetic field required for the toroidal force balance is that the field lines continuously wrap around the torus (like the stripes on a barber pole), property known as *rotational transform* ι.

1.3 Fusion devices

The goal of achieving a confined plasma in a magnetic field can be obtained in various geometries but the quality of this confinement is characterized by different criteria. The following points should be mentioned as essential:

- The ratio of **kinetic plasma pressure** to **magnetic pressure** $\beta = \frac{<p>}{(B^2/(2\mu_0))}$ (where $< >$ is intended as an average over the plasma volume): this number measures the economic efficiency of the confinement since the fusion power output roughly scales as p^2 [2] and B is the magnetic field, externally provided. Usually, β is limited by the occurrences of magnetohydrodynamic (MHD) instabilities (see Appendix A).
- The **energy confinement time** $\tau_E = W_{pl}/P_{heat}$ is one of the quantities appearing in the *Lawson criterion* (Equation 1.2, $nT\tau_E \geq f(T)$) and characterizes the transport properties of the configuration.

High β and long τ_E are desirable: the product nT should be optimized and this means high pressure and, for given magnetic field, high β. In doing so the *ideal* MHD limit is encountered. It is the limit where the plasma is unstable on Alfvén time scale ($\tau_A \sim 10\ \mu s$), only limited by inertia. In this scenario, the *Troyon limit* is introduced $\beta_{max} \sim I_p/(aB)$ (a is the plasma radius), and it leads to the definition of the *normalized beta* $\beta_N = \frac{\beta}{I_p/(aB)}$: at fixed aB, the shaping of plasma cross-section allows higher plasma currents and higher β.
Another important limit is the *resistive* MHD limit ($\tau_R \sim 100\ ms$, resistive diffusion time, see Equation 4.3). Since temperature should have an optimum value around $20\ keV$, plasma density should be as high as possible: but the density is also limited by disruptions in tokamaks and soft terminations in reversed-field pinches, due to excessive edge cooling. The empirical *Greenwald limit* is established, $n_{Gr} \sim I_p/(\pi a^2)$, so that high plasma currents help to obtain high plasma densities.

One of the main challenges for the realization of an efficiently working fusion device will be to take into account all the aforementioned experimental and physical limits. In the following sections a brief description of two different fusion configurations is given, with a particular stress on the Reversed-Field Pinch (RFP) configuration that is the main environment of the analyses in this thesis.

1.3.1 Magnetic fusion configurations: Tokamak

The word *tokamak* is a transliteration of a Russian word which means *toroidal chamber with magnetic coils* and it is a specific geometrical configuration for plasma confinement, firstly proposed by two Russian physicists, Tamm and Sakharov in 1952. The main components are illustrated in Figure 1.4: helical magnetic field lines span nested surfaces of constant magnetic flux (*flux surfaces*). The plasma is enclosed in a vac-

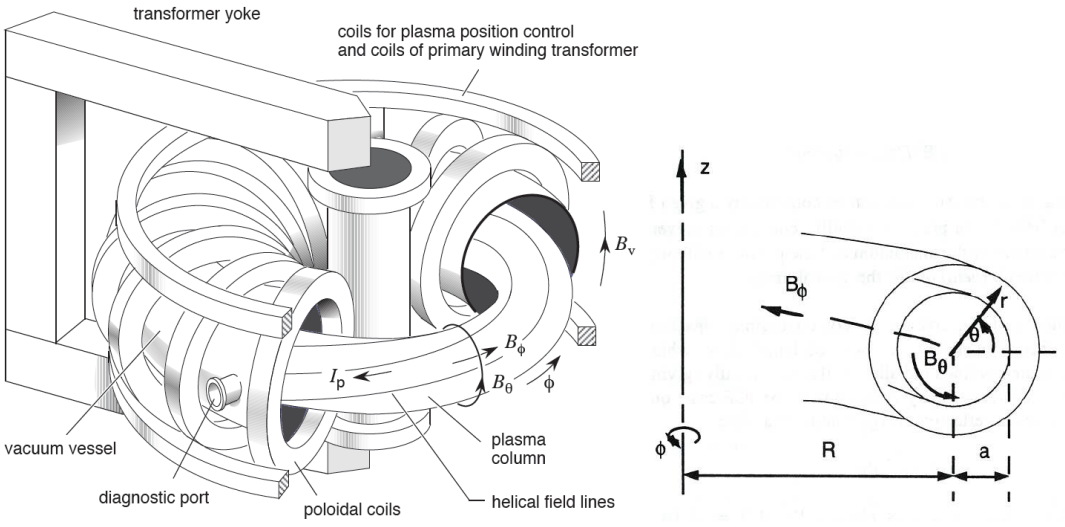

FIGURE 1.4: Typical configuration (left) and coordinate system (right) for a tokamak. Taken from [4].

uum chamber and the axisymmetric toroidal field is provided by poloidal currents in a set of magnetic coils surrounding the plasma. A central solenoid is used to produce a time-varying poloidal magnetic flux which induces a toroidal loop voltage and, due to finite plasma resistivity, a plasma current. Eventually, the plasma acts as the secondary winding of a transformer: the current is ramped up in the primary coil inducing a loop voltage inside the discharge vessel; after breakdown, a toroidal current flows in the plasma (I_P). Heating comes via plasma resistance (*Ohmic heating*) but soon additional heating systems are required (i.e. neutral beam injection, ion or electron

cyclotron resonance and lower hybrid [2]).

The plasma is then subject to a poloidally and radially outward-directed force which results from a finite plasma pressure gradient: this force is balanced by the $\mathbf{j} \times \mathbf{B}$ force acting on the plasma current due to the helical field and an additional vertical field produced by toroidal currents in external conductors (*vertical field coils*). These coils can also create a wide range of plasma shapes but also avoid vertical displacements which eventually cause *disruptions*. Disruption events are the cause of a sudden collapse of the plasma pressure and current with a consequent heat power load on the walls of the plasma chamber that will eventually cause a mechanical stress. Disruptions must be avoided in large experiments and reactors since the large transient forces developed can cause actual physical damage to the structure. The problem of preserving the *Plasma Facing Components* (PFCs), the region where flux surfaces are intercepted by solid elements, leads to the need of separating PFCs from the confined plasma. This separation defines the *Last Closed Flux Surface* (LCFS), also called *separatrix* as the frontier between the well confined core plasma and the *Scrape-Off Layer*, where the plasma interaction takes place. In order to limit the damages to PCFs, two configurations have been created:

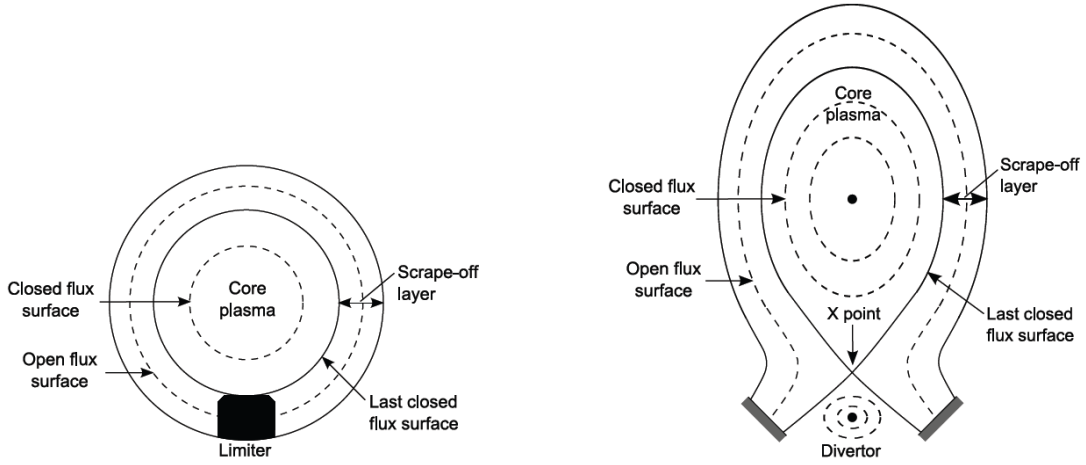

FIGURE 1.5: Poloidal cuts, i.e. cuts by a plane of constant ϕ, showing the limiter (left) and axi-symmetric poloidal divertor (right) configurations [5].

- **limiter** configuration (an example of which is Tore Supra [3]), where the separatrix is directly due to the presence of a material element, called *limiter* (cf. Figure 1.5, left);
- axi-symmetric poloidal **divertor** configuration, where additional coils are used in which axisymmetric toroidal currents flow in order to produce a null in the

poloidal magnetic field, which results in the presence of an X-point (cf. Figure 1.5, right). This offers the possibility to place the material elements further away from the plasma, a better solution in terms of plasma-surface interaction [6].

The divertor tokamak configuration is the one chosen for the main and biggest experiment under construction: **ITER** (International Thermonuclear Experimental Reactor). It is an international project involving worldwide cooperation and an investment of billions of euro. The aim of the scientific community is the demonstration of scientific possibility of obtaining power from fusion. After this step the problem of its technological and economical feasibility will be faced with the **DEMO** experiment. DEMO must be able to demonstrate full steady state operation in a safe, reliable, and maintainable way. While individual components may extrapolate in a straightforward manner, integration of all these components into a working power plant will be a major goal of DEMO.

1.3.2 Magnetic fusion configurations: Reversed-Field Pinch (RFP)

The fundamental characteristic which describes the RFP configuration is the reversal of the toroidal component of the magnetic field at the edge: apart from this, the RFP device can be discussed in analogy to a tokamak device.
The toroidally symmetric vacuum vessel is surrounded by a set of toroidal field coils with a central solenoid which provides the loop voltage necessary to trigger the discharge and hence drive a current in the confined plasma. Therefore, a small toroidal bias field fills the vacuum chamber. A large toroidal current is then ramped up and this compresses both the plasma and the toroidal bias field. In addition, the current raises the plasma temperature by means of ohmic heating. At the end of the current ramp, the toroidal and poloidal magnetic fields within the plasma are of comparable magnitude. However, since most of the toroidal magnetic flux has been trapped and compressed within the plasma, only a small residual toroidal field remains at the plasma edge that spontaneously reverses direction, hence the name "reversed-field" pinch, see left panel of Figure 1.7.

Several RFP experiments exist around the world: the Madison Symmetric Torus (MST) at the University of Wisconsin (USA), the Reversed Field Experiment (RFX) at Consorzio RFX in Padova, the Extrap T2R in Sweden, RELAX in Japan. Several of the

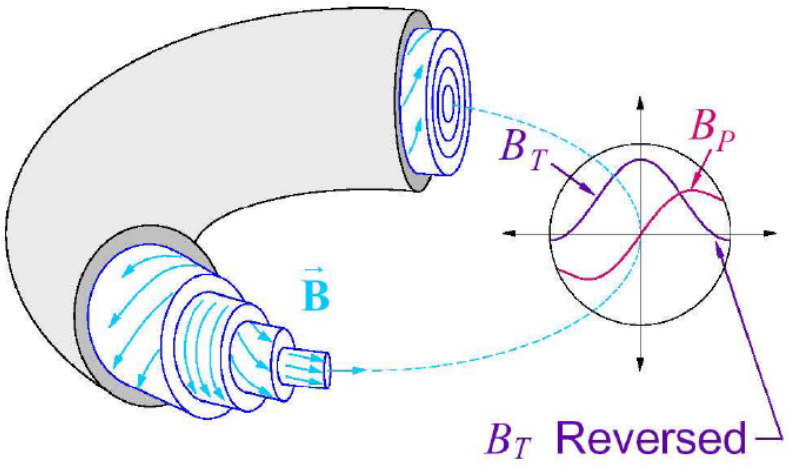

FIGURE 1.6: RFP magnetic field configuration.

main plasma physics problems faced by the RFPs are under investigation by the world-wide RFP community with an eye on the transport problem and on the active control of MHD behavior.

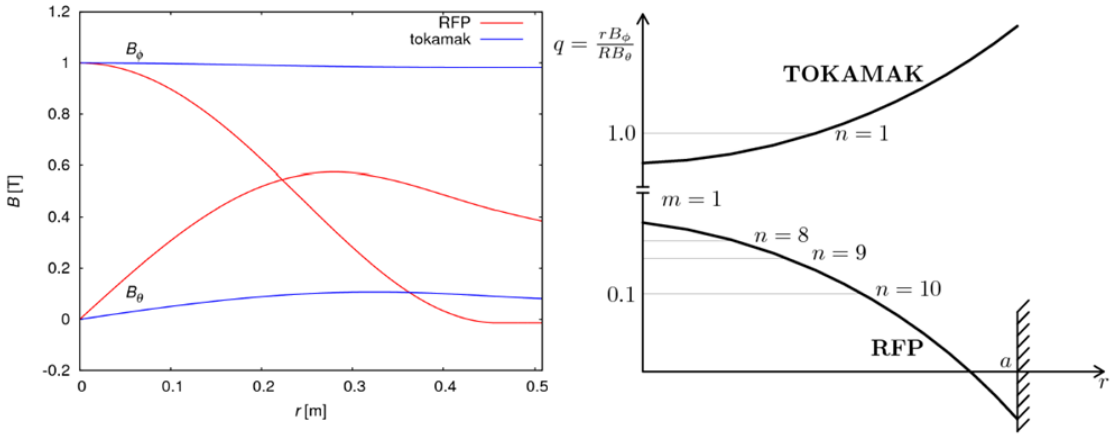

FIGURE 1.7: Left: typical radial profiles for the B_ϕ and B_θ components for the equilibrium of a tokamak and a RFP. Right: typical safety factor profiles and $m = 1$ resonances for tokamak and RFP [2].

As we can see in the left panel of Figure 1.7, the toroidal field vanishes at some radial position called *reversal surface*, after which it reverses its sign. The reversal surface is important since it is the resonant surface of a large spectrum of $m = 0$ modes, *m* being the poloidal mode number while *n* is the toroidal one. Each couple of (m, n) values represents a helical perturbation or mode, supposing we Fourier analyze the

components of the magnetic field[4].
In order to describe the RFP equilibrium it is useful to introduce two dimensionless parameters, the *pinch parameter* Θ and the *reversal parameter* F:

$$\Theta = \frac{B_\theta(a)}{\langle B_\phi \rangle} \qquad F = \frac{B_\phi(a)}{\langle B_\theta \rangle} \tag{1.5}$$

Θ is an indication of how much plasma and the magnetic field are pinched inside the torus, while F measures how much the toroidal field is reversed at the edge.
RFP equilibrium is a solution of Grad-Shafranov equation and turns out to be an axisymmetric equilibrium, since a 2D poloidal cut is enough to describe the entire system. Nevertheless, a 3D modeling of all the toroidal components can further improve the understanding of non-axisymmetric effects, e.g. helical twisting of magnetic flux surfaces.

Comparing RFPs and tokamaks

Both RFPs and tokamaks belong to the class of *toroidal pinch* devices, in which a toroidal current is inductively driven by an external circuit and generates a poloidal magnetic field, while the toroidal one is generated through an external system of coils (tokamak case) or induced by currents flowing in the plasma itself (RFP case).
The two configurations present also some important differences. As can be seen in Figure 1.7, B_θ in a tokamak is one order of magnitude smaller than the toroidal component, while in the RFP case they are comparable in magnitude. This results into very different *safety factor* profiles, cfr. Equation A.16:

$$q(r) = \frac{r B_\phi(r)}{R_0 B_\theta(r)} \tag{1.6}$$

In the tokamak configuration, the condition $q \sim 1$ corresponds to the so-called Kruskal-Shafranov limit, where the configuration is unstable due to a strong $(m = 1, n = 1)$ kink instability rising in the plasma core; in standard tokamak scenarios the q profile increases monotonically with the radial coordinate r, reaching typical values of $q(a) \geq 3$ at the edge, as can be seen in the right panel of Figure 1.7.
The RFP is instead an intrinsically low safety factor device, with $|q| < 1$ over the whole radius; and this does not lead to any disruptive behavior as in tokamaks, thanks to the

[4] A description of MagnetoHydroDynamics basic concepts can be found in Appendix A, in particular the decomposition for a magnetic field component is given in Equation A.17.

combined stabilizing action of the conducting shell and of the large magnetic shear at the plasma edge.
Depending on the q profile, the stability in the toroidal configuration can vary. In Appendix A it is stated that radial positions where $q = m/n$ are those where resonant instabilities can grow. RFPs are usually characterized by a broad spectrum of resonant unstable (m,n) modes with $m = 1$ and $n \geq 1$ and these modes have a clear impact on both the dynamics and transport plasma properties as we will see in next chapters. Also in terms of a reactor vision there are several pros and cons of RFPs with respect to tokamak devices. First, only a very modest set of toroidal field coils is needed to provide the bias field, which is clearly economically advantageous; then, higher values of toroidal current can be reached at the same externally applied magnetic field and this may be sufficient to ohmically heat the RFP plasma to ignition.
The simplicity, efficiency and low cost of ohmic heating compared to alternative external heating mechanisms give to the RFP configuration another important advantage.

Obviously, there are several disadvantages as well which should be considered: first, the low toroidal field at the plasma edge implies a low edge safety factor, which consequently leads to resistive MHD turbulence. This turbulence manifests itself in terms of strongly enhanced energy transport. Eventually, the confinement time τ_E is usually much shorter for a RFP device rather than for a tokamak. Second, since an ohmic transformer cannot operate in DC steady state, some type of external current drive is required (as Oscillating Field Current Drive [2]). Lastly, the presence of a perfectly conducting wall affects substantially the MHD activity in a RFP device. If the wall has a finite conductivity, the plasma becomes subject to resistive wall modes, with the consequence of being clearly unstable to several current-driven modes. This implies that a relatively sophisticated feedback system is required.

1.4 RFX-mod

The *Reversed Field eXperiment modified* (RFX-mod) [7] is the biggest RFP device in the world, it is an upgraded version of the previous RFX and is hosted by Consorzio RFX in Padova.
RFX-mod is operational since 2004 under the management of Consorzio RFX, an association of public and private parties as, CNR, ENEA, University of Padova, Acciaierie Venete S.p.A. and INFN, all within a greater European framework.

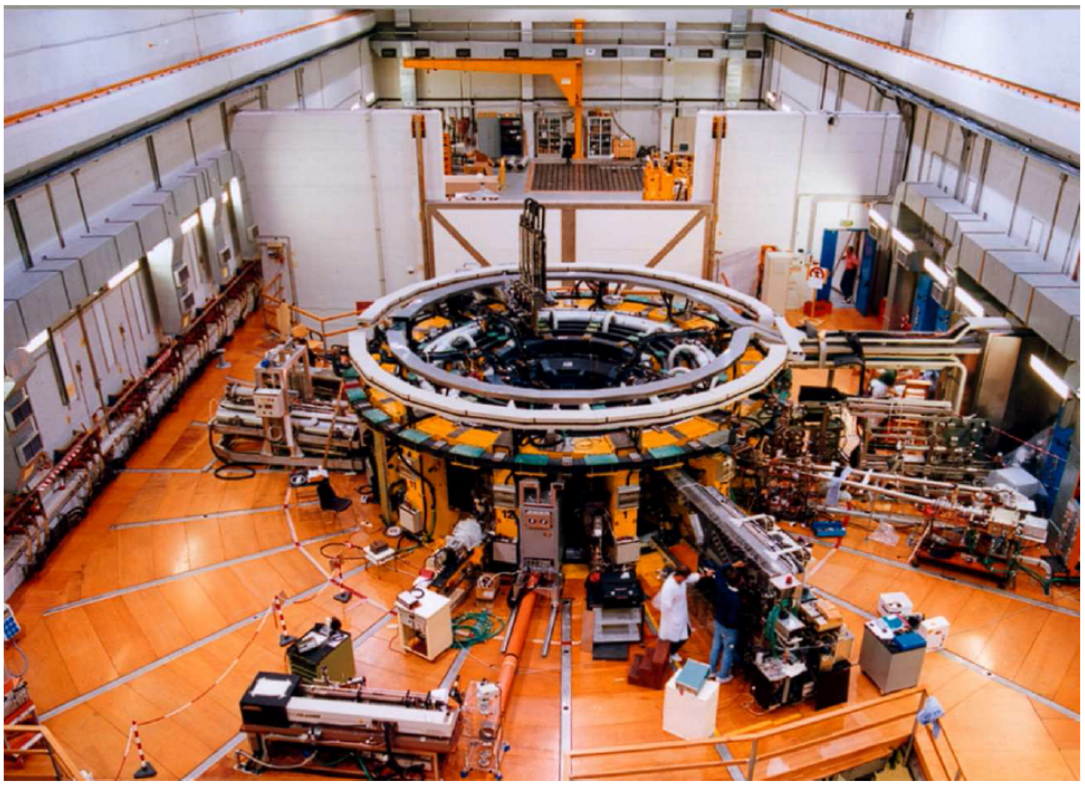

FIGURE 1.8: Photo showing the RFX-mod experiment.

With respect to the original design, some modifications during the years contributed to have significant implementations to the device. As an example: the new feedback control system [7] based on 192 active saddle coils that cover the whole plasma boundary (4 in the poloidal and 48 in the toroidal directions), and the new stabilizing shell whose time constant for penetration of vertical magnetic field ($\tau \sim 50\ ms$) is much shorter than the discharge duration which is now up to $0.5\ s$, with plasma currents up to $2\ MA$.

The plasma of RFX-mod is enclosed in a toroidal vacuum vessel whose internal structure is fully covered by a set of over 2000 graphite tiles. The vessel, a rigid structure made of INCONEL 625, is in turn enclosed in a thin (3 mm thick) stabilizing copper shell and a further structure supports the coils for plasma positioning and feedback control. The shell is intended to stabilize MHD ideal instabilities, having a short penetration time constant for the magnetic field. A 3D view of the overall front-end system of the device is shown in Figure 1.9, while the main physical characteristics of RFX-mod are summarized in Table 1.1.

In RFX-mod, RFP operations at currents greater than $0.6\ MA$ are mainly characterized by *QSH* (quasi-single helicity) *regimes* [8], a special operational condition which

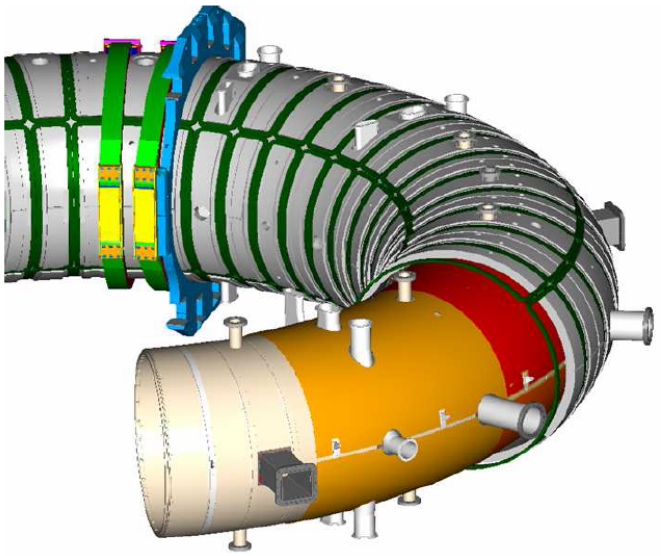

FIGURE 1.9: A 3D view of the technical components in the RFX-mod experiment. The gray external structure is the vacuum vessel, the orange one is the conductive shell, while the blue one represents one of the active control coils.

R_0	2.00 m
a	0.459 m
I_P	$\leq$ 2 MA
B_T	$\leq$ 0.7 T
p_{vacuum}	$\sim 10^{-7}$ Pa
p_{plasma}	10^3 Pa
n_{plasma}	$\sim 5 \cdot 10^{19}\ m^{-3}$
$T_{e,max}$	1.3 keV
$t_{discharge}$	$\leq$ 0.5 s

TABLE 1.1: Main parameters of the RFX-mod experiment in the RFP configuration. R_0 and a represent the major and minor radius of the torus, I_P represents the maximum achievable plasma current, B the maximum magnetic field that coils can create, p_{vacuum} is the pressure inside the vacuum chamber before plasma is created. p_{plasma} represents the typical pressure of the plasma during discharges, n_{plasma} the typical density of ion and electrons, $T_{e,max}$ is the maximum measured electron temperature and $t_{discharge}$ the typical discharge duration.

will be diffusively explained in the next chapter and that allows an amelioration of plasma performances due to an increased resilience to chaos. High current operations and high QSH persistency were made possible by the progressive optimization of the saddle coils feedback control system, which aims at creating a clean boundary analogous to an ideal virtual shell close to the plasma (see [9] and [10]).

The *Clean Mode Control* algorithm operates real-time calculations to correct the *sideband* harmonics coming from the aliasing effects for a discrete system of coils, making

it possible to operate at higher current with better confinement properties. Moreover, the control algorithm has included the possibility to excite a finite reference helicity (useful in experiments with the application of magnetic perturbations of defined helicity).

RFX-mod is a highly versatile device: the machine can be operated also in a tokamak configuration. The magnetic configuration obtained is basically a circular low-field ohmic tokamak, but recently [11] the dynamical control of the plasma column shift and ellipticity has become available within a single discharge with the perspective of performing operations beyond the circular shape also with single or double-null D-shaped plasmas. A new system for control of plasma position and shape has been designed and commissioned.

RFX-mod: the diagnostic system

In this paragraph, a brief description of the most important diagnostics of RFX-mod is given:

- a complete set of *magnetic diagnostics*: these coils are situated between the vacuum vessel and the shell and measure plasma current (by means of 4 Rogowski coils) and concatenated flux variations (using 8 toroidal and 6 poloidal voltage loops) providing information over loop voltage and toroidal flux. In detail, the system is made of 196 bi-axial pick-up coils, distributed along 48 toroidal directions and 4 poloidal directions, which measure toroidal and poloidal components of magnetic fields; 48 x 4 saddle probes, measuring the radial component of the field, coupled to the active control coils. All these pick-up coils are important for the reconstruction of Newcomb's eigenmodes starting from the model [12] and used in this thesis as the input for a *field line tracing code* used to analyze the magnetic topology at the edge;

- the *tomographic system* which reconstructs in a detailed way radiation emission profiles by means of 36 bolometric detectors (which measure the total emission of the plasma) and 78 silicon detectors (which measure the soft-X rays radiation);

- a *Thomson scattering* diagnostic, which provides a 84-point radial profile of electron temperature analyzing the scattering properties of the plasma when a

high power laser beam is injected; the repetition rate is of about 25 ms, for a maximum number of 10 pulses in a discharge;

- an *interferometer*, which measures the electron density averaged along 13 lines of sight. The measurement is performed measuring the phase variation induced in a CO_2 laser beam ($\lambda = 5.4\ \mu m$) that passes through the plasma;
- spectroscopic diagnostics, which measure line intensities of radiation emitted by impurities, in order to calculate their influxes at the edge;
- a *Soft-X Rays multi-filter* diagnostic, used for measuring electron temperature at the center of the plasma by means of comparing SXR emissions measured by differently filtered silicon detectors; it allows a higher time resolution with respect to the Thomson scattering, but with a lower spatial resolution; 4 chords with different filter thicknesses (40 μm, 75 μm, 100 μm, 150 μm) are used, in order to measure temperature in a wider range of emission levels;
- an *integrated system of internal sensors* (ISIS), which includes poloidal and toroidal arrays of 139 magnetic pick-up coils and 97 electrostatic (Langmuir) probes (used to measure and correlate fluctuations of electric and magnetic fields), and 8 calorimetric sensors;
- *insertable probes*: the **U-probe** and the **ExB analyzer**. These probes will be described in full details in Chapter 3 and Chapter 4 due to the direct exploitation related to the analysis performed for the thesis.

Chapter 2

Magnetic topology

The content of this thesis evolves on a dual path. The first one deals with the investigation through insertable probes of the effects on transport properties at the edge deriving from the complex RFP topology: in Chapter 3 a detailed analysis of transport properties at the edge will be presented. The second one regards the study of the consequences that discrete relaxation events have on the topology of a RFP device. Indeed, in Chapter 4 we will see how relaxation events spontaneously arise due to the intrinsic dynamo effect that sustains the RFP configuration, but before that, the aim of this chapter is to give a detailed description of the RFP edge region, in particular of the edge of RFX-mod, developing also a comparison with the structure of tokamak's edge region. The analogy that connects the two configurations consists in a common 3D edge topology of high current (I_p) RFPs on one hand and on the other of tokamaks when external magnetic perturbations are applied.

2.1 Scenario: Taylor relaxation

The theoretical scenario in which the RFP configuration places itself can be at first described through *Taylor relaxation* theory.
The field topology can often change on a macroscopic scale (tearing modes, reconnection events) and the most appropriate physical quantity to describe such changes is the *magnetic helicity*, defined as

$$K = \int_V \mathbf{A} \cdot \mathbf{B} \, d\tau \tag{2.1}$$

where V is the plasma volume, $\mathbf{A}$ the vector potential and $\mathbf{B}$ the magnetic field. Magnetic helicity is a measurement of the plasticity of the field, i.e. its structural topological properties such as twist, shear, linking and braiding. Helicity is conserved in the hypothesis of a null resistivity ($\eta = 0$ describes the ideal MHD limit, see Appendix A), thus for a high conductive plasma ($S \gg 1$, high Lundquist number) helicity is approximately preserved.
In Figure 2.1 we show the system used by Moffatt [13] as illustrative example for the calculation of magnetic helicity.

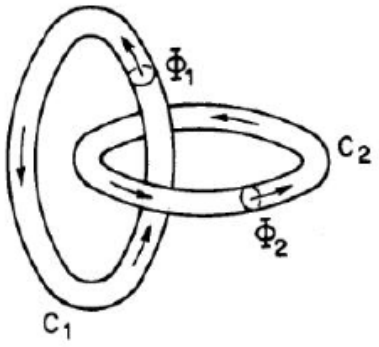

FIGURE 2.1: Moffatt's two interconnected magnetic flux tubes.

He clearly explained how topology and helicity are interconnected, by showing that helicity depends only on the fact that the two fluxes, ϕ_1 and ϕ_2, are interlinked. Moreover he proves that the value of helicity does not change if the two tubes C_1 and C_2 are deformed maintaining their linkage, but as soon as one of the tubes is cut and removed helicity goes to zero. Moffatt's observations were formalized by a previous Woltjer's work [14] by means of two theorems. In the first one Woltjer proves that magnetic topology is always preserved in an ideal (with a null resistivity) magnetofluid hence, as long as $\eta = 0$, helicity is a constant of the system; while the second theorem deals with magnetic relaxation.
Magnetic relaxation is a process that leads the system to relax toward a minimum energy state by means of the self-generation of fields and currents. While the magnetic field is relaxing by means of reconnection, its energy decreases till no more is available. The *magnetic field energy* is defined as:

$$W = \frac{1}{2\mu_0} \int_V \mathbf{B}^2 d\tau \tag{2.2}$$

Eventually, the lowest energy state compatible with the given helicity and boundary conditions is reached. According to Woltjer, this state is a linear force-free magnetic

field while the dynamics described above is termed *Taylor relaxation* [15, 16].Taylor's relaxation is the most relevant model in literature for plasma relaxation. Taylor recognized that in the ideal MHD limit the helicity of each field line is an invariant of motion, whereas for a plasma of small but finite resistivity only the total magnetic helicity of the system is invariant during its evolution towards a minimum energy state. From Woltjer's theorem it follows that the plasma final state is a linear force-free magnetic field configuration.
In real plasmas small departures from the perfect-conductivity approximation should be taken into account, especially if events as magnetic reconnection occurs. If $\eta \neq 0$ then the topological properties of the magnetic field are no longer preserved and the magnetic field lines may break and coalesce, moreover as $\eta \rightarrow 0$ the regions over which resistivity acts get smaller, but at the same time the field gradients get larger. In Chapter 4 we will extensively discuss this kind of mechanisms and we will try to give a description of the evolution of magnetic topology when discrete relaxation events occur.

2.2 The wire model

Numerical simulations have proved the existence of an alternative model to Taylor's relaxation. This model foresees the existence of plasma states that are not Taylor's states though similar. Indeed, in these states the magnetic helicity of the whole plasma is better conserved than magnetic energy, as it occurs in Taylor's states. The states of this alternative model may be viewed as the non-linear states of a resistive kink mode stabilized by the toroidal field reversal [17]. We now turn to describe its toy model.

Consider a current-carrying (I_{wire}) resistive wire placed in the axis of a hollow cylindrical flux conserver [17]. A finite, but small axial magnetic field is present inside the cylinder. This means that a poloidal current exists on the cylindrical shell ($I_{\theta,shell}$): the wire is in unstable equilibrium and a small perturbation can trigger the kink and create a poloidal component of the wire current that attracts it toward the shell and increases its distortion (if $I_{\theta,wire}$ has the same direction of $I_{\theta,shell}$). Such a pitch brings a solenoidal effect which increases the magnetic field and the flux inside the kinked wire. The flux conserver imposes a decrease of the magnetic field and the flux outside. As different portions of the helical wire carry currents in opposite directions the instability cannot quench and the continuous growth of the magnetic field and flux

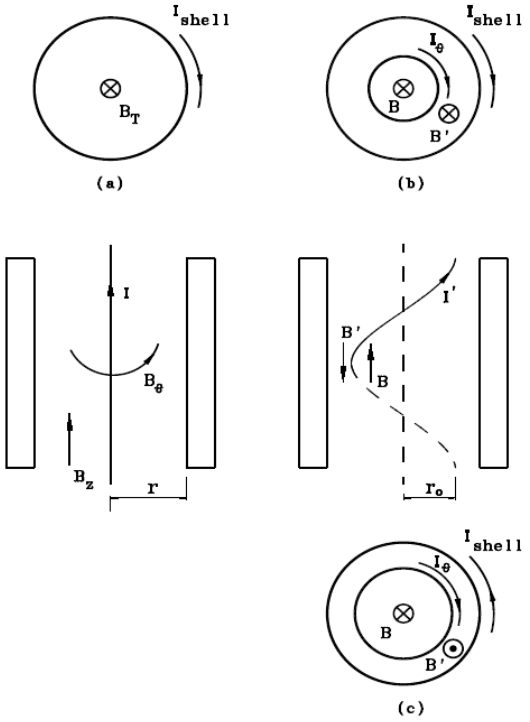

FIGURE 2.2: The wire model.

inside the kinked wire forces the outer magnetic field and the current in the cylinder to reverse. Eventually the wire finds an equilibrium where it is trapped in a sheared magnetic field.

If the wire of the toy model is replaced with a plasma column, this model can be applied to describe both tokamak and RFP equilibria. In the former, weak $m = 1$, $n = 1$ kink mode can be stabilized without field reversal because the corresponding helical deformation extends to the $q > 1$ domain where such a deformation is not energetically favorable. Whereas in a RFP $q < 1$ everywhere, thus such stabilization is not possible and field reversal has to occur.

This model represents a self-organized magnetic system with field reversal where the loss of cylindrical symmetry is essential. In analogy, in Chapter 4 the *dynamo* mechanism will be discussed since it underlies the configuration of the reversed-field pinch and is responsible of its self-sustainement.

Let us now turn to introduce the different topological scenarios associated to the two main dynamics that can be found both experimentally and theoretically in a RFP device.

2.3 Single and Multiple Helicity states

Two different main topologies are experimentally observed in RFP devices: the Single Helicity (SH) and the Multiple Helicity (MH) states.

The first is obtained when a single resistive kink/tearing perturbation[1] saturates and a helical, stable RFP configuration is obtained. These states were firstly found through 2D and 3D numerical simulations in which no helicity was imposed [18] and their signature can be seen by analyzing the Fourier spectrum of the magnetic field and looking for states in which only the $(m = 1,\ n = h)$ mode and its harmonics $(n = hm)$ are present.

As resistive dissipation η decreases other modes can become unstable and the system enters in a non-stationary MH regime characterized by a broad spectrum of Fourier modes with $m = 1$ and different n values. If non-linearity is taken into account, a wide spectrum of $m = 0, 2, 3$ modes is also produced. The consequence is the production of a series of magnetic islands corresponding to resistive kink/tearing modes resonating at rational values of the q profile. The interaction between these magnetic structures generates a chaotic dynamic with detrimental effect on the confinement of energy and particles; anomalous heat and particle transport are then driven by the stochastic magnetic field in the core of the plasma.

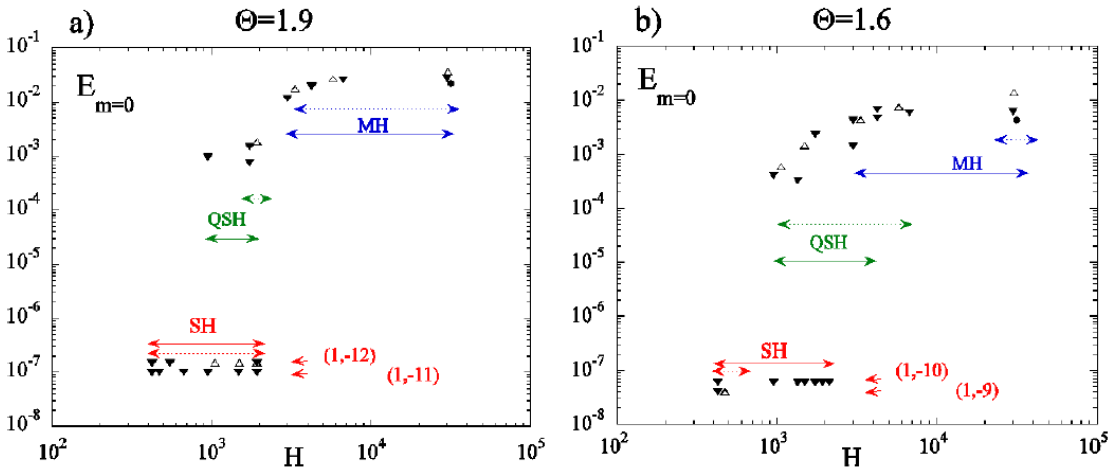

FIGURE 2.3: Time averaged magnetic energy of the spectral component $m = 0$ as a function of the Hartmann number H. Simulations are performed with the SPECYLcode. See [19].

To summarize these different scenarios as predicted by simulations, the energy of $m = 0$ modes turns out to be a useful parameter. $E_{m=0}$ is observed to decay exponentially in

[1] See in Appendix A Section A.1

time when the system reaches a SH state starting from a MH spectrum, as there are no multiple $m = 1$ modes to nonlinearly drive the $m = 0$.

In Figure 2.3 we can see how time-averaged magnetic energy of $m = 0$ modes lets us distinguish between MH and SH states. Visco-resistive pressure-free numerical simulations confirm that the transition from MH to SH states turns out to be continuous as the *Hartmann number* $H = (\eta\nu)^{-1/2}$ decreases[2] and therefore depending on the product of resistivity and viscosity [20]. Nevertheless, this numerical result is in contradiction with experimental investigations which support a Lundquist dependence [21], as we will see.

In between the MH and SH regimes stands the recently discovered *Quasi Single Helicity* (QSH) states and *Single Helical Axis* (SHAx) states. The QSH states are characterized by a different magnetic topology and by the presence of a dominant $m = 1$ mode whose amplitude exceeds by several times that of the other MHD modes, which still have a finite amplitude: in RFX-mod, the dominant mode corresponds to the innermost resonant $m = 1$, $n = 7$ helical state.

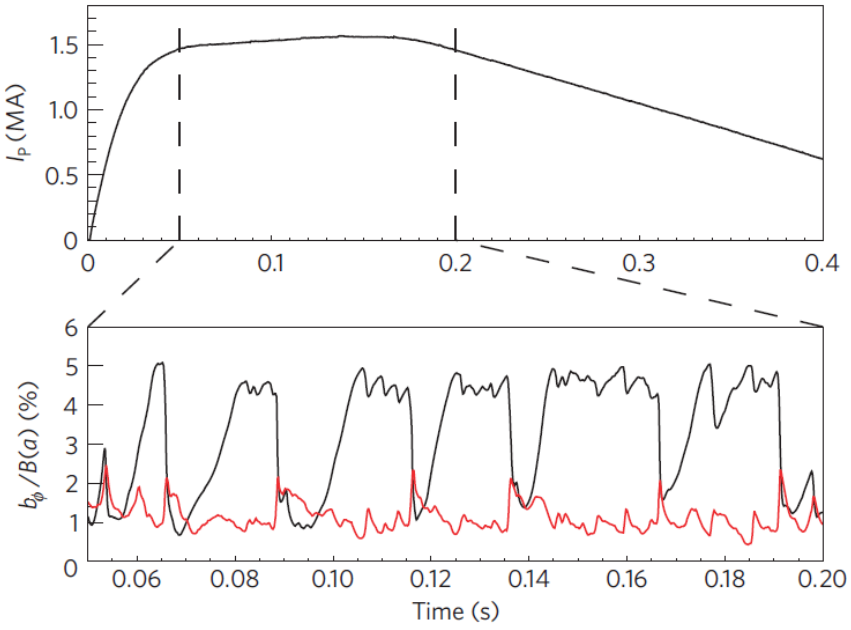

FIGURE 2.4: Top panel: plasma current as a function of time. The dashed lines delimit the flat-top phase of the discharge. Bottom panel: The black curve shows the amplitude of the $m = 1$, $n = 7$ dominant mode during the flat-top phase while the red curve represents the amplitude of the secondary modes (defined as the square root of the sum of their squared amplitudes). The periodical back transitions to the MH state are marked by the strongly decrease of the dominant mode amplitude. The figure is taken from [21].

[2]The transition details are also found to depend on the pinch parameter Θ.

When the plasma current is increased above a certain value ($I_p \geq 1.5MA$), a purer single helical spectrum with further reduction in secondary modes emerges and the amplitude of the dominant exceeds a threshold of $\sim 4\%$ of the total magnetic field at the edge, as it is shown in Figure 2.4.

The QSH properties are found to be related to the Lundquist number S [21], defined as the ratio of the resistive diffusion time to the Alfvén time[3].

Figure 2.5 shows the dependence of the QSH persistence with S, showing that higher S values, which correspond to hotter plasmas obtained at higher current levels, lead to longer persistence, reaching values up to 90%.

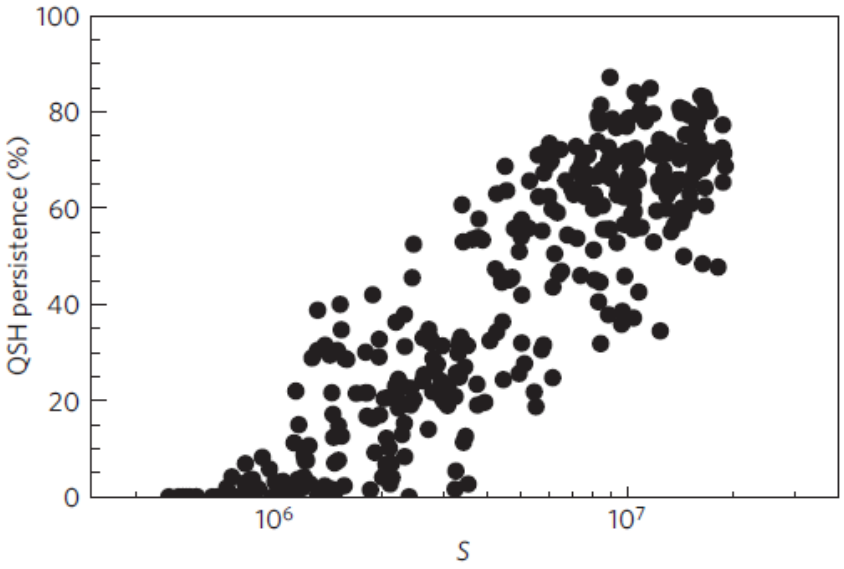

FIGURE 2.5: QSH persistence plotted versus the Lundquist number S for a wide database of discharges with currents ranging between 0.3 MA and 1.6 MA. The persistence is quantified as the ratio between the total duration of the QSH during the current flat-top and the flat-top duration; it is longer at higher S. The figure is taken from [21].

The transition to a new class of QSH states, named single helical axis (SHAx) is accompanied by a deep modification of the magnetic topology with respect to standard QSH states: the O-point corresponding to the magnetic axis and the island's X-point collapse one onto the other, the island's separatrix[4] is expelled from the plasma and the island's O-point survives as the main magnetic axis of a spontaneously occurring helical plasma. Thanks to the measurements of different diagnostics (soft X-ray emission tomography, magnetic measurements, Thomson scattering) it is shown the existence

[3] See Equation A.10 in Appendix A.

[4] Also called the *Last Closed Flux Surface* (LCFS), the separatrix defines the last surface after which all the other magnetic surfaces are open.

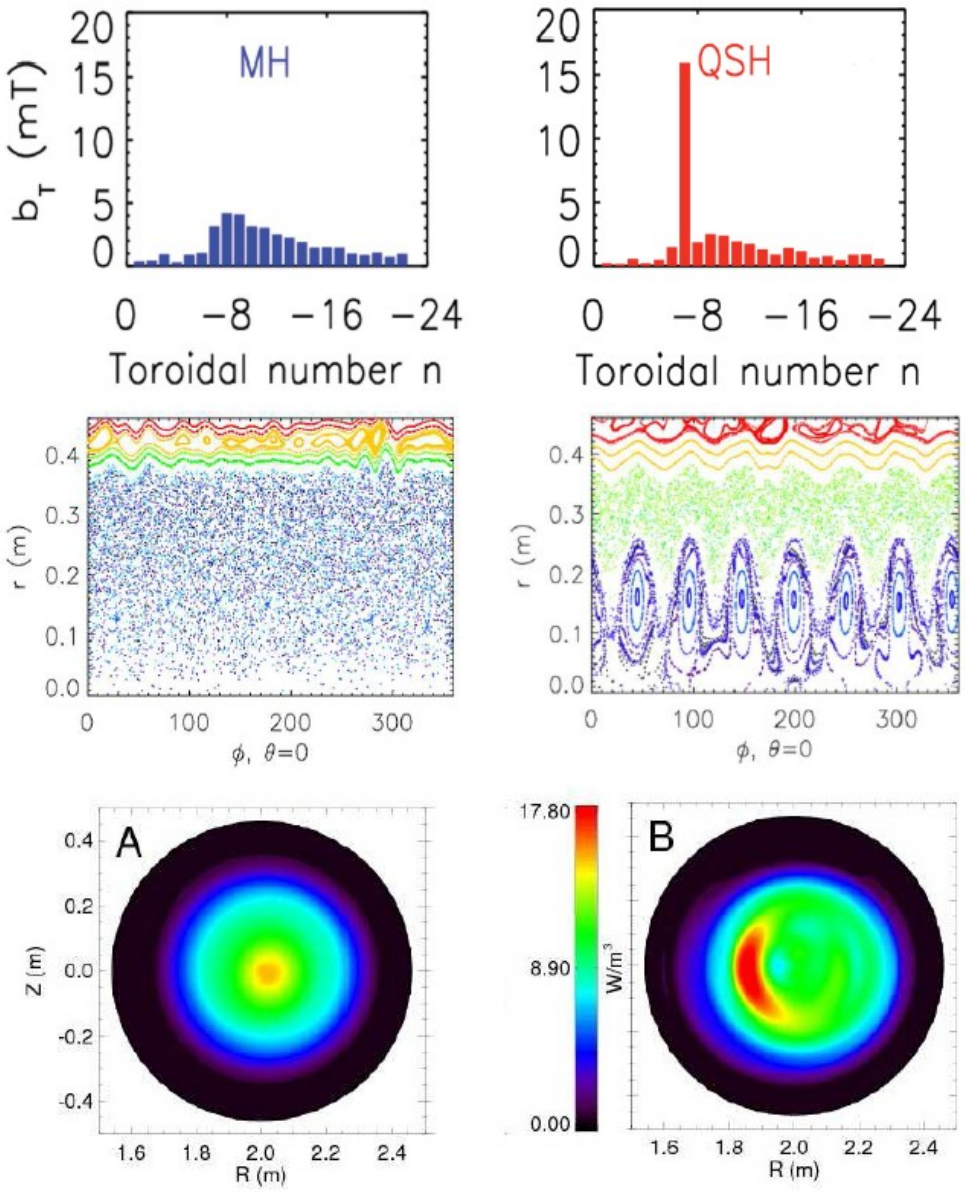

FIGURE 2.6: Left. **MH features**: MHD spectrum where many modes have comparable amplitudes; Poincaré plot with the typical chaotic core; SXR tomography on the poloidal plane, which displays a poloidally symmetric emissivity. MH are the typical state for low plasma current discharges, and only transient states in high plasma discharges. Right. **QSH features**: MHD spectrum where just one mode dominates the spectra; Poincaré plot where the coherent structure in the plasma core, related to the dominant mode, is evident; SXR tomography on the poloidal plane, which displays the bean-like hot structure. QSH are the typical state for high plasma current discharges, and only transient states in low plasma discharges. This figure is intended to give a qualitative picture to summarize MH and QSH features. The figure is taken from [22].

of a hot bean-like structure consistent with the helical shape of the magnetic flux surfaces. In Figure 2.6 we report a visual resumé of the general features of Multiple Helicity and Quasi-Single Helicity states.

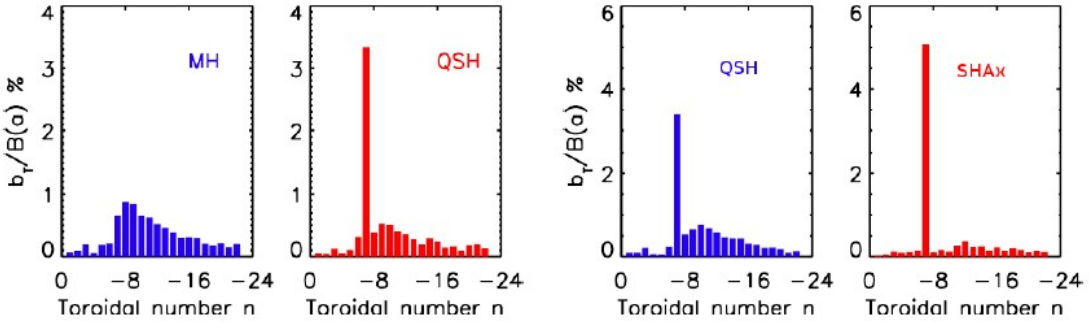

FIGURE 2.7: MHD modes spectrum in MH-QSH (DAx) states and in QSH (DAx)-QSH (SHAx) states. The figure is taken from [23].

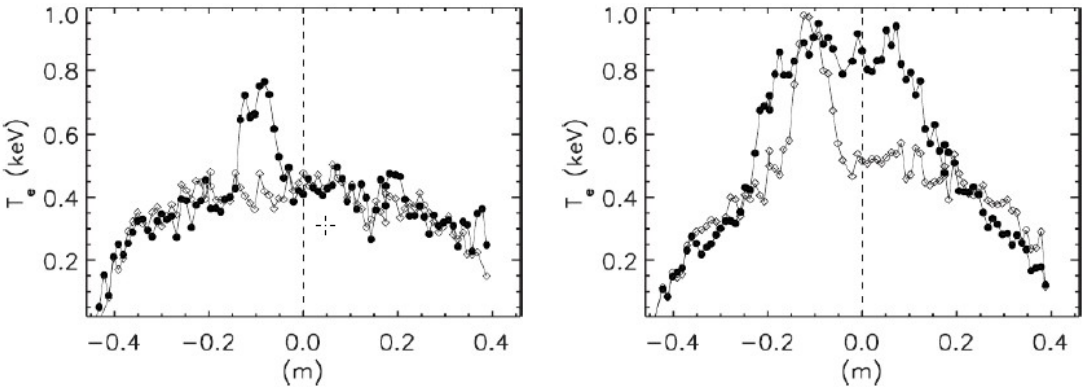

FIGURE 2.8: Electronic temperature in MH states (white circles) and QSH (DAx) (black circles) in the left panel, while in the right panel T_e in QSH (DAx) states (white circles) and QSH (SHAx) (black circles). The figure is taken from [23].

The RFP plasma self-organizes into a helical state [21] through the transition from MH to QSH states and the change in the magnetic field topology. This self-organization has the advantage of improving confinement properties with respect to the MH regime also through the emergence of an electron internal transport barrier (eITB) (see [24] and [25]), visible in Figure 2.8.

As anticipated, a better comprehension of the mutual influence of topology and transport in the edge region represents the main aim of this thesis work. The understanding of the edge transport in RFPs remains crucial in all the regimes previously described: indeed at low plasma current, in MH states, the edge region is the only region where

good magnetic surfaces survive and substantially establish the confinement's degree of the configuration. At a higher current, in QSH or SHAx states, still strong gradients develop in the peripheral region, thus influencing the overall plasma transport: moreover, this region determines the plasma-wall interaction, an important issue in RFP and plasma physics in general, thus motivating the strong effort devoted to analyses and interpretation of kinetic and transport properties at the plasma boundary.

2.4 RFP's edge topology

In the core of RFP plasmas in Multiple Helicity regime several MHD resistive modes resonate generating a stochastic magnetic field: superposition of magnetic islands destroys the well-conserved magnetic surfaces and enhances the chaos.
A large spectrum of $m = 1$ modes is hence destabilized in the core due to the peculiar decreasing q profile, with values always below unit moving from around $q_0 = \frac{2}{3}\frac{a}{R}$ on axis to smaller values at the edge where the toroidal magnetic field reverses. The $m = 1$ modes are responsible for an effective electric field production through the $< \tilde{\mathbf{v}} \times \tilde{\mathbf{b}} >$ dynamo term, which effectively transfers energy from toroidal to poloidal magnetic field circuits sustaining the magnetic field reversal at the edge region against resistive diffusion.[5]
The interest in edge topology resides on the fact that confinement properties are heavily affected by transport phenomena occurring in this region of the plasma, but there is also the unavoidable need to prevent damages to plasma facing materials. Since particle and energy losses in fusion plasmas considerably exceed those expected from collisional transport, turbulent (*anomalous*) transport is considered to be responsible for these losses. The use of probes has allowed extensive measurements of turbulence driven fluxes at the edge: turbulent transport can be conveniently divided into an electrostatic and a magnetic contribution. In particular, measurements coming from many ohmicaly heated devices at the plasma boundary show that particle transport is mainly, though not completely, driven by electrostatic fluctuations (see for example [26, 27, 28]). Energy transport instead is still an open question as electrostatic fluctuations can account for about 30% of the total lost power [29].
In the region between the reversal of the toroidal magnetic field and the first wall, measurements of particle transport have shown similarities with tokamaks, where both

[5] We postpone to Section 4.2.1 a more detailed dissertation on the dynamo mechanism.

edge particle and energy transport are attributed to electrostatic fluctuations. Increasing effort has been devoted to analyze the statistical properties of fluctuations in plasma turbulence, different approach with respect to the characterization of global parameters. Despite the differences in the equilibrium fields, the size of the device or the type of input power, both these magnetic confinement configurations, if compared through 3D fields and magnetic chaos in the edge, show coherent and macroscopic modulations of kinetic quantities which can be easily put into relationship with the symmetry of the dominant magnetic island as shown in [30].

2.4.1 RFX-mod: the edge region

The complex magnetic topology at the edge region of a RFP device is clearly linked to the inversion, in the reversal region, of the toroidal component of the magnetic field B_ϕ. Analyzing the RFX-mod case, it is possible to see that due to the presence of the $q = 0$ surface, all the $m = 0$ modes resonate and together with the beating of the $m = 1$ modes, create a chain of poloidally symmetric islands in the outer plasma. The radial position of these islands can be externally influenced by choosing the value of the reversal parameter F: as can be seen in Figure 2.9 at markedly negative, *deep-F*

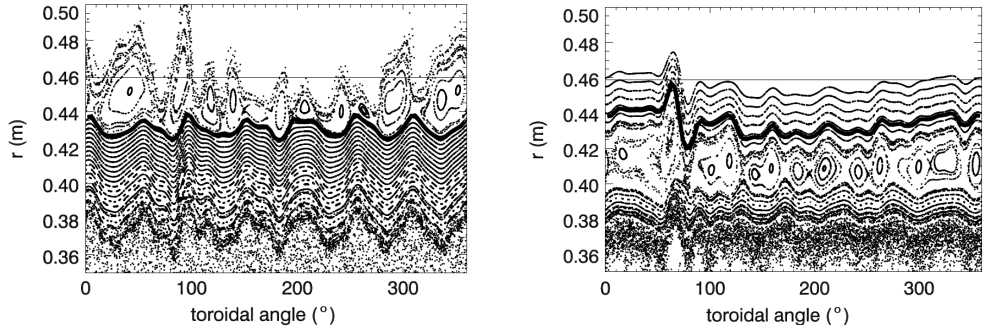

FIGURE 2.9: Poincaré plots of the magnetic field on the outer equator for a SHAx state at 1.5 MA at shallow reversal (left) and deep reversal (right). The thick line marks the position of the LCFS. The horizontal line at $r = 0.459\ m$ indicates the first wall position. Figures are taken from [31].

values ($F < -0.15$) the $m = 0$ islands close entirely into the chamber, while for F values close to 0 or *shallow* ($F > -0.05$), the islands field lines tend to intercept the first wall before closing again.

Generally speaking, two different topologies of the *last closed flux surface* can be identified. In analogy to what already discussed in 1.3.1 for the tokamak case, in the *limiter* configuration the LCFS touches a solid object which defines its position. This direct

contact leads to intense heat loads and a high degree of particle recycling. The second, more sophisticated approach consists of creating a *divertor*, a magnetic structure with one or more X-points, which act as links between a LCFS not touching any solid object and open field lines which are diverted towards appropriate plates, on which heat and particle fluxes impinge. These plates can be located far away from the LCFS, so that neutrals resulting from plasma neutralization and sputtering processes can be ionized before entering the confined plasma, thus resulting in a low recycling of the main gas and in a lower impurity content of the plasma.

Coming back to the topology of RFX-mod, it has been found [31] that in SHAx condition obtained at shallow reversal the last closed flux surface is well separated from the wall by the $m = 0$ islands and their X-points act as to form a *divertor-like* configuration. In contrast, at deep reversal the LCFS is located beyond the $m = 0$ island chain and a *limiter-like* condition is obtained.
Furthermore, the $m = 0$ modes tend to phase lock to each other (see the studies in [32, 33]) with a phase close to that of the $m = 1$ modes phase locking. Thus, the topological characteristics of the external region are quite complicated, with the *large helical deformation* (LHD) due to phase and wall locking of the $m = 1$ modes and the funnel-like shape of the plasma column due to the aforementioned phase-locking of $m = 0$ modes (see Figure 2.10).

The interpretation of data coming from this region of the plasma consequently requires a detailed comparison with the local magnetic topology.
In this work, we have exploited the *Field Line Tracing* code **FLiT** [34] in order to reconstruct the local topology and *Poincaré plots* have been used to depict it. Both these analytical tools will be described in the next subsection.

2.4.2 FLiT and Poincaré plots as a tool

Just outside the first wall of RFX-mod, a system of 48 x 4 sensors measures the fluctuations of the radial and toroidal components of the magnetic field, as described in Section 1.4. These measurements are then used for the reconstruction of the eigenmodes into the plasma based on Newcomb's equation in toroidal geometry, following the model described in [12]. This model applies to toroidal plasmas in a *force-free* assumption and solves a system of equations for the harmonics of the potentials F

and Ψ related to the fields by:

$$B^{\theta} = \frac{1}{\sqrt{g}}\frac{\partial \Psi}{\partial r} \qquad B^{\phi} = \frac{1}{\sqrt{g}}\frac{\partial F}{\partial r} \qquad b^{r} = \frac{1}{\sqrt{g}}\left(-\frac{\partial F}{\partial \phi} - \frac{\partial \Psi}{\partial \theta}\right) \tag{2.3}$$

where g represents the toroidal geometry metric tensor for the system and all coordinates are intended as flux coordinates.
The FLiT code, extensively exploited during this thesis, has been developed [34] starting from this model assumptions, in order to reconstruct the trajectory of the magnetic field lines inside the plasma using flux coordinates. These are obtained integrating the controvariant components of lines equations:

$$dr = \nabla r \cdot \frac{\mathbf{B}}{B}\, dl = \frac{B^{r}}{B}\, dl \qquad d\theta = \nabla \theta \cdot \frac{\mathbf{B}}{B}\, dl = \frac{B^{\theta}}{B}\, dl \qquad d\phi = \nabla \phi \cdot \frac{\mathbf{B}}{B}\, dl = \frac{B^{\phi}}{B}\, dl \tag{2.4}$$

where

$$B = |\mathbf{B}| = \sqrt{g_{rr}B^{r}B^{r} + g_{\theta\theta}B^{\theta}B^{\theta} + g_{\phi\phi}B^{\phi}B^{\phi} + 2g_{r\theta}B^{\theta}B^{r}} \tag{2.5}$$

A straightforward way to visualize the complex magnetic topology using the output of the FLiT code is the *Poincaré plot*, a map where every point is the intersection of a magnetic field line in the (r, ϕ) or the (r, θ) plane with a poloidal or toroidal chosen section. The 3D topology is then reduced to a 2D problem where each magnetic field line is represented through its (r, ϕ) or (r, θ) coordinates at constant θ or ϕ. Through IDL routines it is possible to obtain a set of r, θ and ϕ coordinates from the FLiT code output and then build the actual Poincaré plot: an example is given in Figure 2.10 where the colors are assigned according to the r value of the starting point of the lines. If we take a closer look to the Poincaré plot shown in Figure 2.10, it is possible to distinguish different topological regions:

- an **ergodic layer**: is the blue zone for $r < 0.37\ m$ (r is the camera radius). In this region we have the overlapping of the ($m = 1$, n) magnetic islands recognizable from the irregular field lines trajectories and responsible for the magnetic field stochasticity and the deteriorating of the confinement properties in this core region;

- $\mathbf{m = 0}$ **magnetic islands**: for $0.37\ m < r < 0.42\ m$. It's the edge plasma region, before the first wall, where the toroidal field reverses its sign. The islands are created by *tearing* ($m = 0$, n) modes resonating at the reversal $q = 0$ surface;

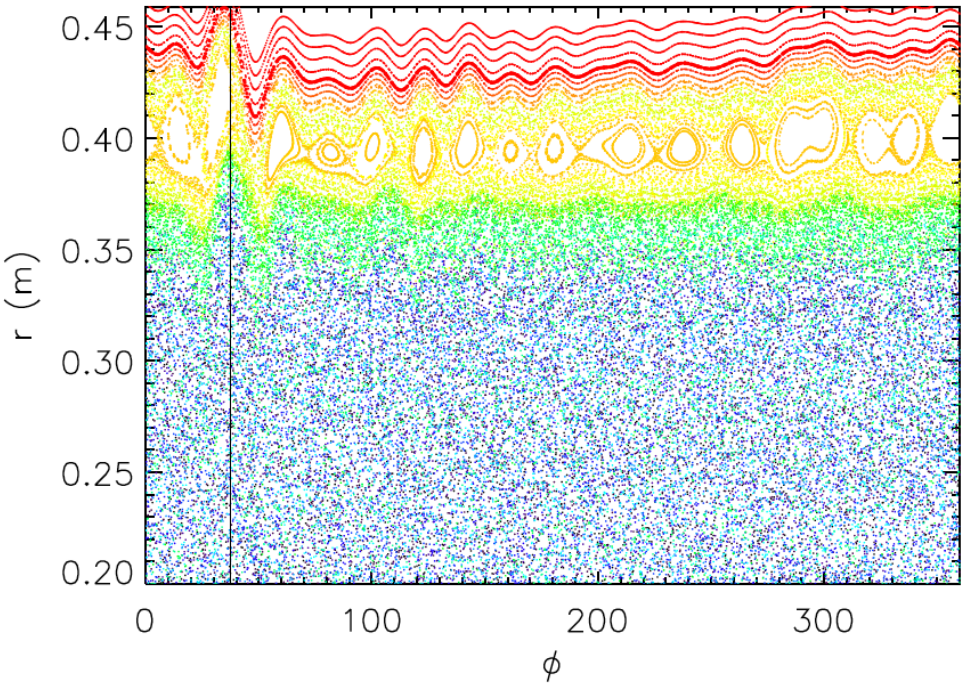

FIGURE 2.10: Poincaré plot built starting from the output of the *FLiT* code for the $(m = 0, 1; n)$ modes of the spectrum. The vertical line stands for the position of the modes locking. Colors are chosen according to the r value of the starting point of the lines.

- **conserved magnetic surfaces**: it is the most external region, around $r = 0.459\ m$, where the flux surfaces are depicted in red. These flux surfaces are influenced by the perturbation of a non-ideal plasma, they are anyway conserved and the lines which do not touch the wall help confine the plasma thanks to the parallel transport. Their behavior gives an idea of the external plasma shape. The last of these surfaces is the **LCFS**.

However, we should highlight that the radial characterization of the aforementioned different topological regions strictly depends on the q profile and the reversal parameter: in other words, the equilibrium deeply affects the topological domain.
Poincaré plots will be used and shown throughout this thesis to help the reader visualize the plasma's magnetic topology that underlies the analyzed transport measurements. All the edge transport measurements (which are a function of time) analyzed in this thesis are related to a topology that is not stationary in time: indeed the islands are slowly rotating in the laboratory frame of reference. In order to correctly map edge measurements, it should be used a frame of reference that rotates together with the magnetic islands, based on the helical field structure set by the dominant ($m = 1$,

$n = -7$) mode. Therefore, after the introduction of FLiT and the Poincaré plot, we will describe the formalism that leads to the definition of the *helical angle*.

2.4.3 Helical angle

Due to the lack of proper diagnostics for measurements of electrostatic turbulence working at high current regime, in RFP experiments on RFX-mod we were led to operate at low plasma current ($I_p \leq 450\ kA$) and to apply magnetic field perturbations of definite helicity, via the saddle coils feedback system, in order to mimic the high current configuration.

We have chosen to induce a ($m = 1$, $n = -7$) mode which is naturally amplified by the plasma and gets a non-axial symmetric topology. The mode rotates toroidally, with a frequency of a few tens of Hz. Furthermore, ($m = 1$, $n = -7$) is the periodicity of the spontaneous dominating mode which is produced in RFX-mod quasi-single helicity regime occurring at high plasma current [35].

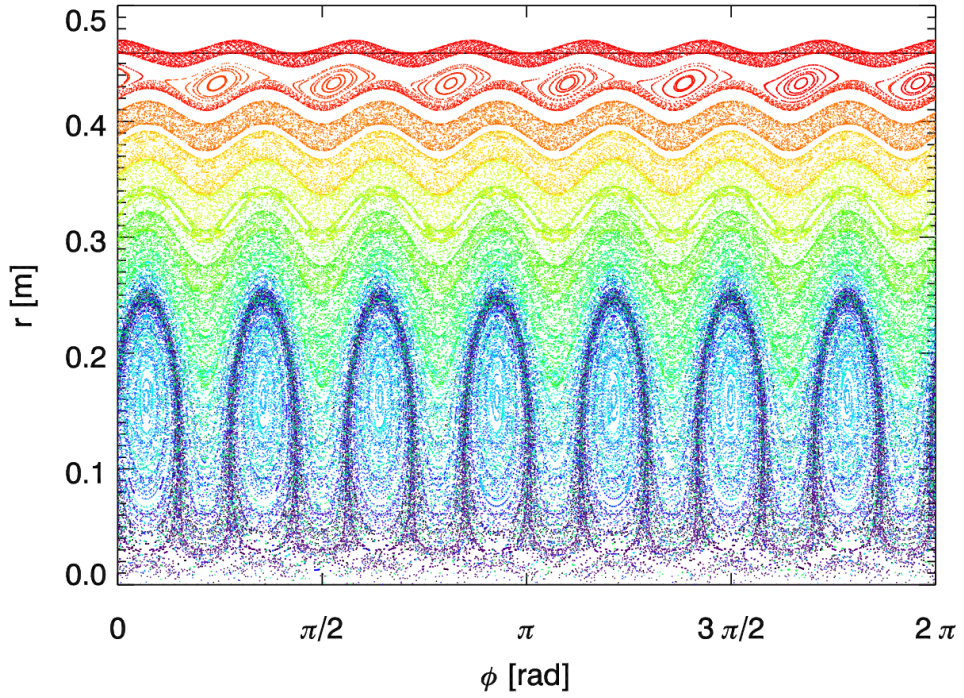

FIGURE 2.11: Poincaré plot for the discharge # 30008 in the plane (r,ϕ) at $\theta = 0°$ showing the ($m = 1$, $n = 7$) symmetry and the chain of ($m = 0$, $n = 7$) magnetic islands resonating at the reversal surface.

The presence of the externally applied magnetic perturbation in these discharges modifies the edge plasma magnetic topology, giving rise, due to the toroidal coupling, to $(m = 0,\ n = 7)$ magnetic islands resonating at the reversal surface. The perturbed magnetic field pattern, if seen in a radial-toroidal section, presents a typical chain of O-points and X-points as can be seen in Figure 2.11.
Theory and experiment are in agreement that electrostatic properties of the plasma edge are modulated by the presence of magnetic islands: electrons are bonded to the magnetic field lines and they spend more time near the X-point, while ions have a larger Larmor radius and are affected by more significant diffusion across the magnetic surfaces [36]. This tendency to a charge separation is balanced by an ambipolar electric field, modifying the flow due to the $E \times B$ drift.
It represents a key issue to associate to edge measurements the correct phase with respect to the $(m = 1,\ n = -7)$ mode.

The interpretation of measurements when 3D fields are present in a plasma is a complex problem. Usually, magnetic equilibrium for toroidal configurations may be computed through an assumption of a 2D geometry, with an ignorable coordinate[6].
The magnetic problem can therefore be studied in perfect analogy with a classical Hamiltonian system with one degree of freedom: the ignorable angle plays the role of time and the Hamiltonian is given by the flux function associated to the remaining angle using toroidal coordinates $(r,\ \theta,\ \phi)$[7].
Starting from the analogy with the Hamiltonian description, the assumption of a 2D system where a coordinate is ignorable leads to the definition of the covariant form of the magnetic field:

$$B = \nabla\psi \times \nabla\theta - \nabla\psi_p \times \nabla\phi \tag{2.6}$$

In this expression, using action-angle coordinates, we are led to the definition of flux-surface coordinates: ϕ and θ are the straight toroidal and poloidal angles while ψ and ψ_p are the corresponding fluxes across the conserved magnetic flux surfaces. From Equation 2.6 it is possible to extract the equation of the field line as the Hamilton-Jacobi equation of motion, by using the links between mangetic quantities (fluxes, coordinates) and canonical coordinates $(H,\ p,\ q,\ t)$.

[6] In a first-order approximation, the ignorable coordinate is ϕ for a tokamak and θ for a RFP configuration. The poloidal angle is chosen because at the edge of a RFP device the toroidal component of magnetic field reverses its sign. At the reversal the ignorable coordinate would not be linearly defined.

[7] The Hamiltonian will be the poloidal flux ψ_p in case of a tokamak configuration and the toroidal flux ψ in case of the RFP one.

If time is the ignorable coordinate, the Hamiltonian is the conserved poloidal flux [37], $H = \psi_p$, and the whole analogy can be written as:

$$\begin{cases} \rho &= \psi_p, \\ t &= \phi, \\ p &= \psi, \\ q &= \theta. \end{cases} \tag{2.7}$$

where $H(p,q) = cost \equiv \rho$ is used to label conserved magnetic flux surfaces. 2D assumptions are at the basis of the field's description in action angle coordinates (Equation 2.6). If we now consider the environment in which transport measurements can be performed, it seems that their interpretation in a 2D framework would fail when the involved magnetic fields are fully 3D: this is a characteristic of Multiple Helicity dynamics where an ignorable coordinate cannot be evidenced. This statement does not subsist in conditions of Quasi Single Helicity, where the symmetry related to the dominant mode that defines the helical state can be highlighted by using a transformation of coordinates and an ignorable coordinate can be found.

In the following, a frame of reference moving with the dominant mode will be introduced in order to correctly relate different toroidal and poloidal measurements with respect to the helix. There is already a clear evidence [35] that edge properties are modulated along the toroidal angle ϕ and also in time since the helical plasma is slowly rotating in the laboratory frame of reference. These oscillations are furthermore correlated with the local plasma displacement Δ_r associated to the dominant mode: a precise description of the edge geometry needs proper coordinates.

As we have anticipated at the beginning of the paragraph, due to the lack of diagnostics for measurements of electrostatic turbulence working at high current when QSH regimes arise, we are forced to operate at low plasma current where the underlying natural dynamics is of the MH kind. Therefore we applied external magnetic perturbations of definite helicity, with (m, n) reproducing the periodicity of the spontaneous dominant mode in QSH. This technique mimics the high current QSH state and identifies a dominant symmetry with the consequent possibility to apply the Hamiltonian description.
The standard expression [38] of the poloidal flux for a single ($\bar{m}$, $\bar{n}$) mode is adopted:

$$\psi_P(\rho,\theta,\phi) = \psi_P^0(\rho) + \psi_P^{\bar{m},\bar{n}}(\rho) e^{i(\bar{m}\theta - \bar{n}\phi)} + c.c. \tag{2.8}$$

where $\psi_P^0(\rho)$ is the equilibrium component and $\psi_P^{\bar{m},\bar{n}}$ the perturbative term linked to the dominant mode. We define $U = \bar{m}\theta - \bar{n}\phi$ and, as a consequence, the Hamiltonian in QSH/SH condition is indipendent from one ignorable coordinate that represents the canonical time in the the canonical transformation from (r, θ, ϕ) to (ρ, U, ϕ).
To connect with physical quantities, we define the helical flux:

$$\begin{aligned} \chi &= m\psi_p - n\psi, \\ &= \chi_0(\rho) + \alpha_{\bar{m},\bar{n}} sin\left(\bar{m}\theta - \bar{n}\phi + \varphi_{\bar{m},\bar{n}}(t)\right) \end{aligned} \tag{2.9}$$

where $\alpha_{\bar{m},\bar{n}}$ is the perturbative amplitude and $\varphi_{\bar{m},\bar{n}}(t)$ is the associated phase [39]. Finally, we choose the following definition for the *helical angle*:

$$u(\theta, \phi; t) = \bar{m}\theta - \bar{n}\phi + \varphi_{\bar{m},\bar{n}}(t) \tag{2.10}$$

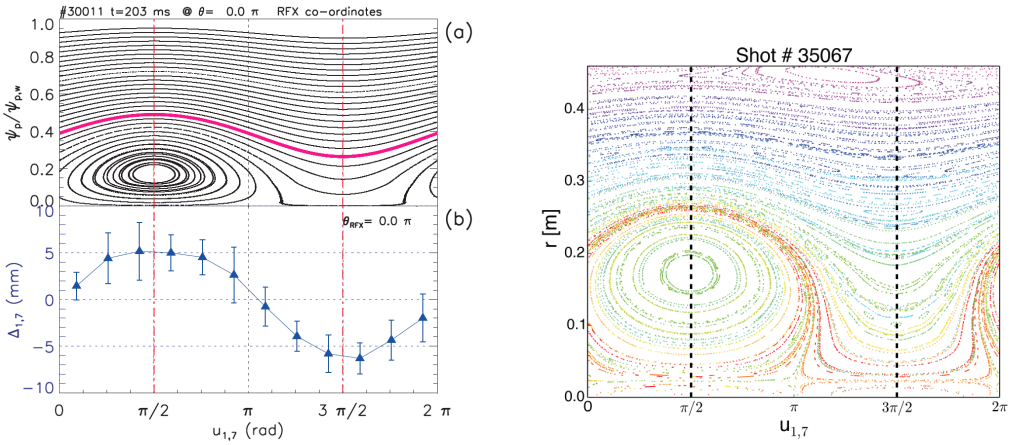

FIGURE 2.12: *(a)* Magnetic flux for the $(1, -7)$ magnetic deformation as a function of the helical angle $u_{1,-7}$;*(b)* radial displacement at $r/a = 1$, again as a function of the helical angle $u_{1,-7}$. The definition of the angle is such that the OP appears at $u = \pi/2$ and the XP at $u = 3/2\pi$. The right panel shows a Poincaré plot obtained by the output of the FLiT code for the discharge #35067 in the plane $(r, u_{1,-7})$.

As it is customary for the definition of the helical coordinates in RFX-mod [40, 41] the amplitude and phase of the dominant ($m = 1$, $n = -7$) perturbation are obtained by solving Newcomb's equations in toroidal geometry with the code NCT [12], starting from the experimental pick-up coil data, δB_ϕ and δB_r , measured at the wall. For each time t , definition in Equation 2.10 provides a unique way of assigning a measurement at (θ, ϕ) to a definite phase relation with the topology of the (m, n) mode. In particular, the O-point (OP) is always found at $u = \pi/2$, while the X-point (XP) is

found at $u = 3/2\pi$, as shown in the panel *(a)* of Figure 2.12.
Equation 2.10 can be applied to a generic mode, e.g. also the $(m, n) = (0, 1)$ mode that dominates in MH discharges and resonates at $q = 0$.
In QSH/SH experiments, the angle $u_{1,-7}$ replaces a more empirical parameter, namely, the shift of the last closed flux surface $\Delta_{1,-7}$, which has been used in the past as a proxy to characterize the PWI and flows in the edge [35]: as shown in the panel *(b)* of Figure 2.12, the maximum shift $\Delta_{1,-7}$ corresponds exactly to the OP.

2.5 Tokamak's edge topology

Let us now focus on the main features of tokamak's edge topology and eventually introduce the Resonant Magnetic Perturbations (RMPs), whose effects on the edge are studied in this thesis as the link between RFP and tokamak magnetic configurations.

It was discovered in the german tokamak ASDEX [42], at the beginning of the 80's, that under certain conditions (typically above a certain threshold in the injected power P_{inj}), a transition occurs in the plasma, resulting in a clear improvement of the confinement. This mode was given the name of *H-mode*, the H standing for *high* confinement, as opposed to the *L-mode*, with the L for *low* confinement, which was the reference mode until then. In H-mode, the energy confinement time increases by typically a factor of 2 with respect to the L-mode. The H-mode is characterized by a transport barrier, i.e. a region where the radial transport is reduced, located at the edge of the plasma. Experiments show that this is due to a reduction of the turbulence. Because of the reduced transport, the radial gradients of the plasma density and (ion and electron) temperatures in the *Edge Transport Barrier* (ETB) region are enhanced.

2.5.1 Edge Localized Modes

Figure 2.13 illustrates a tokamak discharge during the L to H transition and after it. In this case we can observe a series of bursts on the D_α signal, after the transition, whose frequency decreases in time. This signal gives a measure of the emission of α ray of deuterium which is associated to its *recycling*, i.e. all the processes the fuel undergoes after reaching the plasma facing components. The D_α signal is therefore a measure of the recycling, which is itself strongly correlated to the particle flux coming

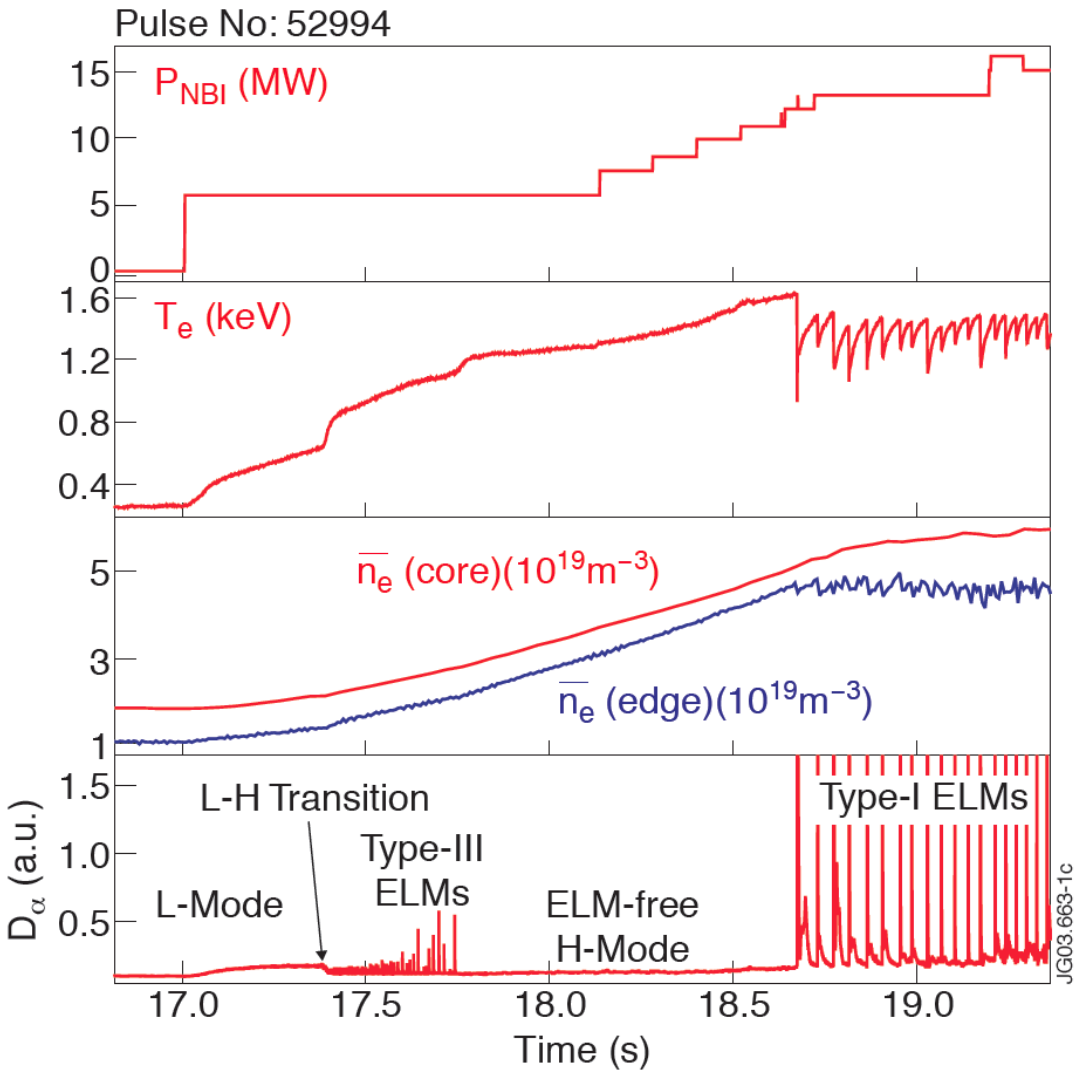

FIGURE 2.13: Overview on a JET discharge displaying the typical sequence of events during the gradual increase of injected power. The figure is taken from [4].

out from the plasma and reaching the PFCs.

These visible bursts in the D_α signal are associated to so-called *type-III Edge Localized Modes* (**ELMs**). If P_{inj} is large enough, type-III ELMs are followed by a period of time where the D_α signal is quiet, which is called the *ELM-free H-mode*. A further increase in P_{inj} leads to large, quasi-periodic bursts on the D_α signal, which are the mark of *type-I* (or giant) *ELMs*.

Good reviews on ELMs can be found in [43, 44, 45, 46].

Type-I ELMs are found to be triggered by MHD instabilities: the model that better describes their evolution is the *Peeling-Ballooning* (P-B) model [47], which deals with instabilities that are driven by both the parallel current density (peeling component, mainly the bootstrap current [3]) and the pressure gradient (ballooning component)

in the pedestal.

The type-I ELMy H-mode has been observed to have also good confinement properties since the induced crash lasts no longer than $200\ \mu s$ and in this lapse of time it helps to expel a certain amount of particles and energy from the edge plasma, resulting in a collapse of temperature and density profiles. Following this collapse, the profiles are re-built because of recovering of confinement (first of all) and heat and particle sources coming from the core of the plasma as well as particle recycling and/or injection. By transiently expelling large amounts of particles from the confined plasma, type-I ELMs maintain a certain level of density and impurity transport at the edge. Without ELMs, it would be difficult to prevent the density from rising too much (with consequent result of disruptions) and the impurities[8] (and also fusion *ashes*, i.e. α particles) to accumulate in the core plasma.

Although this type of ELMs keeps good confinement properties and a good level of fusion power, from the point of view of the PFCs, these phenomena are absolutely deleterious and are synonyms of large transient heat and particle loads that can above all cause deterioration and damage of plasma facing components and for these reasons they need to be avoided.

Active control methods have been investigated to mitigate and/or avoid the generation of ELMs, in particular the one we are interested in for this thesis is the ELMs mitigation by *Resonant Magnetic Perturbations* (RMPs).

2.6 RMPs: Tokamak and RFP

We have seen that ELMs are strictly related to the occurrence of a spontaneous H-mode transition, in presence of additional heating. The transition results in an edge transport barrier (ETB) "too efficient", with growing temperature and density gradients, and associated to an increase in the global stored energy and confinement primarily due to an increase in the edge pressure. The edge pressure and its gradient grow until an MHD limit is reached triggering Peeling-Ballooning instabilities. At this point ELMs occur causing a rapid relaxation of the edge pressure and re-establishing the H-mode transport barrier. On the deleterious side, the ELM burst transports a

[8] Impurities are species others than the species normally present in the plasma (i.e. deuterium, tritium and α particles), for instance carbon, nickel or oxygen. In general, they come from the PFCs, and are nefarious to the plasma because they disperse a large amount of power by radiation (especially the heavy impurities), thereby cooling down the plasma (and in some cases leading to a radiative collapse of the plasma), and also they dilute the fuel, i.e. the deuterium and tritium mixture, reducing the fusion power. The same problems exist with α particles.

heat flux transient to all plasma facing components.

ELMs mitigation and control can be performed through a plethora of different techniques: one possible way, the relevant one to discuss to the aim of this thesis, is the application by external means of 3D magnetic fields.
The RMP approach has demonstrated to be a successful ELMs suppression technique in several existing devices (for example in DIII-D, see the work of *Fenstermacher and Evans* [48]). The main aim is to enhance the radial transport by producing magnetic perturbations with a non negligible radial component so that the very efficient parallel transport contributes to the radial transport.
We know that several islands chains can happen to exist in the plasma, centered on distinct resonant surfaces. However, magnetic islands could be beneficial. When applying small enough RMPs, the islands are still well separated, but increasing the RMPs, the islands grow until they *overlap*. Then, magnetic field lines start to behave in a chaotic manner, all closed flux surfaces between the two resonant surfaces being destroyed, giving rise to a so-called *stochastic* or *ergodic* layer that helps to control and avoid ELMs. The edge ergodization obtained for example in TEXTOR [49], and more generally the island divertor concept also applicable in RFX-mod [31], share the same rationale: a non-axisymmetric magnetic field at the edge exploited to reach improved confinement regime.

Resonant and non-resonant magnetic perturbations used in tokamak plasmas for ELMs suppression can heavily influence transport and kinetic properties. The link between magnetic topology and the transport properties is of fundamental importance both in tokamak and RFP devices due to the modifications shown by the the structure of plasma edge depending on the application of RMP fields. We will see that RMP fields can strongly affect and influence particle and energy transport in the plasma edge of RFX-mod. In particular, throughout the thesis we will focus on the role of electrostatic fluctuations in the edge transport mechanism. We will describe how this specific transport channel can be affected by the application of external 3D fields and we focus on electrostatic fluctuations since these are not always taken into account in presence of stochastic effects on the edge. Furthermore, we will give the reader an enriched characterization of transport properties at the edge of RFX-mod in presence of different underlying topologies.

After having introduced and discussed RMPs as ELMs control tool, in the next subsection we will show some results obtained in the TEXTOR tokamak. Later on and in the next chapter, we will clarify the connection with experiments on RFP devices and diffusively discuss the 3D effects on the RFX-mod boundary.

2.6.1 TEXTOR and the ergodic divertor

In the past, several machines have tested the concept of *ergodic limiter* (see the review paper [50]), *in primis* the TEXTOR tokamak with its dynamic ergodic divertor (DED). The idea is to use a specific set of coils to produce radial RMPs at the edge of the plasma, so as to create an ergodic region, for the purpose of improving the plasma-wall interaction with respect to a standard limiter case.
The main theoretically expected effect of the magnetic field ergodization on radial transport is an enhancement of the heat transport through the electrons [51], which travel along field lines much faster than the ions[9] and hence have larger parallel transport coefficients. This effect was experimentally verified in several devices, as reviewed in [50]. An increase in the density transport is also expected and was clearly observed experimentally [50], sometimes resulting in a *pump-out*, i.e. a drop in the plasma density [52].
The conclusion of the above considerations is that it seems a priori worthwhile trying to ergodize the magnetic field at the edge of an H-mode tokamak plasma in order to increase the pedestal transport and suppress type-I ELMs [53].

Magnetic topology in TEXTOR-DED

Figure 2.14 shows an example of the magnetic topology as a combination of Poincaré plot and a laminar plot modeled for a typical TEXTOR discharge in the $m/n = 6/2$ base mode[10] [54]. The Poincaré plot shows the intersections of the magnetic field lines with the selected poloidal plane and exhibits the stochastic behavior of the field lines. The laminar plot, instead, quantifies the connection length L_c of the field lines as field

[9] At equal temperatures, their thermal velocity is larger than that of the ions by a factor $(m_i/m_e)^{1/2}$.

[10] TEXTOR-DED consists of a set of 16+2 coils implemented into the vacuum vessel and winding helically around the torus at the high field side. They create a spectrum with main resonances around the $q = 3$ surface and poloidal/toroidal base mode numbers of $m/n = 3/1, 6/2, 12/4$ can be selected by different wiring of the perturbation coils. The induced fields can be rotated with frequencies of $\nu = 1 - 10$ kHz.

line length from target to target in units of meters (m) or poloidal turns (p.t.). L_c is depicted as a color coded contour plot.

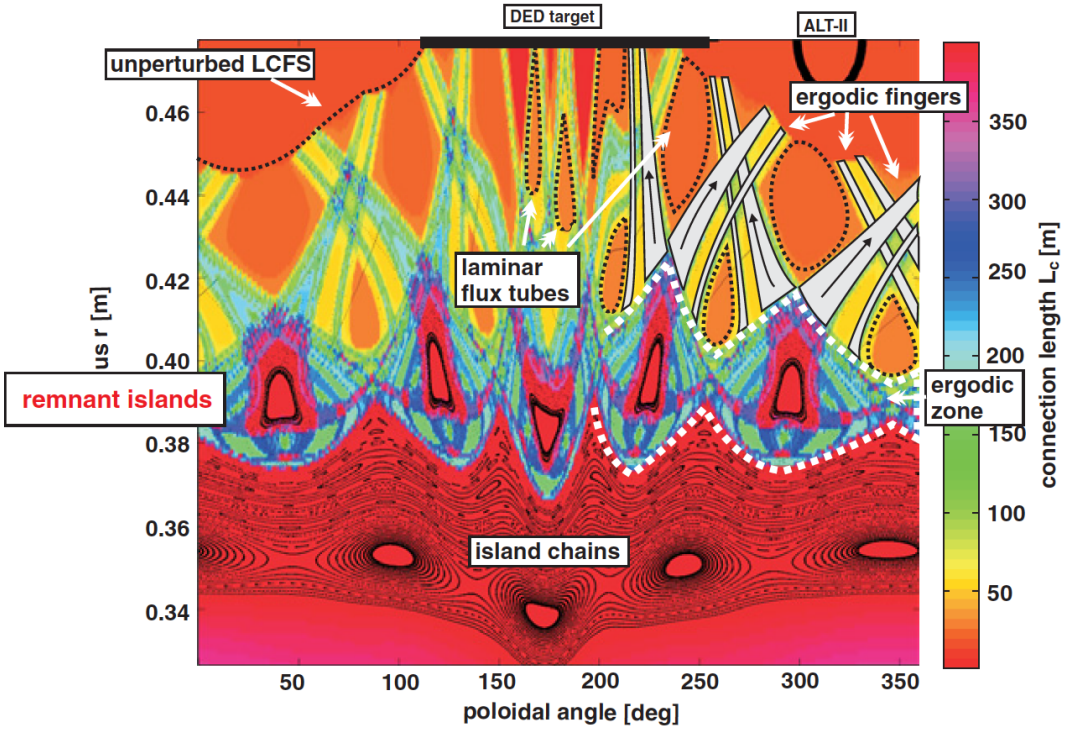

FIGURE 2.14: An overview of the magnetic topology in the stochastic edge for $m/n = 6/2$ base mode configuration. Shown here is a superposition of a Poincaré plot (black colored intersection points with the chosen poloidal plane), a laminar plot (color coded connection length distribution) and highlighted are the characteristic topological domains. The figure is taken from [54].

In Figure 2.14 it is indeed shown that at the edge a complex magnetic topology exists and consists in three regions with very different transport characteristics expected. At small radii, magnetic islands are created with fast particle and heat transport parallel along the field lines around the island's O-point. The island's size grows on flux surfaces closer to the perturbation source and is defined by field lines with mode numbers resonant to the high amplitude Fourier components of the RMP field. Then the island chains of the neighboring resonant flux surfaces overlap and the field lines get stochastic, leading to an increased, diffusive radial transport [51, 55]. They are not bound to the flux surface or single islands chain anymore but become highly diffusive filling the whole volume in the radial and poloidal directions also. This region is indeed the *ergodic region*. However, as the RMP coils are located at the high field side[11], the field lines of the outer edge will be diverted towards the DED target. These near-field

[11]The *HFS* is the radial region where magnetic field profiles are higher with respect to the *Low Field Side* (LFS). As a reference see left panel in Figure 1.6.

effects induce an extended region filled with short L_c field lines: the *laminar zone* [56, 57]. The field lines here are bundled into laminar flux tubes with short connection lengths to the wall, which lead to a strong local reduction in transport relevant quantities as electron density n_e, temperature T_e and therefore pressure p_e with respect to the no-RMP case due to fast parallel particle transport to the wall (see [58]).

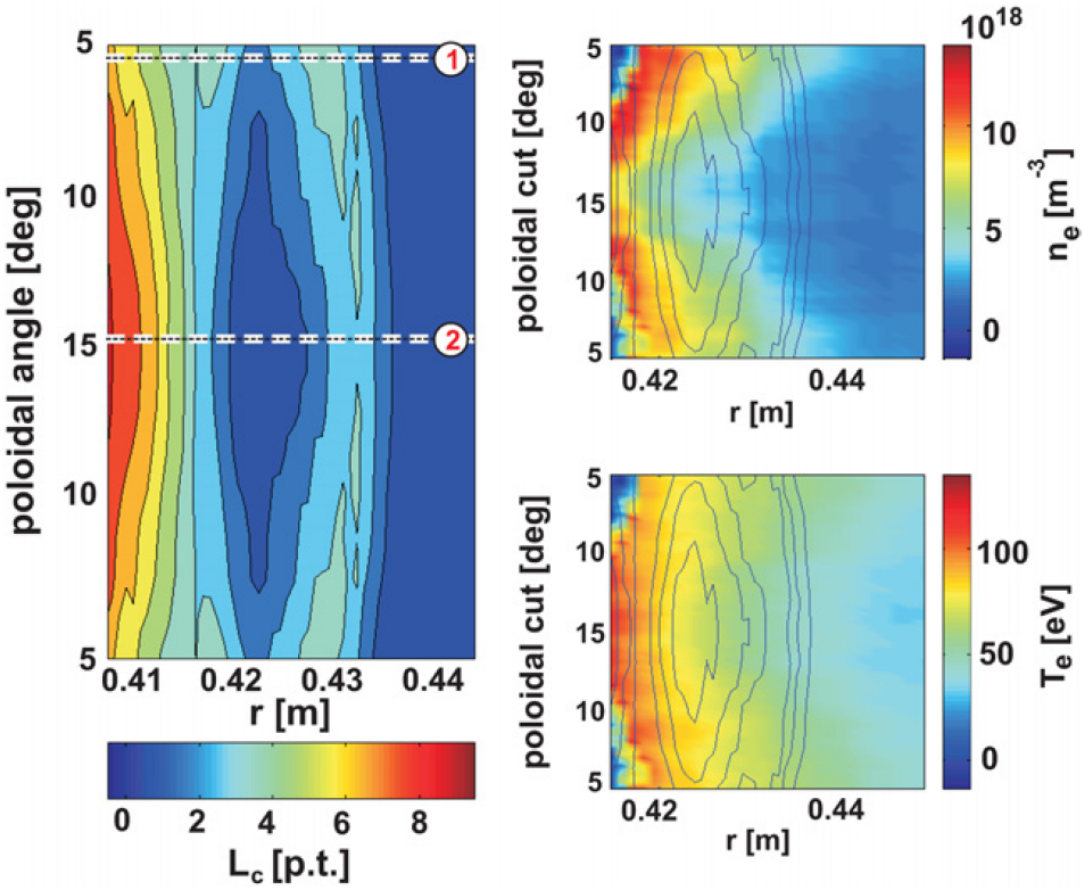

FIGURE 2.15: Two dimensional $n_e(r, \Theta)$ and $T_e(r, \Theta)$ distribution measured with a He beam diagnostic at TEXTOR in $m/n = 12/4$ base mode. The plot on the left shows the corresponding $L_c(r, \Theta)$ distribution. Dashed lines mark the extremal point of sweep: 1 - ergodic domain with long L_c; 2 - laminar flux tube with short L_c. The figure is taken from [54].

For static RMP fields, the laminar zone was shown to impose a modulation to the $n_e(r, \Theta)$ and $T_e(r, \Theta)$ fields along the poloidal angle Θ, as shown in Figure 2.15 and discussed in [54, 59].

In the next chapter we will draw an analogy with the RFP case. We will present analogous information obtained in the RFX-mod RFP device, highlighting the commonality of plasma transport in stochastic/ergodic layer independently from the magnetic configuration and underlying transport mechanism.

Part II

Transport analysis

Chapter 3

Edge and transport

Magnetic perturbations play a fundamental role in the dynamics of RFP and tokamak configurations. In order to represent them, a proper decomposition can be obtained through a Fourier analysis approach; thus, naming m and n as the poloidal and toroidal mode numbers, we can define the magnetic fluctuations in the form:

$$\tilde{b}_r(t) = \sum_{m,n} b_{m,n}(r) e^{i(n\phi + m\theta - \delta b_r^{m,n}(t))} \tag{3.1}$$

The $(m,\ n)$ couple determines a field component that can resonate on a magnetic rational surface that is associated to a rational value of the safety factor $q = m/n$ (see q profile in Figure 1.7). The resonance can subsequently cause the growth of magnetic islands whose width is proportional to the square root of the magnetic perturbations. The condition for islands overlap is characterized by an *overlap parameter* which is found to be proportional to the *magnetic shear*[1]. If magnetic islands overlap, the magnetic field lines can thread from one island to the next and particles can therefore traverse the confinement zone.

The high values of magnetic fluctuations always present in the core of RFP devices naturally favor a complex transport mechanism between the core and the plasma edge and when the condition for islands overlap is satisfied, it consequently represents one of the main energy loss mechanism. However, if in RFP's core particle and energy fluxes are driven by a stochastic magnetic field, measurements coming from many ohmically heated devices at the plasma boundary show that particle transport is mainly driven

[1]The magnetic shear s is defined as $s(r) = \frac{r}{q(r)} \frac{dq(r)}{dr}$. It plays an important role in stabilizing MHD instabilities, particularly those driven by the pressure gradient. This parameter diverges at reversal surface.

by electrostatic fluctuations (see for example [26, 27, 28]) although these fluctuations do not account for the total particle flux at the edge. Energy transport instead is still an open question as electrostatic fluctuations can account for about 30% of the total lost power [29].

This thesis reports about recent observations and theoretical interpretations of the effects of spontaneous and applied magnetic perturbations at the edge region of RFX-mod, operated both as a reversed-field pinch and as a circular ohmic tokamak.
For the tokamak case, the flexibility of the RFX-mod MHD control system allows operational regimes with $q_a \gtrsim 2$.
In both configuration a large modification of the plasma flow is observed, with a velocity pattern recognizable around the edge of magnetic islands and generating local density accumulation/convection with a consequent modification of local gradients. Variation of flow and gradients are found to deeply affect the properties of small scale electrostatic fluctuations: these are in turn responsible of a modulation of perpendicular and parallel transport with consequent turbulence induced particle losses [60].

Before we turn to discuss the results, let us clarify the different experimental configurations used to operate RFX-mod and the means of investigating the plasma edge, the insertable probe *U-probe*, together with the theory upon which the collection of measurements relies, the *Debye sheath theory*.

3.1 Experimental configurations for RFX-mod

3.1.1 RFP configuration

Up to this point we know that at high plasma currents (greater than 1 MA) the RFP exhibits a transition from a dynamic regime of Multiple Helicity states (MH mode) towards a helical equilibrium set by a single mode, the Single Helicity (SH) state. The amplitude of this mode is sufficient to modify the flux surfaces, creating a helical core with a reduced chaos, surrounded by a quasi-symmetric boundary. It has been found [61] that in this helical regimes the helical ripple at the edge is relatively small, of the order of 1% of the total field, but still sufficient to spatially modulate local transport and kinetic properties [35, 61, 62].

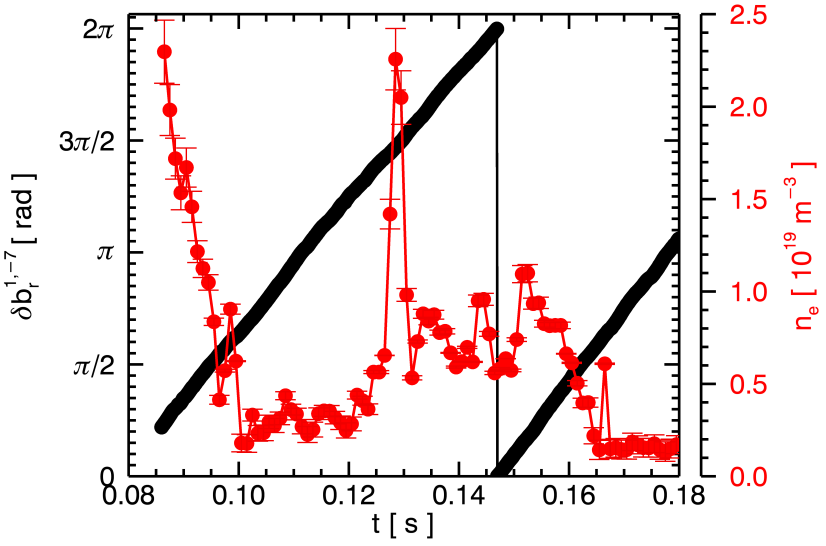

FIGURE 3.1: For the discharge # 35755, in black we show the phase of the radial component of the externally applied magnetic field as a function of time, while in red we plot the electron density as a function of time, signal reconstructed through the *U-probe* and resampled at 1 kHz. In the δb_r profile we can observe a complete rotation of the mode ($m = 1$, $n = -7$).

In order to investigate the main features of transport and its effects on the plasma-wall interaction, insertable probes are extremely useful: in RFP configuration experiments, the insertable *U-probe* was exploited in low current discharges (with $I_p \leq 450\ kA$) with an helical boundary ($m = 1$, $n = -7$), externally applied via the saddle coils

feedback system. In this way it is possible to mimic a high current configuration and have a better "topological" control on the discharge.

Experimentally, the boundary is a magnetic perturbation that toroidally rotates with frequencies of the order of 10-15 Hz: in Figure 3.1 we show the profile of the perturbation's phase $\delta b_r^{1,-7}$ (in black) together with the local electron density (in red) as a function of time for the discharge # 35755, where the probe has been inserted 1.5 cm in the chamber.

In Figure 3.2 we show the typical profiles of plasma current, density and the reversal parameter set for the analyzed RFP discharges.

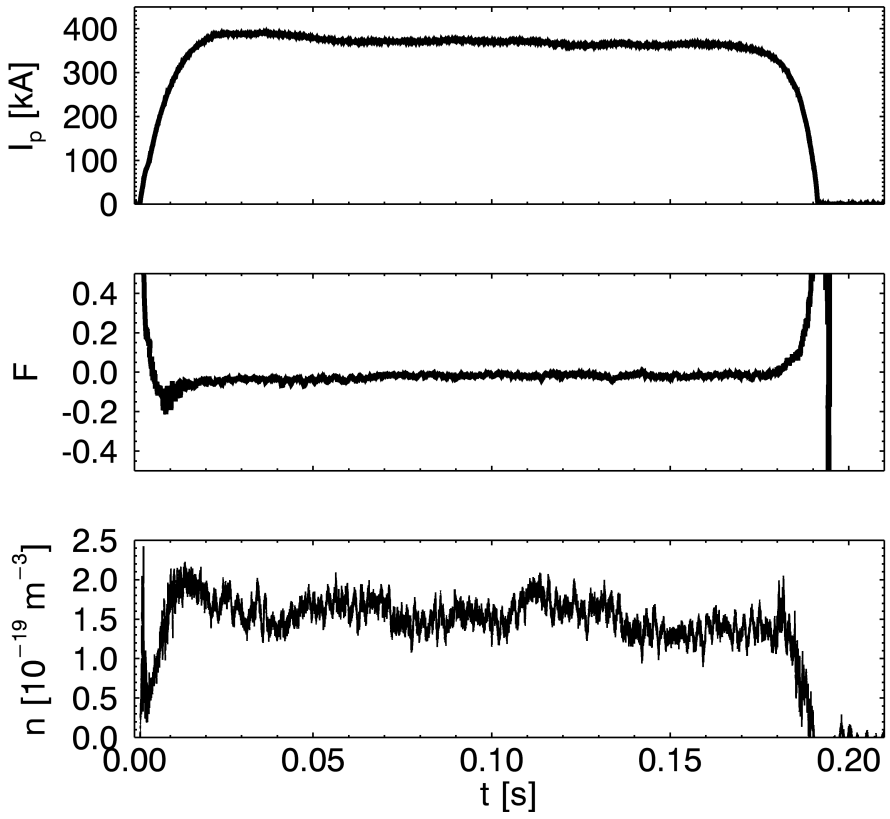

FIGURE 3.2: In the three panels we reported the plasma current I_p, the value of the reversal parameter F and the density obtained by the interferometer n for a typical RFP discharge analyzed, in this case discharge # 35755.

Data reported hereafter have been extracted from discharges with $I_p \lesssim 450\ kA$, normalized Greenwald fraction $n/n_{Gr} \simeq 0.3 - 0.4$ and edge safety factor $q_a \approx -0.004$. All the analyzed RFP discharges share the same "shallow" equilibrium, with a common reversal parameter F of the order of $F \sim -(0.01 - 0.02)$.

Measurements are always referred to the flat top phase of the plasma current.

3.1.2 Tokamak configuration

In addition to RFP operation, RFX-mod can routinely operate as a low-current ohmic circular tokamak with the first wall representing the limiter [63]. The maximum plasma current achieved is $I_p = 0.15\ MA$, with a maximum toroidal magnetic field $B_\phi = 0.55\ T$, corresponding to an edge safety factor $q_a = 1.7$.

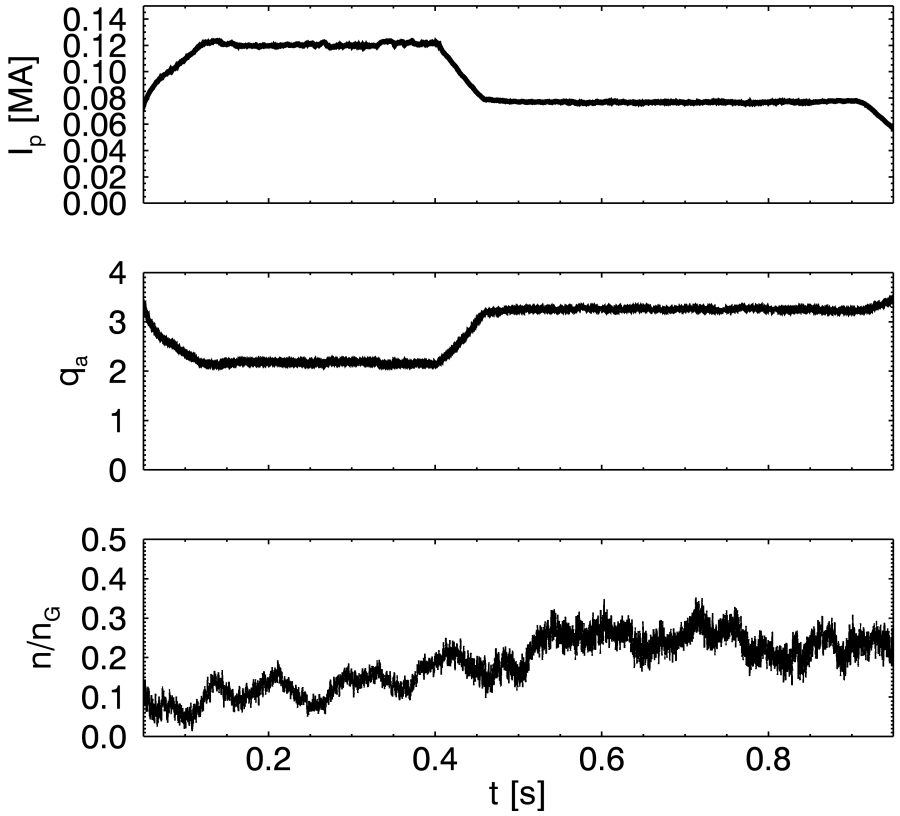

FIGURE 3.3: In the three panels we reported the plasma current I_p, the value of q_a and the normalized Greenwald fraction n/n_G for a typical tokamak discharge, in this case discharge # 35555. Measurements extracted from the *U-probe* are referred to the flat top phase of I_p in the first part of the discharge.

This low-q operations were made possible only by means of a feedback control on the ($m = 2$, $n = 1$) mode, that resonates close to the wall and would otherwise grow too large and disrupt the discharge. The representative discharge taken here into account for the analyses, exhibits a controlled variation from $q_a \simeq 2.1$ to $q_a > 3$ obtained by decreasing the plasma current. The flexibility of the MHD control system has allowed to vary the helical boundary condition within the same discharge with a (2, 1) radial perturbation during the $q_a < 3$ phase, whereas in the $q_a > 3$ a magnetic perturbation on modes with the same toroidal periodicity (both $n = 1$ and $n = 2$) and poloidal

mode numbers $m = -1, 0, 1, 2$ has been applied. This produces a perturbation of the magnetic field with a bulging of the plasma towards the external equatorial plane, similar to the one obtained with the so-called C-Coils in DIII-D [48].
In Figure 3.3 we show the typical profiles of plasma current, n/n_G and the safety factor profile at the edge, imposed for the tokamak discharges.
For the aim of this thesis, we will show the results obtained by analyzing and reconstructing the topology in the first part of a typical tokamak discharge in RFX-mod, with $q_a \simeq 2.1$. The representative chosen discharge is the $\#\ 35555$, whose operational parameters can be seen in Figure 3.3: between $0.2\ s$ and $0.4\ s$ a resonating perturbation (2, 1) is applied through feedback control with a rotation frequency of 10Hz.

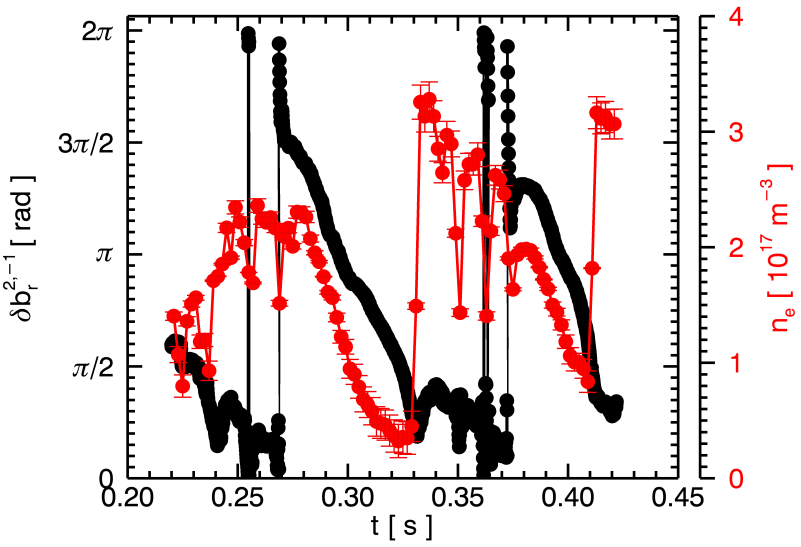

FIGURE 3.4: For the discharge #35555 we plot the phase of the radial component of the externally applied magnetic field as a function of time for the discharge. It is possible to see two complete rotations of the ($m = 2$, $n = -1$) mode, while in red we overplot electron density as a function of time; the signal is reconstructed through the *U-probe* resampled at 1 kHz (original sampling frequency for the tokamak case is 2.5 MHz). For this discharge the probe was inserted 3 cm in the chamber.

In Figure 3.4 we show the phase of the radial component of the externally applied magnetic field as a function of time, together with the edge electron density signal resampled at 1kHz.

3.2 U-probe

The study of edge plasma transport properties requires measurements with high spatial and temporal resolution. This can be obtained using insertable probes, though the main disadvantage is that the probes perturb the plasma and the interpretation of the measurements can be in some cases difficult.

We will now describe the insertable *U-probe* [64] used to carry on transport analyses on RFX-mod. The *U-probe* can be inserted both in reversed-field pinch and in tokamak configuration, only in low current discharges to avoid excessive heat load and damage to its components. It provides detailed information about electrostatic and magnetic fluctuations in the boundary region of the plasma. In particular, it can be inserted radially up to 5 cm in the chamber and in our experiments it is located at fixed poloidal and toroidal position, $\theta = 0°$ and $\phi = 247.5°$.

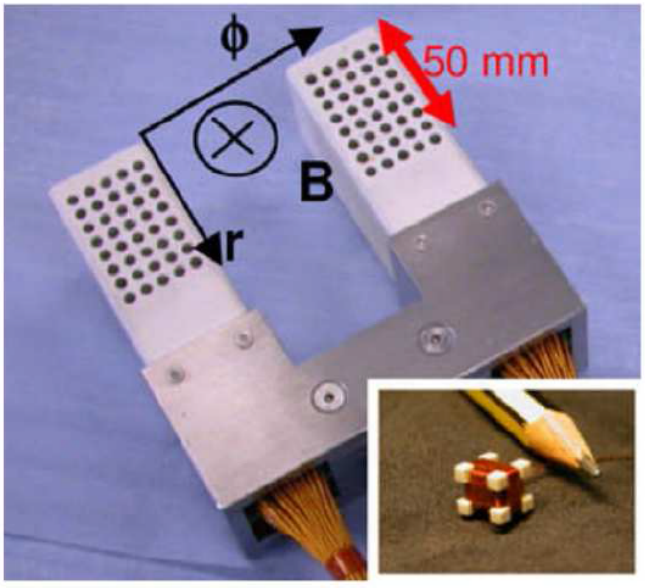

FIGURE 3.5: Picture showing the U-probe and a magnetic sensor. In figure it is also indicated the probe orientation with respect to the toroidal and radial reference machine system and to B_θ in case of RFP configuration.

The probe consists of two fingers, 88 mm apart each other along the perpendicular direction[2], each equipped with a 2D array of electrostatic pins of 3 mm of diameter with a radial and toroidal resolution of 6 mm. Inside each finger, a radial array of

[2]This is true considering the RFP case. In the tokamak configuration the probe is rotated of $90°$ according to the cross-field.

3-axial magnetic probes has been placed, having the same resolution of the electrostatic system: a picture of the probe is shown in Figure 3.5. The electrostatic pins have been arranged in order to obtain information simultaneously and in the same location on plasma density, electron temperature and floating potential as well as on their respective radial gradient. Both electrostatic and magnetic probes are digitally sampled with a $0.2\ \mu s$ of time resolution[3], with a minimum bandwidth of 700 kHz.

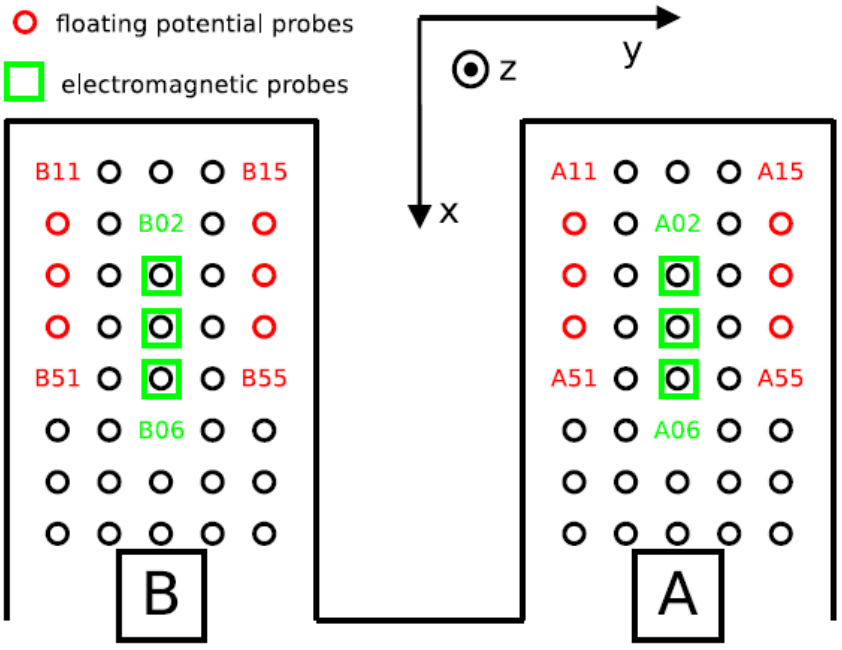

FIGURE 3.6: U-probe scheme and labels of the acquired pins. Here the triplet (x, y, z) stands for a general coordinate system.

The scheme of the probe with a detailed labeling of the pins is reported in Figure 3.6; on each row the pins are arranged accordingly to a five-pins balanced triple probe [65]. This configuration, that is at the basis of *Langmuir* probes, gives us the possibility to extract information about fluctuations of electron temperature and density since we obtain local measurements of floating and positive potential plus saturation current thanks to the *Debye sheath* theory. In the following we give a simple description of the probe theory.

3.2.1 The Debye sheath

The capability of screening out electrical charge is a characteristic feature of plasmas. When a conducting probe is put in contact with the plasma, it feels an ion and electron

[3]For the tokamak case the sampling frequency is halved due to longer discharges.

flux. If this object is electrically insulated, it can't carry away a net current from the plasma, so in stationary conditions the probe will get an equilibrium electric potential which allows to balance the incoming flux of ions and electrons. This equilibrium potential is the *floating potential*. This quantity is relatively simple to be measured, and in plasma experiments this kind of measurements are collected with a sampling frequency of the order of MHz.

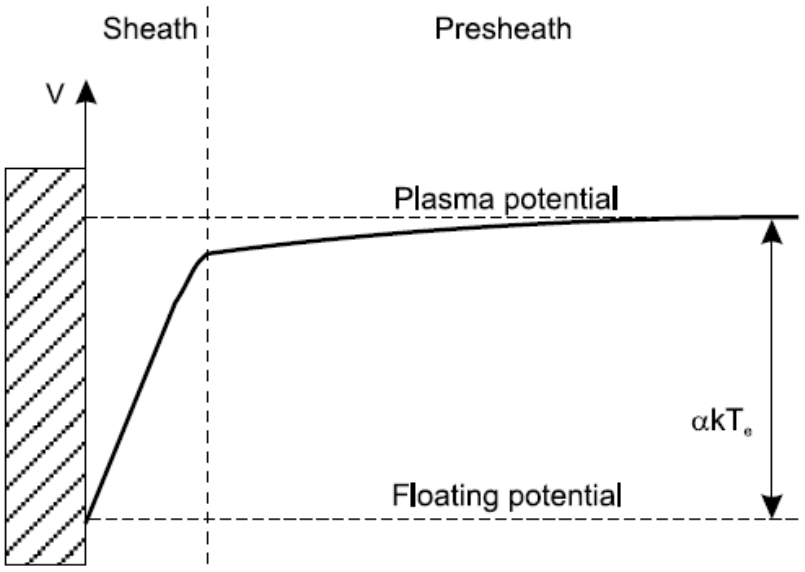

FIGURE 3.7: Schematic figure of the potential distribution in front of a floating probe.

When a conducting object is faced to the plasma, it will accumulate a charge cloud whose typical dimension is defined by the *Debye length* in Equation A.1. The object will initially collect a stronger electron flux than an ion one due to the mass difference between the species and an eventually higher temperature for electrons rather than ions. The main part of the charge difference between the solid and the plasma will be confined to a narrow sheath region restricted to some Debye lengths in thickness. The potential distribution is shown schematically in Figure 3.7. Outside the sheath there is a volume with a weaker electric field called the *pre-sheath* region. Ions are accelerated in the pre-sheath towards the probe. The sheath edge is defined as the surface where the ions reach the sound speed velocity c_s:

$$c_s = \sqrt{\frac{T_e + T_i}{m_i}} \tag{3.2}$$

The Poisson's equation, $\nabla^2\phi = \frac{e(n_e - n_i)}{\epsilon_0}$ with n_e and n_i the electron and ion density distributions, is the one that allows to calculate the electric potential profile within the sheath by matching its solution in the sheath and pre-sheath. Coming to the Bohm sheath criterion for the ion current entering the sheath, $v_{i,sheath} = c_s$, the current density will be consequently equal to the ion saturation current density j_{sat}:

$$j_{sat} = \zeta e n_e c_s \tag{3.3}$$

The constant ζ is linked to the ratio between the ion density at the sheath edge and in the background plasma. In an ideal case with no collisions, ionization and recombination in the pre-sheath we have ζ approximately equal to $1/2$ [66].
Since electron drift velocity is much smaller than the thermal one, a Maxwellian distribution function can still be adopted. Therefore, electrons will closely follow the Boltzmann relation [66]:

$$n_e = n_0 \; exp\left(\frac{e(\phi - \phi_P)}{T_e}\right) \tag{3.4}$$

where n_0 is the plasma density far away from the probe where the space potential of the plasma is $\phi = \phi_P$. It can be shown that plasma potential ϕ_P is related to the floating potential ϕ_f, the potential adopted by a floating probe when the probe current is zero [66]:

$$\phi_P = \phi_f + \alpha T_e \tag{3.5}$$

The voltage drop in the plasma sheath is consequently proportional to the electron temperature. The coefficient α can be calculated and varies generally between 2 - 3 depending on probe geometry, type of plasmas etc. [67]. All the previous equations are derived under the assumption of zero ion temperature and no magnetic field. It is also assumed that all electrons that hit the probe surface are absorbed. In particular, the effect of the magnetic field is determined by the relation between of the Larmor radii (Equation 1.4) of ions ρ_i and electrons ρ_e respectively to the probe dimension d. In the RFP edge a good approximation is $\rho_e \ll d \ll \rho_i$. The main effect will be the variation of the collection area of the electrons that will result the projection of the probe along the magnetic field [66].

The U-probe exploits a modified triple-probe technique called *five-pins balanced triple probe* that has the advantage of reducing phase-shift problems between the signals. This probe technique gives a reliable measurement of electron temperature with a fixed

bias [65, 68]. The triple probe uses a floating double probe together with a single probe tip measuring the floating potential. When the double probe is biased to saturation, i.e. $\phi \gg T_e/e$ the potential of the positive leg will be:

$$\phi_+ \approx \phi_f + ln3\ T_e \tag{3.6}$$

So electron temperature may be calculated from measurements of ϕ_+ and ϕ_f.

3.3 RFP: spectral analysis

In the next sections we are going to show and discuss the results obtained by analyzing electrostatic fluctuations of electron temperature, density and therefore particle and energy fluxes extracted through the U-probe, first in RFP and then in tokamak configuration experiments.
In RFP configuration, it has been possible to obtain a detailed analysis of the radial profiles of the fluxes driven by electrostatic fluctuations, since the experimental campaign has provided enough statistics at different radial insertions of the *U-probe*.

The formula to which we refer in order to obtain the electrostatic particle flux is the following [69]:

$$\Gamma_{es} = \langle \tilde{v}_r \tilde{n}_e \rangle = \frac{\left\langle \tilde{E}_\phi \tilde{n}_e \right\rangle}{B_\theta} \tag{3.7}$$

$\tilde{n}_e$ stands for the electron density fluctuations, while $\tilde{v}_r$ is the radial velocity field. $\tilde{E}_\phi$ are the fluctuations of toroidal electric field and remember that at the edge of a RFP device we have a dominant poloidal magnetic field B_θ (see Figure 1.7).
For the electrostatic energy flux stands:

$$Q_{es} = \frac{3}{2} \langle \tilde{v}_r \tilde{p}_e \rangle = \frac{3}{2} \frac{\left\langle \tilde{E}_\phi \tilde{p}_e \right\rangle}{B_\theta} \tag{3.8}$$

where $\tilde{p}_e = \tilde{n}_e \tilde{T}_e$.
A detailed discussion on transport relevant equations is reported in Appendix B.
Since it is our interest to investigate the fluxes in the frequency domain, we can recall that the decomposed electrostatic particle flux in the Fourier space can be extensively

written as [69]:

$$\Gamma_{es} = \frac{2}{B}\int_0^\infty k_\perp(\omega)\bar{n}(\omega)\bar{\phi}(\omega)\gamma_{n\phi}(\omega)sin\alpha_{n\phi}(\omega)d\omega \tag{3.9}$$

where $\bar{n}$ and $\bar{\phi}$ are the square root of the power spectra of density and plasma potential fluctuations, while $\gamma_{n\phi}$ is the coherence between density and plasma potential, $\alpha_{n\phi}$ is their relative phase and $k_\perp$ is the transverse wave number of the plasma potential fluctuations.

We will first consider the radial profiles of the fluxes in presence of applied magnetic perturbations of definite $(m,\ n)$: they are shown in Figure 3.8 and are obtained moving the probe from shot to shot at a different radial insertion in the chamber.

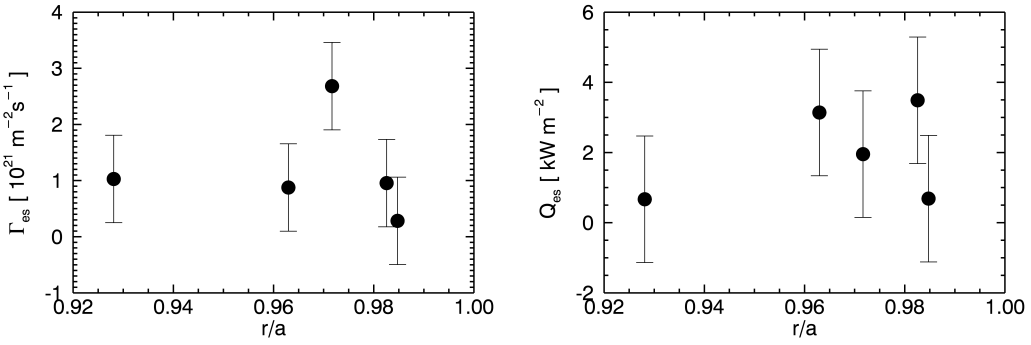

FIGURE 3.8: Radial profiles of electrostatic particle flux (left panel) and electrostatic energy flux (right panel). The radius is normalized to the chamber radius $a = 0.459\ m$. Errors are obtained as the root mean square of measured values.

The particle flux exhibits a maximum value of $\Gamma_{es} \simeq 2.5 \cdot 10^{21}\ m^{-2}s^{-1}$ at about $r/a \sim 0.97$. The decrease in the innermost region may be attributed to the decrease in the source term (i.e. hydrogen/deuterium influx from the wall) [27] while the decay in the region $r/a > 0.97$ may be attributed to the wall proximity which affects the particle balance by parallel losses to the wall due to plasma column shifts, field error or MHD instabilities. The radial profile for the energy flux Q_{es} can be explained in analogy with the particle flux profile.

According to Equation 3.9 the particle flux has been computed in the Fourier space. In Figure 3.9 we show the fluxes spectra as a function of frequency: for frequencies greater than 300 kHz the contributions to both fluxes tend to zero.
Both particle and energy transport are mainly concentrated in the range $30\ kHz \leq$

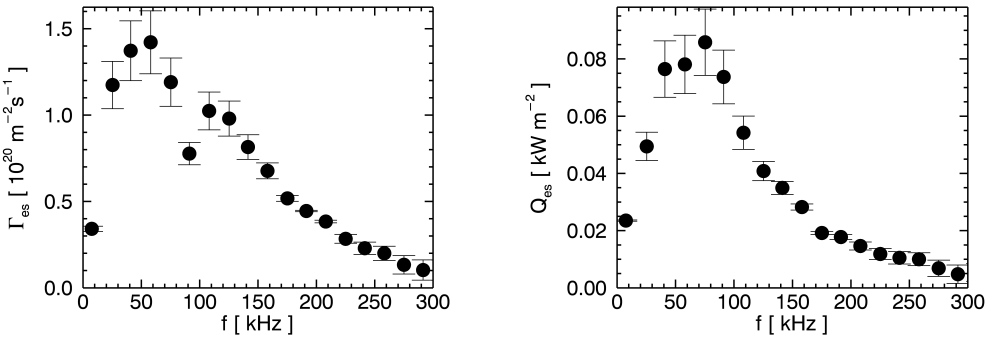

FIGURE 3.9: Profile of electrostatic particle flux (left) and profile of electrostatic energy flux (right) as a function of the frequency for an ensemble of different shots, all at $r/a \approx 0.97$.

$f \leq 150\ kHz$ with a clear maximum around $f \simeq 60\ kHz$. The data shown are the result of an average performed over different discharges with similar plasma parameters, and are referred to the same radial insertion of $r/a \approx 0.97$, in the proximity of the maximum of the radial profile of Γ_{es}.

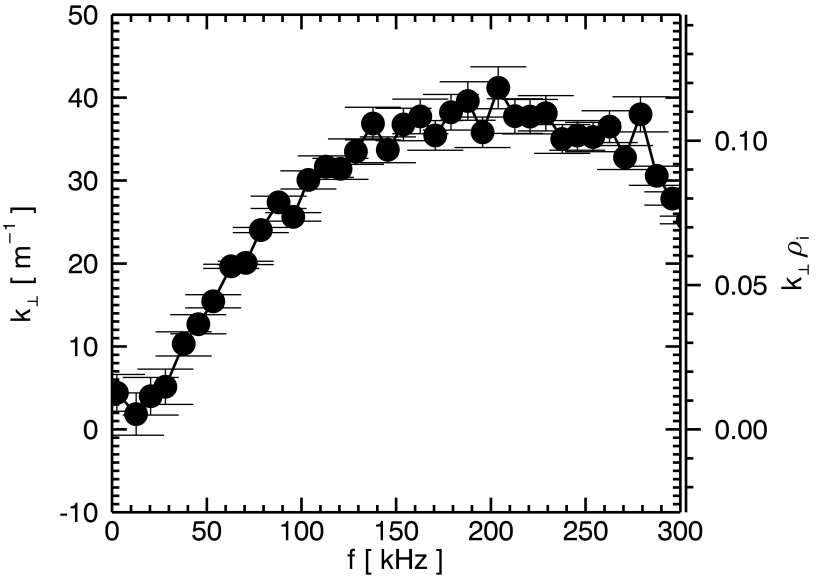

FIGURE 3.10: Perpendicular wave number $k_\perp$ versus the frequency relevant for particle transport. A secondary y-axis is drawn, where $k_\perp$ is multiplied by the ion Larmor radius. Collected data refer all to the same insertion $r/a \approx 0.97$.

Fluxes are then analyzed as a function of the transverse wave number $k_\perp$, derived

from two points measurements of floating potential in the toroidal direction. The perpendicular wave number is actually shown as a function of the associated frequency relevant for particle transport ($f \leq 300\ kHz$) in Figure 3.10. A secondary vertical axis is also plotted, were the wave number is multiplied by the ion Larmor radius ρ_i[4], which for the considered discharges is of the order of $\rho_i \sim 2 - 3\ mm$.

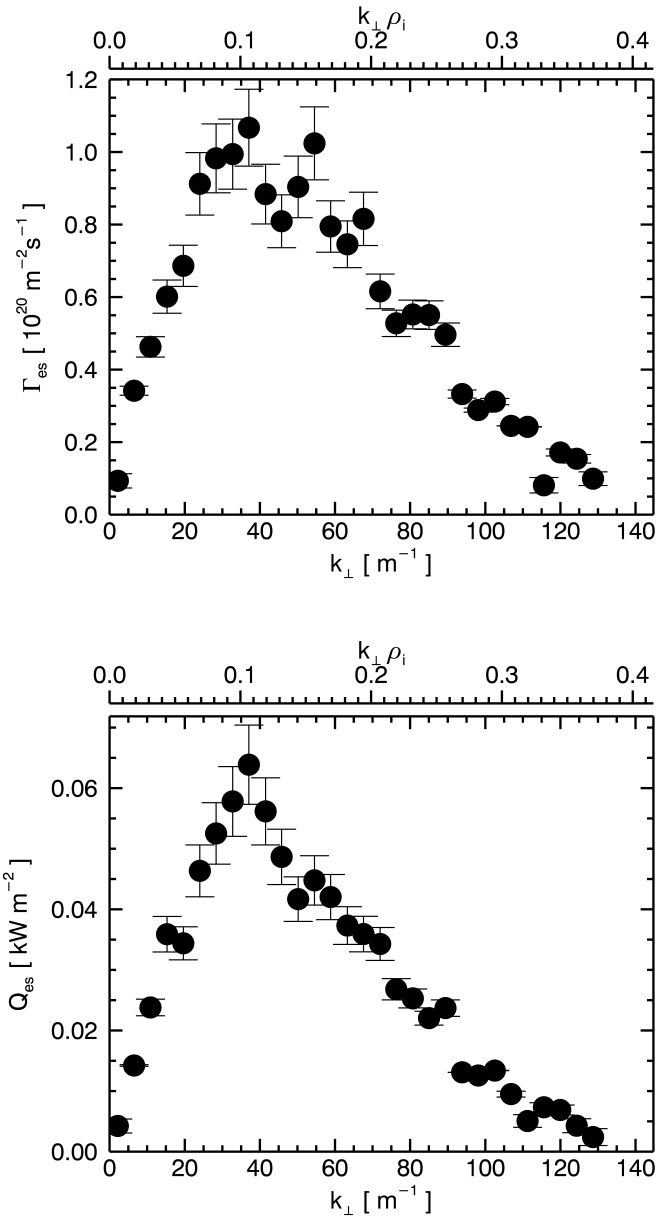

FIGURE 3.11: We show in the upper panel the profile of electrostatic particle flux and the profile of electrostatic energy flux in the lower one as a function of the transverse wave number $k_\perp$. Plus, we draw a secondary x-axis where $k_\perp$ is multiplied by the Larmor radius ρ_i for an ensemble of different shots, all at $r/a \approx 0.97$.

[4]See Equation 1.4.

From the behavior of $k_\perp$ as a function of frequency it is possible to extract a dispersion relation from which we can further estimate a phase velocity for the fluctuations.
Before discussing the dispersion relation, we consider the wave number decomposition of particle and energy flux whose profiles are visible in Figure 3.11. We can say that both energy and particle transport driven by electrostatic fluctuations are concentrated in the range $20\ m^{-1} \leq k_\perp \leq 60\ m^{-1}$ with a maximum peaked around $k_\perp \sim 40\ m^{-1}$. In Figure 3.11 we show the fluxes versus the wave number and a secondary x-axis is plotted where $k_\perp$ is multiplied by ρ_i: we can evince that the fluxes have peaks around $k_\perp \rho_i \sim 0.1$.

From Figure 3.10 we can estimate a phase velocity for the fluctuations of $v_{phase} \sim 9.5\ km\ s^{-1}$. Furthermore, we know that v_{phase} of the fluctuations (and therefore the related $k_\perp$) propagates in the same direction of the electron diamagnetic velocity term[5] defined by [70]:

$$\mathbf{v}_{*,\mathbf{e}} = \frac{\nabla p_e \times \mathbf{B}}{e n_e B^2} \tag{3.10}$$

Considering only the contribution coming from the density gradient and neglecting the temperature one, we can give an estimate also for this velocity using the local edge measurements of temperature and density obtained through the U-probe: $v_{*,e} \sim 2\ km\ s^{-1}$.

Another comparison can be done with the $\mathbf{E} \times \mathbf{B}$ term which for the RFP analyzed discharges gives the velocity:

$$v_{\mathbf{E}\times\mathbf{B}} = \frac{\mathbf{E} \times \mathbf{B}}{B^2} = -\frac{E_\phi}{B_\theta} \tag{3.11}$$

The value obtained when substituting local measurements gives us: $v_{\mathbf{E}\times\mathbf{B}} \sim 22\ km\ s^{-1}$. Here the electric field is obtained using the gradient of plasma potential following the expression in Equation 3.5, as we will discuss in the next section.
We can therefore conclude that the fluctuations tend to propagate in the same direction of the electron diamagnetic flux but with a higher velocity although lower than the $\mathbf{E} \times \mathbf{B}$ one. This latter observation might actually be a first rough approximation, since the extrapolated dispersion relation from the profile in Figure 3.10 is strongly dependent on the fit technique used to extract the phase velocity.

[5] The associated *diamagnetic current* generally acts to reduce the magnitude of the magnetic field inside the plasma; so it contributes to force balance and also gives rise to ohmic heating.

3.4 RFP case: transport in O-point and X-point regions

Recalling what we understood in Section 2.6, results coming from experiments on TEXTOR-DED with RMP coils, either with static and rotating fields show a modulation of local profiles of electron temperature, density and therefore pressure. The cause relies on the emergence of a stochastic layer imposed to the plasma edge, which consists of three topological profiles with different transport properties. Referring to the topology illustrated in Figure 3.12, if the RMP field penetrates enough, magnetic islands can be formed with the presence of fast particle and heat transport parallel along field lines around the island's O-point.

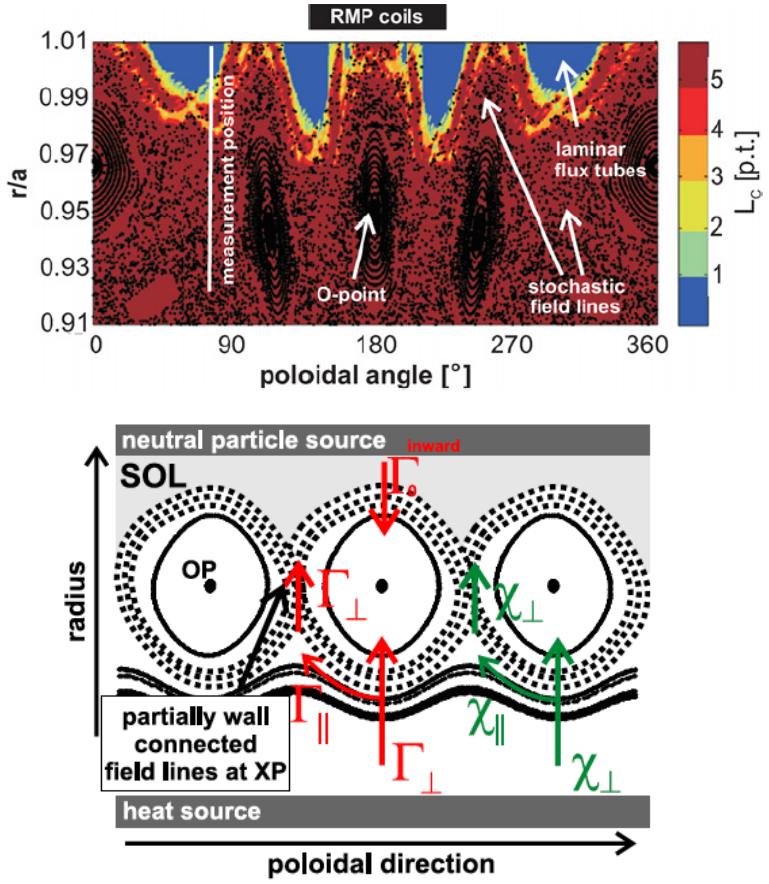

FIGURE 3.12: Upper panel: edge magnetic topology calculated in vacuum approximation for a static RMP field. The complete connection length L_c in poloidal turns is displayed color-coded and the field line distribution as a Poincaré plot. Lower panel: conceptual sketch of the parallel and perpendicular transport properties around a remnant island in close contact with the SOL. Figures are taken from [58].

In the more external buondary, island chains from neighboring rational flux surfaces

overlap and form a region with ergodic, stochastically distributed field lines that lead to an increased, diffusive radial transport around the island's X-point.
In the radially outermost region, field lines with short connections to the wall are coherently bundled to the laminar flux tubes, which lead to a strong local reduction in electron density and temperature due to fast parallel particle transport to the wall.

In RFX-mod, the connection length is used to characterize the properties of the edge in presence of $m = 0$ islands, even though it retains some limitations of a traditional 2D treatment. Previous studies have shown that in QSH/SHAx discharges L_c follows the same $n = 7$ periodicity of the dominant helical equilibrium [61].
Since we cannot insert the probe in high current regimes due to the high power load, in RFP configuration our experiments are performed in a MH substrate upon which an external magnetic perturbation is superimposed with a rotation frequency of the order of 10-15 Hz. Nevertheless, it is possible to find that the behavior of connection lengths is analogous to that obtained in QSH experiments.
In Figure 3.13 we show in the upper panel the L_c profile as a function of the toroidal angle for a representative discharge, while in the lower panel we have a Poincaré plot in the plane (r, ϕ) zoomed at the edge region, for $0.36\ m \leq r \leq 0.46\ m$. The Poincaré plot is obtained through the FLiT code [34] and the color code follows the values of connection lengths in the considered spatial region; though the existence of a much richer magnetic topology, we have limited the spectrum included in the map computation to highlight the space relation with respect to the dominant periodicity. L_c is then extracted from FLiT and the data are presented at two different radial positions around the position of the probe in the discharge ($r_{probe} = 0.446\ m$) and coherently reported also in the Poincaré map as the red and cyan dashed lines.
As we can see, the L_c modulation is affected by the local topology and can abruptly change from one radial position to the other, depending also on the encountering of the last closed flux surface, whose location is between the $m = 0$ chain and the yellow ergodic region, defined by long connection lengths to the wall. In analogy with the topology characterization in TEXTOR-DED, the $m = 0$ islands here play the role of the remnant islands and in between them short connection length regions mark the laminar zone.

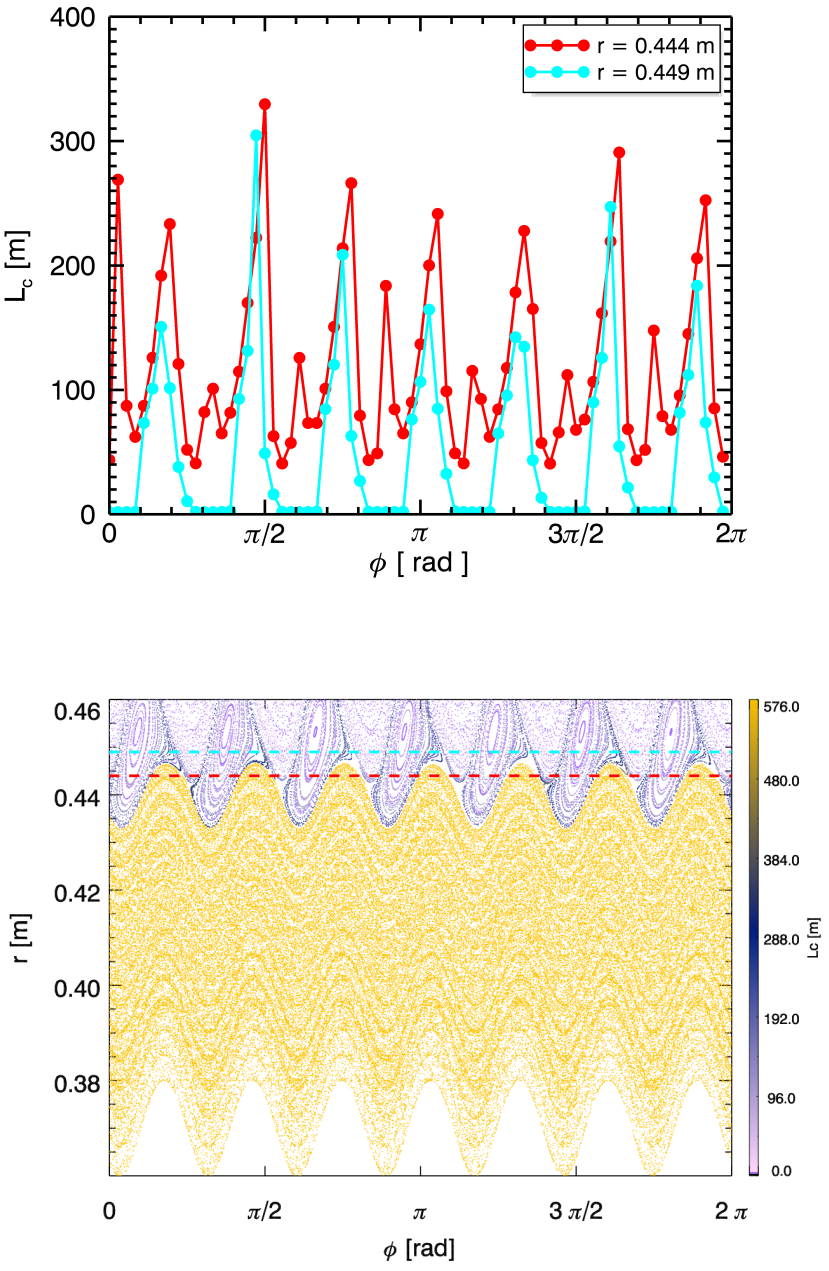

FIGURE 3.13: Upper panel: for the discharge #35755 connection length profile as a function of the toroidal angle obtained through the field line tracing code and extracted at two different radial position. Lower panel: corresponding Poincaré plot for discharge #35755 at $t = 0.139\ s$ obtained solving Newcomb's eigenfunctions for the dominant ($m = 1$, $n = 7$) mode and the toroidal coupled $m = 0$ component. In red and cyan, the dashed lines represent the radial positions at which we extracted the L_c profiles shown in the upper panel.

In presence of a rotating (m, n) magnetic perturbation (MP) plasma parameters measured by the diagnostic placed at a fixed position on the device, exhibit a sinusoidal time evolution: this translates in an oscillatory behavior of the PWI as a function of time that can be better understood whenever the modulation on fluctuating values of transport properties is considered as a function of the local *helical angle*, previously described in paragraph 2.4.3.

We consider a statistics given by an ensemble of discharges where the probe has been radially inserted at $r/a \approx 0.97$, since it corresponds to a maximum in the radial profiles of the electrostatic fluxes visible in Figure 3.8.

The profiles we will show are the result of a final re-sampling of the signals collected by the U-probe. Once the signals have been resampled at 1 kHz (the original sampling frequency is 5 MHz), they are averaged and then related to the averaged values of the perturbation. The errors are obtained by the standard deviation of the mean; where the error bars are not clearly visible they are of the same width of the symbol used in the plot.

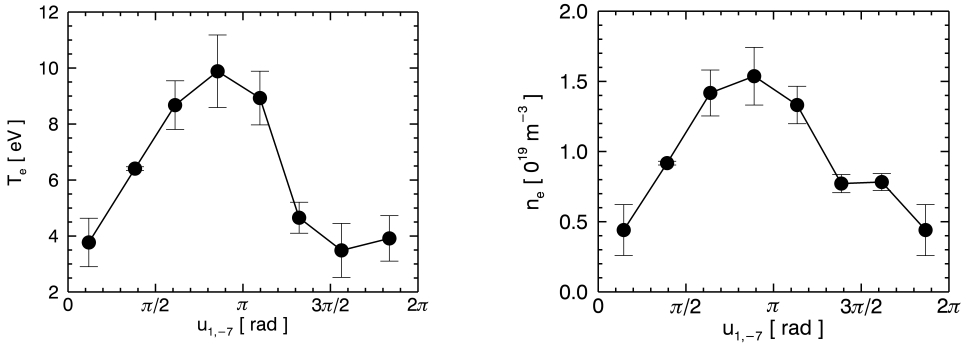

FIGURE 3.14: Electron temperature (left) and density (right) as a function of the helical angle $u_{1,-7}$, for an ensemble of different shots all at $r/a \approx 0.97$.

In Figure 3.14 we can see that both electron temperature and density show an oscillating behavior along the helical angle with a maximum in the region $\pi/2 \leq u_{1,-7} \leq \pi$ and a minimum around $u_{1,-7} \sim 3\pi/2$, corresponding to different topological regions, as we will soon demonstrate. It is worth to remind that this modulation is also observed on the entire edge profile: previous studies [30, 71] have reported that the perpendicular flow is modulated along the helical angle, and this has been confirmed independently from the helicity of the dominant perturbation. Owing to the small contribution coming from the diamagnetic flow, the observed velocity modulation reflects the modification of the radial electric field, which has been theoretically explained in terms of ambipolar constraints [30, 71].

In our studies, the radial component of the electric field is directly computed as

$$\tilde{E}_r = -\frac{\partial}{\partial r}\,\phi_P \tag{3.12}$$

where ϕ_P is the plasma potential obtained by Equation 3.5 at different radial insertions in the same discharge.

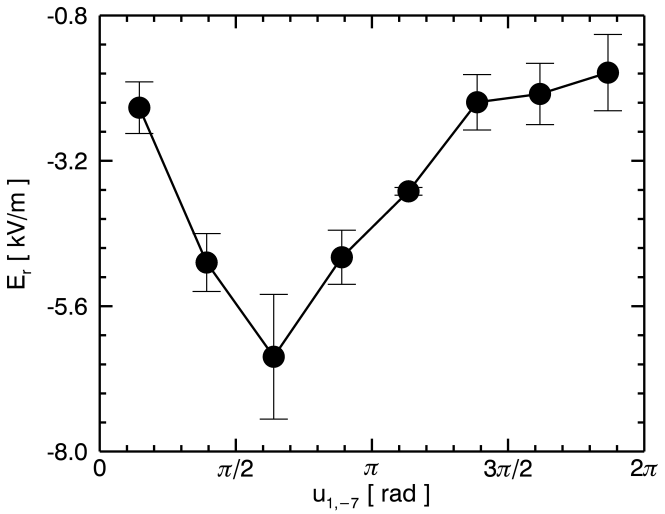

FIGURE 3.15: Radial electric field as a function of the helical angle $u_{1,-7}$, for an ensemble of different shots all at $r/a \approx 0.97$. From this profile we can extract an estimate for the $\mathbf{E} \times \mathbf{B}$ velocity term: $v_{\mathbf{E}\times\mathbf{B}} \sim 22\ km\ s^{-1}$.

In Figure 3.15 E_r profile as a function of the helical angle is shown. A negative peak in the region $\pi/2 \leq u_{1,-7} \leq \pi$ can be interpreted in analogy with the ambipolar potential theory as an accumulation point of local electron density [30]. Actually, particle species behave differently in presence of a magnetic ripple or magnetic islands, with electrons strictly following magnetic field lines due to their smaller drift. The appearance of a point of density accumulation has been seen to cause a radiative collapse of the discharge in high density experiments where it has actually been shown [30] that the modulation of the flow causes a reversal in a toroidal sector of the machine, also due to the presence of a macroscopic $(m = 0,\ n = 1)$ island.

A cautionary remark should be done regarding the experimental scenarios: our configuration contemplates low current discharges where the edge dominant symmetry is given by the $(m = 0,\ n = 7)$ mode. Even though the experimental scenario completely differs, experiments show that magnetic islands spontaneously resonating in

the reversed-field pinch are associated with macroscopic fluctuations of the flow (up to $\approx 20\ km\ s^{-1}$), with the same symmetry as the generating island.

3.4.1 Transport driven by electrostatic fluctuations

Recalling the *Fick's law*, we can define the *radial diffusion coefficient* as the fraction of electrostatic flux over the electron density gradient:

$$D_{es} = -\frac{\Gamma_{es}}{\nabla n_e} \tag{3.13}$$

Consequently, we can also exploit the definition of the *Bohm diffusion coefficient*, in order to get a comparison between the effective diffusion coefficient and the parameter that characterizes anomalous transport:

$$D_{Bohm} = \frac{1}{16}\frac{T_e}{eB} \tag{3.14}$$

where $B = B_\theta$ since at the edge of a RFP device the field is mainly poloidal, while for the tokamak analysis we shall substitute the toroidal component of the magnetic field.

In order to better understand why transport profiles change and what is the underlying topology when resonant and not resonant MPs are applied, we can exploit Poincaré maps of the edge. These are obtained through the field line tracing code FLiT, whose description we have given in paragraph 2.4.2.
A detailed magnetic reconstruction of the edge region is given in Figure 3.16.
The modulation due to the ($m = 1$, $n = -7$) perturbation is clearly visible, together with the details of secondary $m = 0$ islands, the main one centered at $u_{1,-7} = \pi$.
In the upper panel of Figure 3.16 we show the profile of particle flux driven by the electrostatic fluctuations, $\Gamma_{es} =< \tilde{v}_r \tilde{n}_e >$, as a function of $u_{1,-7}$. It is possible to evince that the average profile of Γ_{es} shows the same periodicity of the applied MP.
In particular, the flux shows a peak in the region $\pi/2 \leq u_{1,-7} \leq 3\pi/2$ and if we compare this result to the Poincaré map, the peak corresponds to the region where the O-point of the externally applied magnetic perturbation lies.
From Figure 3.16 we can draw an important conclusion: we can witness a reduction or an enhancement in radial transport properties depending on the magnetic topology and this is confirmed also by the modulation on the profile of the diffusion coefficient

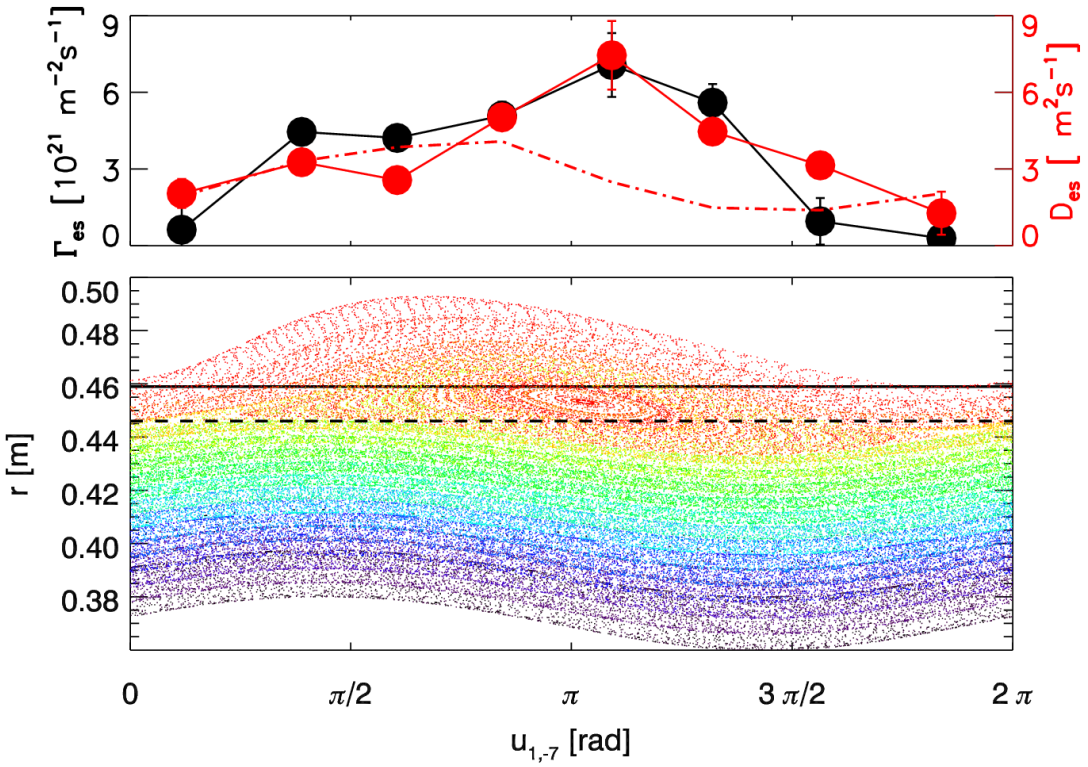

FIGURE 3.16: Poincaré plot in the plane $(r, u_{1,-7})$ for the discharge #35755 at $t = 0.139$ s, instant chosen in correspondence of a maximum of the externally applied perturbation $(m = 1, n = -7)$. The color code is arbitrarily chosen depending upon the starting values of the radial coordinate of the magnetic field lines. Above the Poincaré plot, the profiles of particle flux (black) and perpendicular diffusion coefficient (red) are displayed as a function of the helical angle. The red dot-dashed line stands for the Bohm diffusion coefficient. Although these profiles are extracted for just one discharge, they follow the pattern of all the ensemble at $r/a \approx 0.97$.

(the red line in the upper panel). A further information given in Figure 3.16 is represented by the comparison between D_{es} and the Bohm coefficient (the red dot-dashed line). We can see a slight change in the prevalent transport mechanism whether we consider transport around $u_{1,-7} \sim \pi/2$ or $u_{1,-7} \sim 3\pi/2$, which correspond to the O- or X-point of the dominant mode.

We now analyze the profile of the electrostatic energy flux Q_{es} as a function of the helical angle and we discuss it in analogy to the particle flux behavior. In Figure 3.17 we show Q_{es} together with the convective contribution (in red) and we can see in both profiles a peak in the region corresponding to the O-point of the island, where $\pi/2 \leq u_{1,-7} \leq 3\pi/2$, and a consequent reduction where $u_{1,-7} \geq 3\pi/2$.

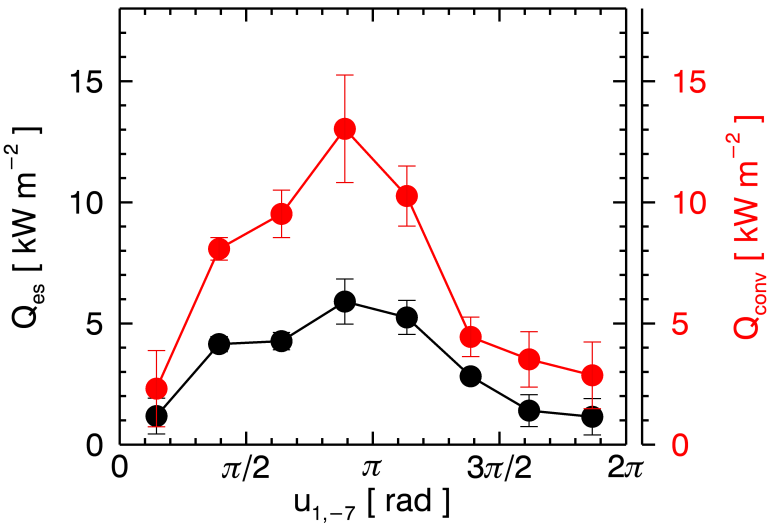

FIGURE 3.17: Profile of electrostatic energy flux as a function of the helical angle $u_{1,-7}$, for an ensemble of different shots all at $r/a \approx 0.97$. In red the contribution of the convective term.

The convective flux has been computerd according to the following expression:

$$Q_{conv} = \frac{5}{2}\Gamma_{es}T_e \tag{3.15}$$

From Figure 3.17 it is possible to conclude that $Q_{es} < Q_{conv}$ within the error bars: apparently, there is an inconsistency with what discussed in [29] where the electrostatic energy flux was fully ascribed to the convection associated to the electrostatic particle flux. The explanation resides on the fact that in the computation of the electrostatic energy flux we have intentionally neglected the term due to temperature fluctuations. This term reveals to be significative in the RFP case and can account for the missing portion in the estimation of the electrostatic energy flux. Eventually, according to [29], we can ascribe the whole energy flux due to electrostatic turbulence to the convective energy transport and find the conductive energy flux to be negligible.

We understood that transport driven by electrostatic fluctuations is deeply affected by the application of MPs; in particular, magnetic perturbations lead to peaked profiles of transport relevant quantities in the discharge phase when $\pi/2 \leq u_{1,-7} \leq 3\pi/2$. Since the peaks are in correspondence to the $m = 0$ island's O-point, it should be interesting to analyze the behavior of the electrostatic fluxes around the O-point and X-point of the applied perturbation in order to extract the typical transverse wave

numbers for these small scale fluctuations.

These analysis have been carried on a single representative discharge, the # 35755, and the profiles of Γ_{es} and Q_{es} can be observed in Figure 3.18: the collection of blue dots is an averaged profile around the O-point, while the red ones represent the distribution around the X-point of the perturbation.

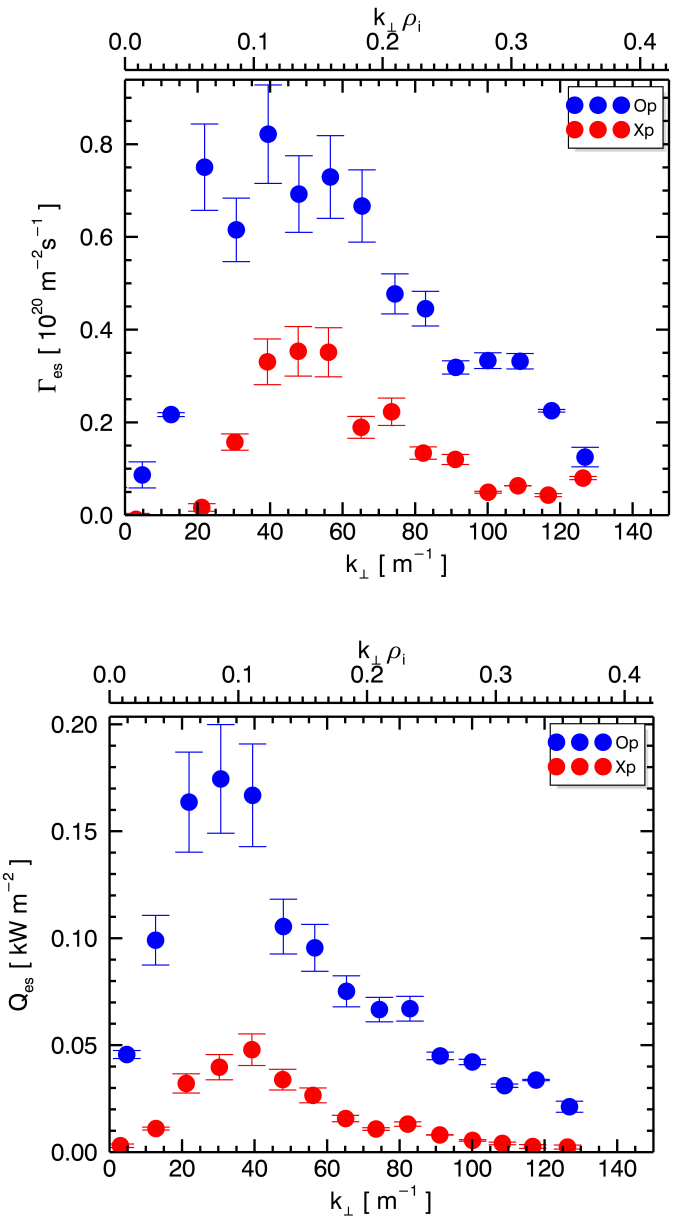

FIGURE 3.18: Profile of electrostatic particle flux (upper panel) and electrostatic energy flux (lower panel) for the discharge # 35755 as a function of the transverse wave number $k_\perp$. Plus, we draw a secondary x-axis where $k_\perp$ is multiplied by the Larmor radius ρ_i. The blue dots represent data around the O-point of the perturbation, while the red ones correspond to the X-point. For $k_\perp < 0$ there is no actual contribution to both fluxes.

Looking at the fluxes profiles, for both the O- and X-point distributions it can be seen a peak for $30\ m^{-1} \leq k_\perp \leq 60\ m^{-1}$ followed by a consequent reduction: the values of Γ_{es} and Q_{es} are definitely higher in the O-point collection than the ones obtained around the X-point region. This transport reduction will be further investigated in terms of amplitude of fluctuations and their relative phase.

In Figure 3.19 we show the profile of the transverse wave number as a function of frequency around the O-point and the X-point regions and from it we can extract the dispersion relation and evaluate the velocity with which the fluctuations propagate. Actually, no clear difference can be seen in the dispersion relation of collected data around the O-point with respect to the X-point.

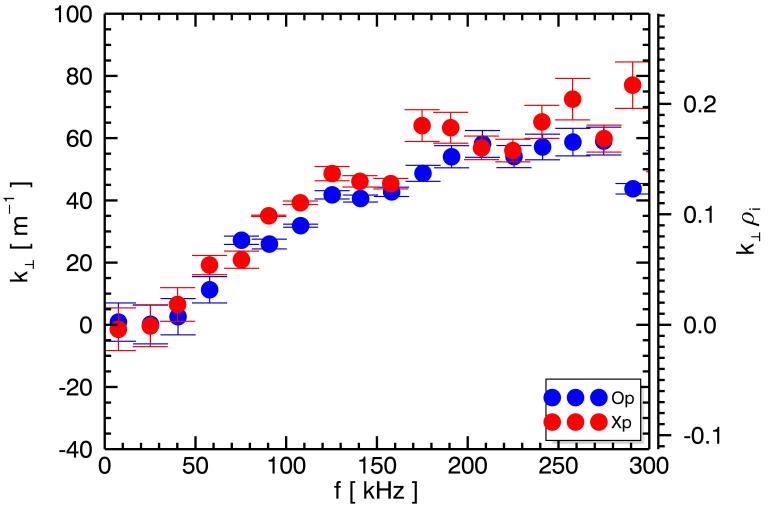

FIGURE 3.19: Perpendicular wave number $k_\perp$ versus the frequency relevant for particle transport for the discharge # 35755. A secondary y-axis is drawn, where $k_\perp$ is multiplied by the ion Larmor radius. The blue dots represent data around the O-point of the perturbation, while the red ones correspond to the X-point.

In order to better understand the profiles of the fluxes in Figure 3.18, hence their propagation around the O- and X-point, we computed both power spectra of density and potential fluctuations and their relative phase $\alpha_{n\phi}$[6] as a function of the transverse wave number $k_\perp$ and $k_\perp \rho_i$.

Profiles are shown in Figure 3.20 and in Figure 3.21: in the $k_\perp$ range where the fluxes tend to accumulate, for $30\ m^{-1} \leq k_\perp \leq 60\ m^{-1}$, we cannot see any clear difference in the phase relation between the O-point and the X-point contribution given by $\alpha_{n\phi}(k_\perp)$. Whereas, the power spectra confirm that the reason why the fluxes are lowered around

[6] See Equation 3.9.

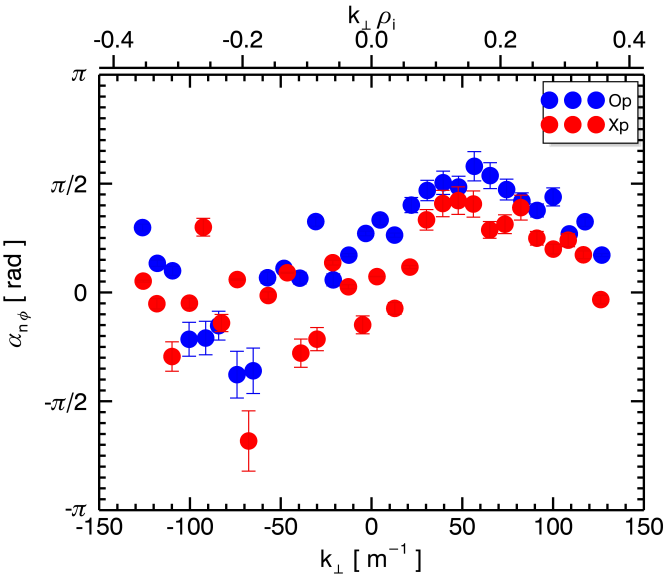

FIGURE 3.20: Relative phase between density and potential fluctuations. In the region where the electrostatic fluxes tend to accumulate, for $30\ m^{-1} \leq k_\perp \leq 60\ m^{-1}$, $\alpha_{n\phi}$ profile shows no difference in the O-point and the X-point distributions and it is peaked around $\alpha_{n\phi} \sim \pi/2$. For $k_\perp < 0$ there is no actual contribution to the electrostatic fluxes.

the X-point region is linked to a reduction in the fluctuations amplitude and not related to a reduction of the relative phase distribution around the X-point region.

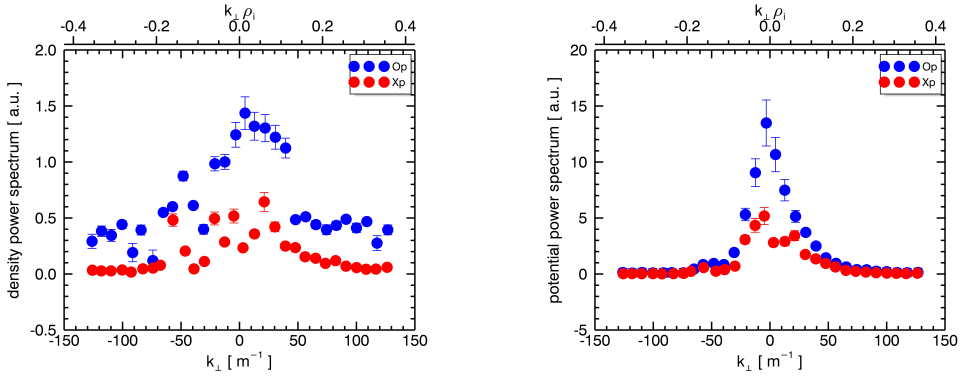

FIGURE 3.21: For the discharge #35755, we show the power spectra of electron density ($\bar{n}^2$) and floating potential ($\bar{V}_\phi^2$) fluctuations (see Equation 3.9) as a function of the transverse wave number $k_\perp$. Plus, for both plots we draw a secondary x-axis where $k_\perp$ is multiplied by the Larmor radius ρ_i. In both cases, the blue dots represent data around the O-point of the perturbation, while the red ones correspond to the X-point.

3.5 Tokamak: spectral analysis

We will now discuss the results obtained in the case of the tokamak configuration experiments in RFX-mod. All the analyses have been performed during the first part of the # 35555 discharge, where $q_a \simeq 2.1$.
We have performed analyses similar in all aspects to the ones already presented for the RFP configuration. Although we had not enough statistics to obtain radial profiles for the electrostatic fluxes, we have computed the particle and energy flux according to Equation 3.7 and Equation 3.8. Furthermore, we obtained their profiles as a function of frequency as showed in Figure 3.22.

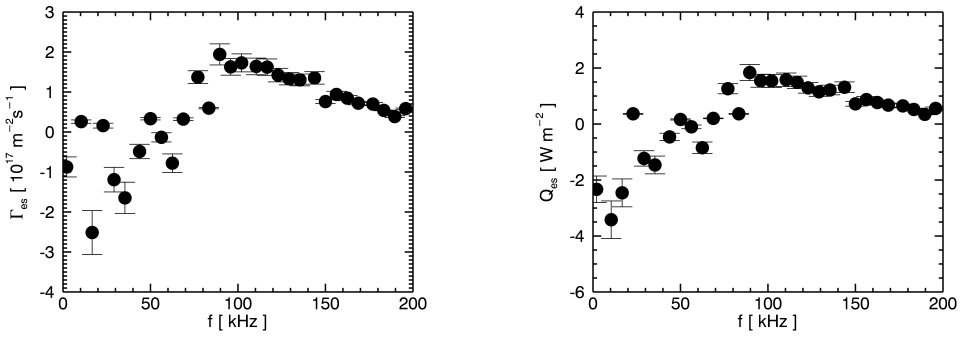

FIGURE 3.22: Profile of electrostatic particle flux (left) and profile of electrostatic energy flux (right) as a function of the frequency for discharge # 35555. For $f > 200\ kHz$ the contribution to both fluxes tends to zero.

Both particle and energy flux present a negative peak around $f \sim 20\ kHz$ and then show an *outward* contribution mainly concentrated in the range $80\ kHz \leq f \leq 120\ kHz$. We compared these results to analyses performed before the application of the external magnetic perturbation for $t < 0.2\ s$, where the fluxes show a lower *outward* contribution at $f \geq 80\ kHz$. We can deduce that transport increases also due to electrostatic fluctuations when a stochastic layer is applied and this confirms the main effects of RMPs application: RMPs modify and increase turbulent transport.

Considering the Fourier decomposition for both fluxes, we can extract a dispersion relation from the profile of the transverse wave number $k_\perp$ as a function of the associated frequency relevant for electrostatic transport ($f \leq 200\ kHz$). The scattered profile is shown in Figure 3.23. A secondary vertical axis is also drawn: the wave number is multiplied by the ion Larmor radius ρ_i, which for the considered discharge is of the order of $\rho_i \sim 1\ mm$.

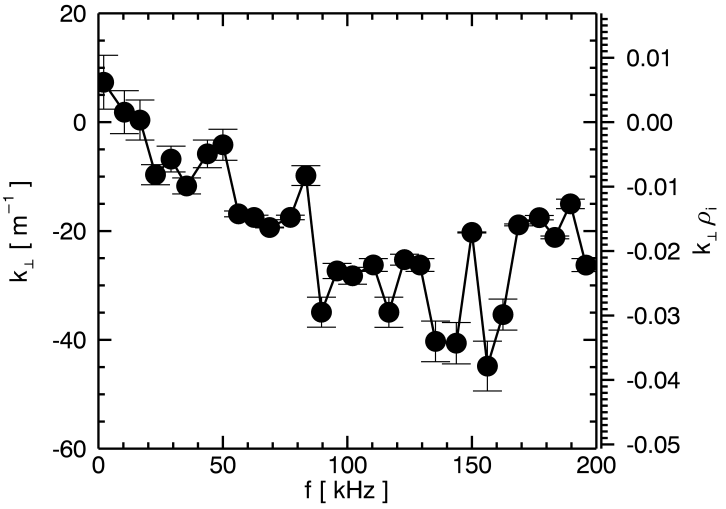

FIGURE 3.23: Perpendicular wave number $k_\perp$ versus the frequency relevant for particle transport. A secondary y-axis is drawn, where k is multiplied by the ion Larmor radius. Collected data refer all to discharge # 35555.

Then, the fluxes have been further analyzed as a function of the transverse wave number $k_\perp$. If we look at Figure 3.24 we can say that both energy and particle transport driven by electrostatic fluctuations are concentrated at negative values of $k_\perp$ in the range $-90\ m^{-1} \leq k_\perp \leq -30\ m^{-1}$ with a maximum peak around $k_\perp \sim -70\ m^{-1}$.
In Figure 3.24 we show also a secondary x-axis is plotted where k is multiplied by ρ_i: fluxes have peaks around $k_\perp \rho_i \sim -0.06$, while in RFP configuration electrostatic fluxes showed peaks around $k_\perp \rho_i \sim 0.1$. The presence of an *inward* contribution a $k_\perp > 0$ should be subject of further investigations.

From Figure 3.23 we can extrapolate a dispersion relation from which we can estimate a phase velocity for the fluctuations: $v_{phase} \sim 8\ km\ s^{-1}$.
Furthermore, we know that v_{phase} of the fluctuations (and therefore the related $k_\perp$) propagates in the same direction of the electron diamagnetic velocity term in analogy with the RFP case. Lacking a measurement for the density gradient, we cannot compare in this case the velocity associated to the electrostatic fluctuations with electron diamagnetic velocity; nevertheless, we can still compare the $\mathbf{E} \times \mathbf{B}$ term which for the tokamak case gives the velocity:

$$v_{\mathbf{E}\times\mathbf{B}} = \frac{\mathbf{E} \times \mathbf{B}}{B^2} = \frac{E_\theta}{B_\phi} \tag{3.16}$$

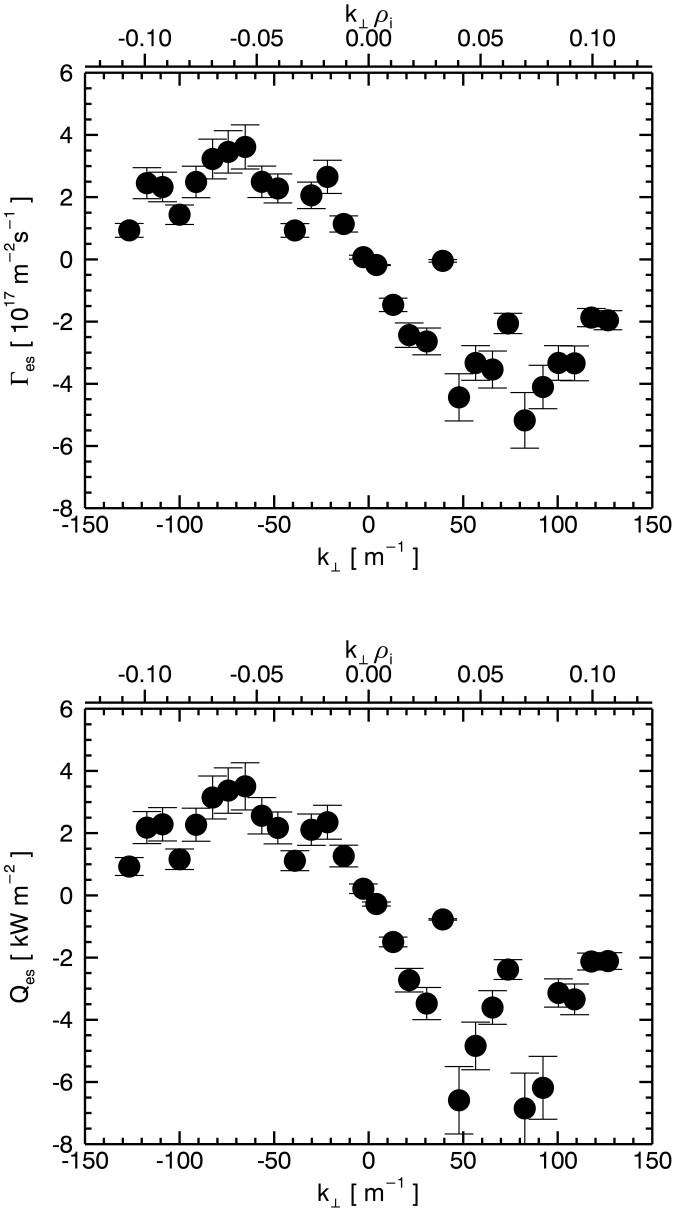

FIGURE 3.24: In the upper panel we report the profile of electrostatic particle flux while in the lower panel there is the profile of electrostatic energy flux as a function of the transverse wave number $k_\perp$. Plus, we draw a secondary x-axis where k is multiplied by the Larmor radius ρ_i.

The value obtained from local measurements gives us $v_{\mathbf{E}\times\mathbf{B}} \sim 8\ km\ s^{-1}$. Here the velocity field has been obtained considering the contribution coming from the floating potential, while neglecting the temperature term in the expression of the plasma potential that gives us the electric field.

Therefore, the fluctuations tend to propagate in the same direction of the electron diamagnetic flux with approximately a phase velocity of the order of the $\mathbf{E} \times \mathbf{B}$ one.

3.6 Tokamak case: transport in O-point and X-point regions

As we have already anticipated in Section 3.1, we have studied a tokamak discharge where an helical radial resonant MP rotating at the frequency of 10 Hz had been imposed during the first part of the discharge, with the same helicity of the spontaneous (2, 1) perturbation. RFX-mod tokamak operations at $q_a \approx 2.1$ are possible when involving an active MHD control system for the mitigation of the $(m = 2,\ n = 1)$ perturbation that spontaneously grows.
Assuming that the magnetic island is rigidly rotating with the applied MP, we can infer the poloidal maps of the various transport relevant quantities.

To this aim, it is important to find a reference frame consistent with the rotation of the perturbation. For the RFP case we would have used the helical angle, in this case the poloidal angle of the perturbation has been chosen, under the assumption of a rigid body rotation. Decomposing the magnetic perturbations in Equation 3.1 as cosine functions, the maximum of the applied perturbation can be found when:

$$cos(m\theta + n\phi - \delta b_r^{m,n}(t)) = 1 \quad \Longrightarrow \quad m\theta + n\phi - \delta b_r^{m,n}(t) = 0 \tag{3.17}$$

From it we can define the poloidal angle in the case of a $(m = 2,\ n = -1)$ perturbation and adopting the convention of negative n values indicating resonant perturbations:

$$\theta_{2,-1} = \frac{\phi + \delta b_r^{2,-1}(t)}{2} \tag{3.18}$$

In this way, it is possible to translate the temporal information contained in $\delta b_r^{m,n}(t)$ in the fixed reference frame of the U-probe, if substituting ϕ with the toroidal fixed angle at which the probe is located.

Let us now show the poloidal distributions obtained from the analysis done on the discharge $\#\ 35555$.
In analogy with the RFP case, we first show in Figure 3.25 the profiles of local electron temperature and density, as collected by the U-probe and afterwards re-sampled each 2 ms: we can notice a modulation on the density profile, following the symmetry of the dominant $(m = 2,\ n = 1)$ perturbation. If we recall Figure 3.4, we can say that time profiles of the radial component of the externally applied magnetic field and the

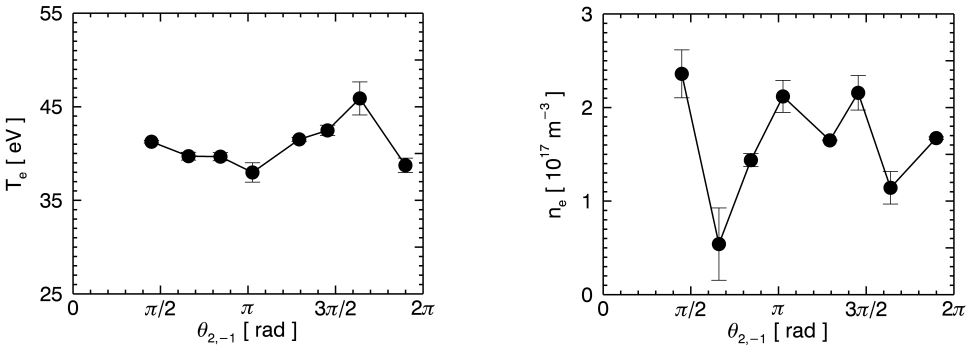

FIGURE 3.25: Electron temperature (left) and density (right) as a function of the poloidal angle of the perturbation $\theta_{2,-1}$ for the dicharge $\#35555$. The values associated to T_e seem to be too high to be reliable.

signal of the electron density, were already showing a visible modulation following the $m = 2$ symmetry.

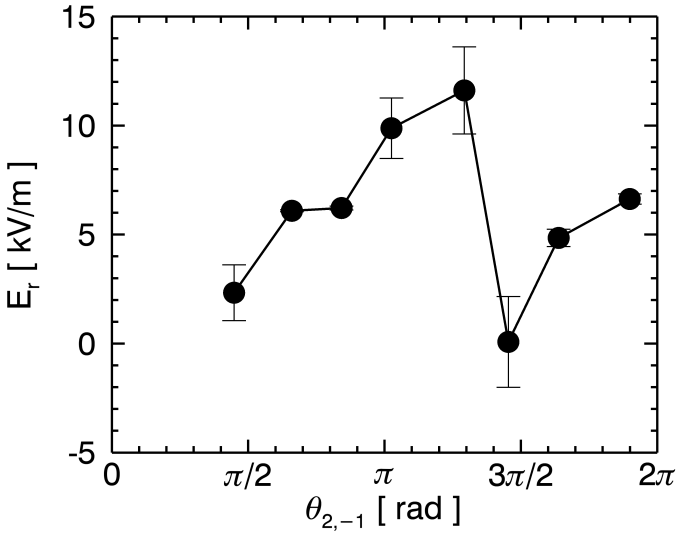

FIGURE 3.26: Radial component of the electric field as a function of the poloidal angle of the perturbation $\theta_{2,-1}$ for the dicharge $\#35555$.

Following the analogy with the RFP case, the poloidal profile of the radial electric field is shown in Figure 3.26. In this case E_r has been calculated neglecting the contribution of the temperature radial gradient since the measurements were considered not reliable. Hence, in first approximation:

$$E_r = -\frac{\partial}{\partial r}\phi_p \sim -\frac{\partial}{\partial r}\phi_f \tag{3.19}$$

where ϕ_f is the floating potential.

The radial component of the electric field follows a clear $m = 2$ symmetry, with depletions around $\theta_{2,-1} \simeq \pi/2$ and $\theta_{2,-1} \simeq 3\pi/2$, and an enhancement in the profile for $\theta_{2,-1} \simeq \pi$. A plausible interpretation of the E_r profile can only be given in relation to the underlying magnetic topology that we are introducing in the next subsection.

3.6.1 Transport driven by electrostatic fluctuations

In Figure 3.27 we present the Poincaré plot for the discharge #35555 in the plane $(r,\ \theta_{2,-1})$. The map is again obtained through the field line tracing code FLiT, built retaining the poloidal mode numbers $m = 0, 2$ with the toroidal periodicity $n = 1$ only.

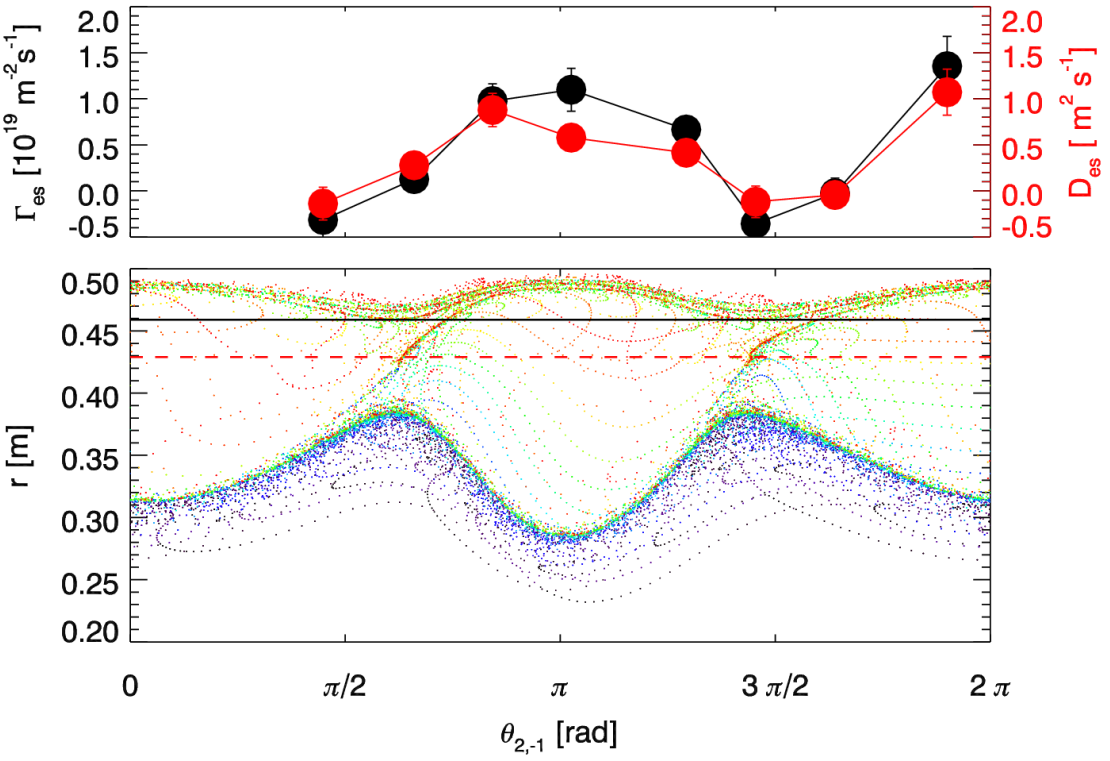

FIGURE 3.27: Poincaré plot in the plane $(r,\ \theta_{2,-1})$ for the dicharge # 35555 at $t = 0.3\ s$, instant chosen in correspondence of a maximum of the externally applied perturbation $(m = 2,\ n = -1)$. The color code is arbitrarily chosen depending upon the starting values of the radial coordinate of the magnetic field lines. The red dashed line indicates the radial probe insertion while the black line defines the location of the first wall. Above the Poincaré plot, the profiles of particle flux (black) and perpendicular diffusion coefficient (red) are drawn as a function of the poloidal angle.

The reconstruction of the ($m = 1$, $n = 1$) is not possible since it represents a resonant kink mode located at the plasma core, whose effects cannot be traced by the external magnetic coils used as boundary conditions by the FLiT code.
U-probe local measurements are referred to the radial position indicated by the red dashed line: the probe was inserted 3 cm inside the chamber, rotated according to the cross-field plane in the tokamak configuration. It is worth noting that these are measurements that, according to the magnetic reconstruction, lie inside the magnetic island itself.

Since we have introduced the topological environment, we can now give a possible explanation for the E_r profile in Figure 3.26: the presence of the island touching directly the material wall, as can be seen in Figure 3.27, creates a wide scrape-off layer region (SOL), with the internal separatrix of (2, 1) mode representing the separatrix between confined plasma and SOL. The positive radial electric field is consistent with an higher electron mobility (generally observed in the far SOL, see for example [72]). On the other side at the X-point the separatrix position is moving towards the wall and the reduction of E_r may be interpreted as a reduction of the difference in electron-ion mobilities. It is equivalent to provide a measurement of the electric field in a region closer to the separatrix, where also in standard discharges E_r approaches the zero value and than changes sign (e.g. [72]). This is consistent with measurements performed in the japanese LHD device [73], where the change of sign of the electric field is suggested to provide a valid measurement of the effective plasma boundary in presence of a 3D magnetic field.

Together with the radial electric field, also the electrostatic particle flux and the diffusion coefficient (obtained through Equation 3.7 and Equation 3.13) follow a $m = 2$ modulation (see the upper panel Figure 3.27). In Figure 3.28 we show also the electrostatic energy flux plus the convective contribution: both of them show a $m = 2$ symmetry. The depletions around $\theta_{2,-1} \simeq \pi/2$, $\theta_{2,-1} \simeq 3\pi/2$ and the enhancement at $\theta_{2,-1} \simeq \pi$ are in correspondence of the poloidal locations of the two X-points and the O-point of the ($m = 2$, $n = 1$) island, visible in the Poincaré map in Figure 3.27.
Since in tokamak configuration the temperature fluctuations are smaller with respect to the RFP case, we find $Q_{es} \sim Q_{conv}$ and the conductive energy flux due to electrostatic turbulence is negligible.

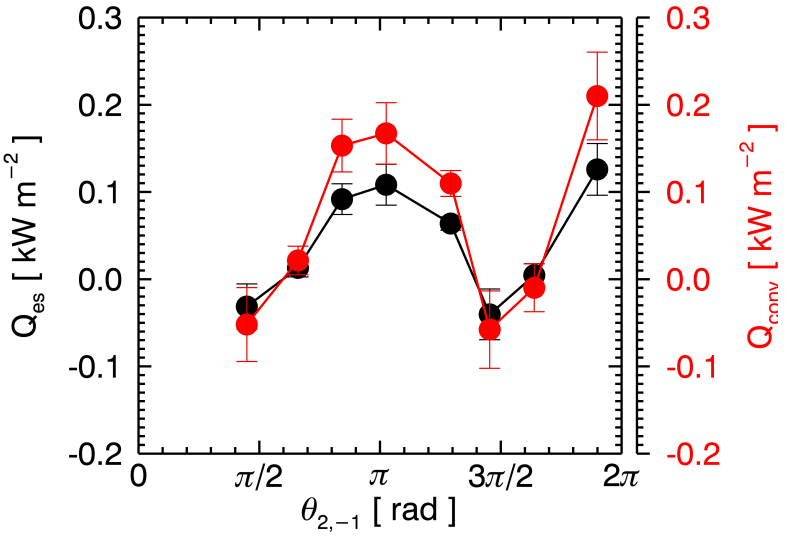

FIGURE 3.28: Profile of electrostatic energy flux as a function of the poloidal angle $\theta_{2,-1}$, for the discharge # 35555. In red the contribution of the convective flux.

We understood that also in the tokamak case, transport driven by electrostatic fluctuations is deeply affected by the application of MPs; in particular, the applied (2, 1) magnetic perturbation leads to an increase in the fluctuation level in the discharge phase when $\theta_{2,-1} \sim \pi$.

In order to have a comparison with the RFP case, we can analyze the behavior of the electrostatic fluxes around the O-point and X-points of the applied perturbation in order to extract the typical transverse wave numbers that influence small scale electrostatic fluctuations. The profiles of Γ_{es} and Q_{es} can be observed in Figure 3.29: the collection of blue dots is again an averaged profile around the O-point, while the red ones represent the distribution around the two X-points of the perturbation.

In this case the phase relation between $k_\perp$ and the fluxes leads to have positive fluxes for negative values of the transverse wave number, in particular a consistent accumulation of points can be seen for $-100\ m^{-1} \leq k_\perp \leq -20\ m^{-1}$ and a consequent quench in the profiles of both fluxes around the O-point of the perturbation, in contrast with the behavior in the X-point region. Indeed, the X-point distribution determines an *inward* contribution which should be the subject of further investigations.

Still, in the O-point case the values of Γ_{es} and Q_{es} are definitely higher than in the case of the X-point distribution.

In Figure 3.30 we can then investigate the relation between $k_\perp$ and the associated frequency around the O- and the X-point regions.

We can determine that the velocity of the fluctuations changes its direction at $f \geq$

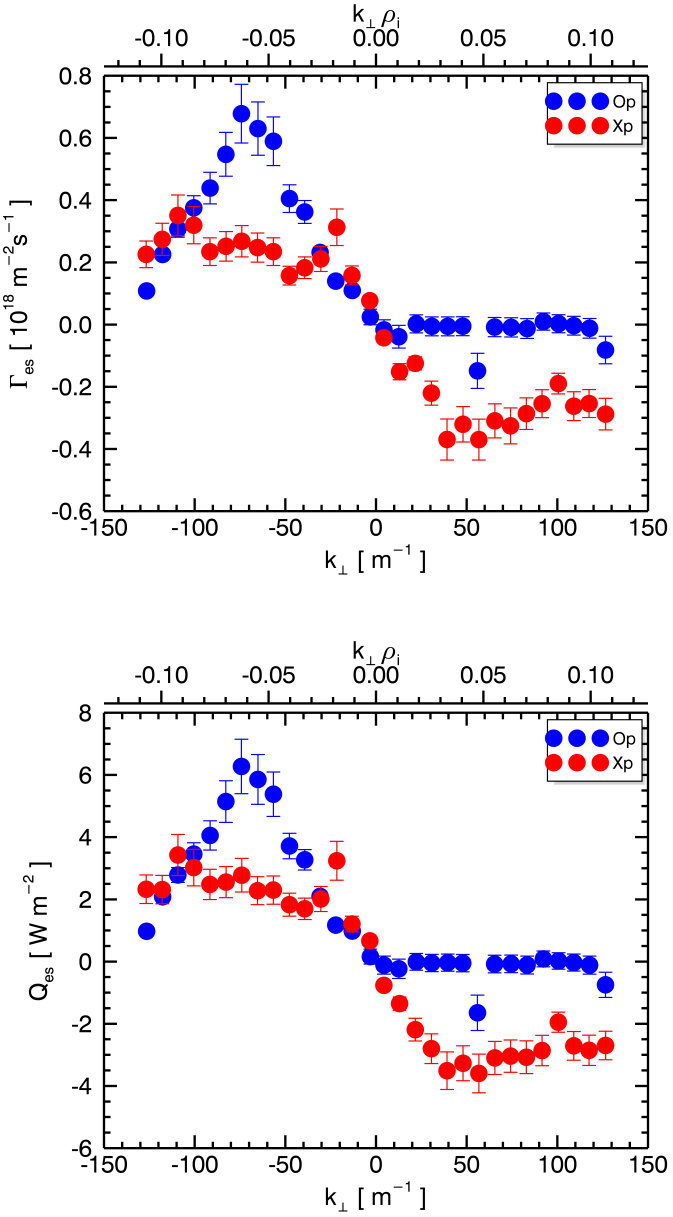

FIGURE 3.29: For the discharge # 35555, in the upper panel it is shown the profile of electrostatic particle flux and in the lower panel, the profile of electrostatic energy flux as a function of the transverse wave number $k_\perp$. Plus, for both plots we draw a secondary x-axis where $k_\perp$ is multiplied by the Larmor radius ρ_i. In both cases, the blue dots represent data around the O-point of the perturbation, while the red ones correspond to the two X-points. For $k_\perp > 0$ we can see no contribution to both fluxes around the O-point region, while they show an inward contribution around the X-point.

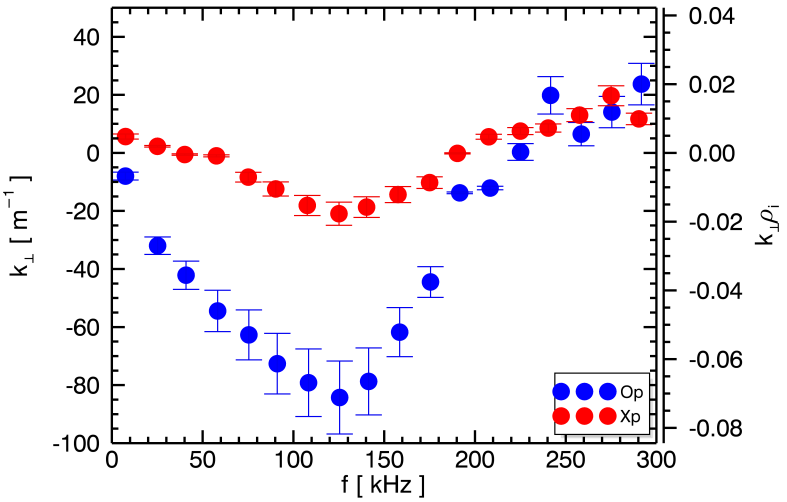

FIGURE 3.30: Perpendicular wave number $k_\perp$ versus the frequency relevant for particle transport for the tokamak discharge # 35555. A secondary y-axis is drawn, where $k_\perp$ is multiplied by the ion Larmor radius. The blue dots represent data around the O-point of the perturbation, while the red ones correspond to the X-point.

$120\ kHz$ both in the O- and X-point distribution. This suggests that for frequencies greater than 120 kHz, v_{phase} tends to align itself to the direction of ion diamagnetic velocity instead of the electron one.

We have also computed both power spectra of density and potential fluctuations and their relative phase $\alpha_{n\phi}$ as a function of the transverse wave number $k_\perp$ and $k_\perp\rho_i$. Profiles are shown in Figure 3.31 and in Figure 3.32. In the $k_\perp$ range where the fluxes tend to accumulate, for $-100\ m^{-1} \leq k_\perp \leq -20\ m^{-1}$, we can state that there is no clear difference in the phase relation between the O-point and the X-point contribution given by $\alpha_{n\phi}(k_\perp)$. In the power spectra we can observe a reduction in the density fluctuations around the X-point region in contrast to a slight enhancement in the O-point distribution. Once again the fluxes profiles depend on the increase or reduction in the fluctuations level. The region with $k_\perp > 0$ where the profiles show an *inward* contribution will be subject of further investigations.

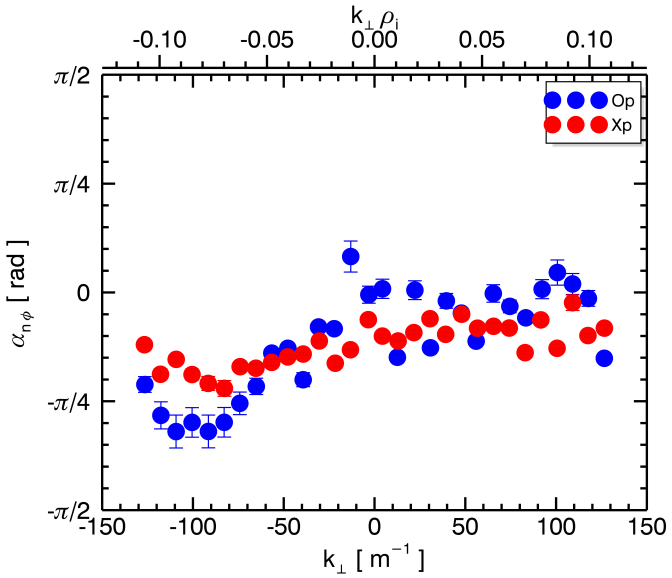

FIGURE 3.31: Relative phase between density and potential fluctuations. In the region where the positive contribution to the electrostatic fluxes tend to accumulate, for $-100\ m^{-1} \leq k_\perp \leq -20\ m^{-1}$, $\alpha_{n\phi}$ profile shows no difference in the O-point and the X-point distributions and it is concentrated around $\alpha_{n\phi} \lesssim \pi/4$.

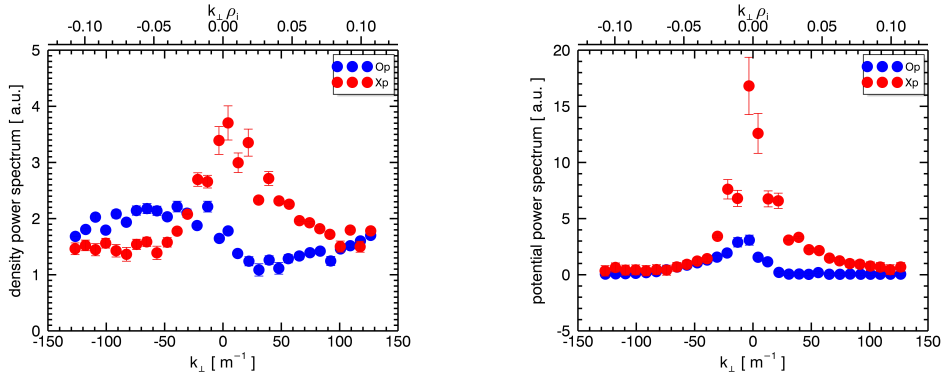

FIGURE 3.32: For the discharge #35555, we show the power spectra of electron density ($\bar{n}^2$) and floating potential ($\bar{V}_\phi^2$) fluctuations (see Equation 3.9) as a function of the transverse wave number $k_\perp$. Plus, for both plots we draw a secondary x-axis where $k_\perp$ is multiplied by the Larmor radius ρ_i. In both cases, the blue dots represent data around the O-point of the perturbation, while the red ones correspond to the X-point.

Part III

Topology analysis

Chapter 4

Reconnection and edge topology

In Chapter 3 we have described how magnetic topology affects transport properties at the edge region both in RFP and in tokamak configuration; in this chapter instead, we would like to give an example of how topology is influenced by spontaneous events as magnetic reconnections in a RFP device.
In this chapter we are going to show the results obtained from modeling the RFP edge under certain assumptions in presence of magnetic reconnections. First, we will briefly introduce the main adopted reconnection models, then we will give a description of the typical self-organization phenomena in RFP devices and in particular, in RFX-mod. Eventually, we will show and discuss the analysis performed and the tools used to perform them.

A reconnection event is a fundamental dynamical process that takes place in high conductive plasmas, both astrophysical and laboratory ones, and substantially consists in a topological rearrangement of the magnetic field lines. During this process, magnetic energy is converted into kinetic energy through acceleration or heating of charged particles and as a consequence the system is driven to relax into a new equilibrium configuration at lower magnetic energy.
Magnetic reconnection is seen in the evolution of solar flares, coronal mass ejection and interaction of solar winds with the Earth's magnetosphere and is considered to occur in the formation of stars[1]. It occurs as the self-organization process in current carrying fusion plasmas, it is observed in relaxation processes in reversed-field pinches and in minor and major disruptions of tokamak discharges.

[1] A good review on magnetic reconnection in astrphysical and laboratory plasmas can be found in [74].

4.1 Models for magnetic reconnection events

Reconnection phenomena may depend not only on local plasma parameters in the reconnection layer but also on 3D global boundary conditions. This is the reason why providing realistic models of magnetic reconnection is an interesting theoretical challenge.

The simplest approach is to reduce the problem to a two-dimensional *slab* geometry, assuming that the reconnection event takes place in a plane. Figure 4.1 gives a scheme for the dynamic process of a 2D reconnection event. The reconnection takes place

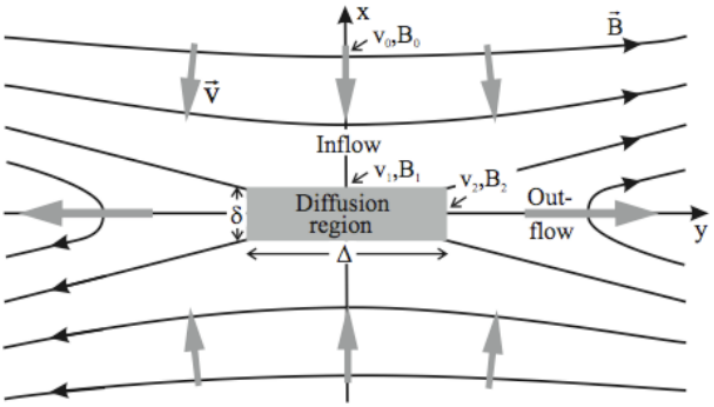

FIGURE 4.1: Schematic pattern for a two-dimensional reconnection. This figure is taken from [75].

where the plasma resistivity is finite, namely in the *diffusion region*. As long as the magnetic lines approach to each other, the magnetic field configuration changes rapidly till vanishing in the middle. This phase, preceding the magnetic reconnection itself, can be described by means of the combined Faraday equation (Equation A.6) and Ohm's law (Equation A.4), considering a uniform resistivity η:

$$\frac{\partial \mathbf{B}}{\partial t} = \nabla \times (\mathbf{v} \times \mathbf{B}) + \frac{\eta}{\mu_0} \nabla^2 \mathbf{B} \tag{4.1}$$

As the field lines approach the origin the quantity $\nabla^2 \mathbf{B}$ becomes larger, due to the changes in the field geometry; furthermore, since this quantity multiplies η, the resistivity term becomes more and more important.

The inflow of magnetic field lines is an essential actor in plasma relaxation process since it allows an efficient conversion of magnetic energy into kinetic one. In addition, the induction equation written above points out that magnetic field gradients become stronger wherever reconnection takes place, since larger field gradients are connected

to high current densities. This is where the *current sheets* develop: it is believed that they are the precursors in the reconnection dynamics [75], triggered by the electric field and a consequent enhancement of current density. Eventually, magnetic field lines can decouple and reconnect where the local Lundquist number, given by Equation A.10, is found to be lower than elsewhere: when reconnection occurs, the magnetic topology changes, resulting in the plasma being squeezed out sideways as in Figure 4.1.

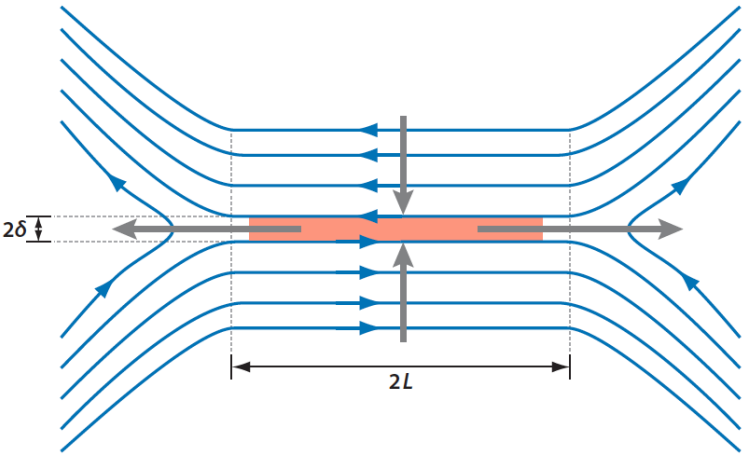

FIGURE 4.2: Magnetic field geometry in Sweet-Parker reconnection. Oppositely directed magnetic fields are brought together over a length $2L$ and reconnect in a diffusion layer of width 2δ. This figure is taken from [76].

If we make assumptions on the width of the diffusion region to be of the order of the global length scale L and on an homogeneous external region, then we are introducing the *Sweet-Parker model* [77]. Parker (1957) and Sweet (1958) were the first to formulate magnetic reconnection as a local problem in which the inflow of plasma was connected with an outflow from the diffusion region. Although this model is not able to account for the fast rates measured in systems with high Lundquist number ($S > 10^{10}$), on the other hand it agrees quite well with many RFP experiments [78, 79, 80] ($10^2 < S < 10^8$).

Sweet-Parker reconnection is slow because all the fluid brought into the reconnection region must flow out through a thin, resistive channel. Petschek (1964) realized that reconnection would be faster if the resistive layer were short and most of the incoming fluid did not pass through it, but instead was redirected by standing shock waves. In Petschek's model a shorter length scale L' substitutes L and the reconnection rate is increased by $\sqrt{L/L'}$, so the reconnection process is actually sped up.

A general feature of Petschek-like models is that, in contrast to the Sweet-Parker model, most of the energy is converted to the ion kinetic energy of the outflow and, if shocks are present, to heat, with relatively little energy going into resistive heating

of the electrons.
Both these models describe a steady-state reconnection but do not address the self-organization circumstances under which it occurs.

4.2 RFP self-organization

In a RFP discharge, magnetic reconnection occurs during self-organization processes that can be of both continuous and impulsive nature. However it is associated to situations where the magnetic field suddenly reconnects into a new MHD equilibrium state releasing the magnetic energy stored until that in a force-free magnetic equilibrium configuration, reached via a slow adjustment to an external driving force. Local reconnections can exist on different surfaces, defined by the safety factor $q = m/n$, that eventually lead to a global relaxation whose macroscopic effect is always the dissipation of total magnetic energy in favor of its conversion to the kinetic one.
But what mechanism is at the basis of the self-sustainment of a RFP configuration? Let us discuss the dynamo mechanism in details in the next paragraph.

4.2.1 The dynamo mechanism

The dynamo process underlies the configuration of reversed-field pinches and represents the main actor in the plasma self-organization mechanism: it can be discussed in analogy with the wire model presented in Section 2.2.
In laboratory plasmas, resistive diffusion evolves the plasma away from a preferred state whereas the dynamo forces the plasma back toward the preferred, self-organized state. While resistive diffusion is a well-understood process, the plasma self-organization by means of dynamo is a current topic of research.
Nevertheless, it has been revealed by non-linear visco-resistive MHD simulations that the dynamo process is strongly related to the phenomenon of magnetic relaxation of the RFP configuration, where stationary, pure *single helicity* states are found [81].
However, let us try to better explain the dynamo process through its premises: in a RFP core the poloidal and toroidal magnetic fields have the same order of magnitude (see for example Figure 1.7) and consequently the current flowing in the plasma is much higher than in a tokamak. Another crucial aspect is represented by the values of the safety factor, $q < 1$ over the whole cross section of the plasma. In this way a

resistive kink is likely to develop (in analogy with the wire model) and the magnetic field can be helically distorted. This distortion requires a modulation of the current density along the current lines and the modulation in turn requires the existence of a modulated electric field, which has to be an electrostatic one. The corresponding electrostatic potential brings a component of the electric field perpendicular to the magnetic field and this component drives an $\mathbf{E} \times \mathbf{B}$ motion whose non axi-symmetric part is exactly the dynamo velocity field : $\mathbf{E}_{dynamo} = \mathbf{v} \times \tilde{\mathbf{b}}$, where $\tilde{\mathbf{b}}$ is the perturbed magnetic field.

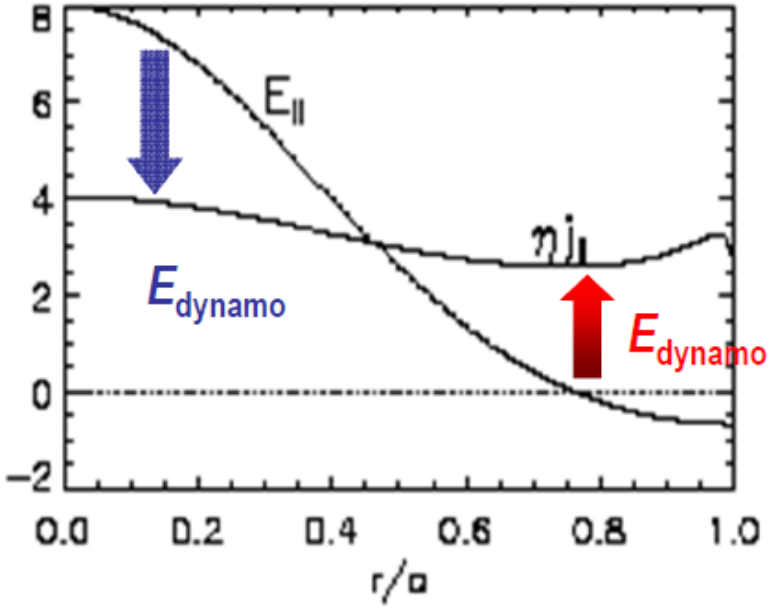

FIGURE 4.3: Radial profile of $E_{\parallel}$ and $\eta j_{\parallel}$ in a RFP configuration. The discrepancy is accounted for the dynamo term E_{dynamo} that acts in opposite directions in the core and at the edge.

Therefore, in an experimental RFP system, the existence of a finite plasma resistivity is responsible for the dynamo term and can consequently cause the rise of MHD tearing instabilities[2].

If we now want to extract the typical resistive time-scale, we should consider that the magnetic field evolves in time accordingly to the induction equation in Equation 4.1. Neglecting the convective term in Equation 4.1, and introducing L as the characteristic length of the spatial variation of $\mathbf{B}$, we obtain a differential equation for the time evolution of the magnetic field, whose solution is:

$$\mathbf{B}(t) = \mathbf{B}_0 \, e^{-t/\tau_R} \tag{4.2}$$

[2]See Appendix A.

where $\mathbf{B}_0$ is the initial condition for the field and

$$\tau_R = \frac{\mu_0 L^2}{\eta} \tag{4.3}$$

is the *resistive diffusion time*. τ_R indicates the time scale on which the magnetic energy is dissipated and the RFP configuration is eventually lost, in the absence of any other regeneration mechanism. The poloidal component of the magnetic field is controlled by external means, since it depends on the toroidal current induced by the transformer, while a large part of B_ϕ depends on the plasma itself and attempts to control its shape by external means have succeeded only in a transient way [82].

It is a general observation in RFP experiments that the configuration lasts as long as the plasma current is sustained, usually much longer than the resistive diffusion time: it is possible to evince that also the experimental evidence implies the existence of an internal and spontaneous mechanism of regeneration of dissipated toroidal magnetic flux, represented by the *dynamo effect*.

The electric field $\mathbf{E}_{dynamo}$ sums up in Ohm's law (A.4) to the externally applied electric field and contributes to drive a current density **j**. Its poloidal component is then responsible for the regeneration of the toroidal magnetic field in the core and the sustainment of its reversal at the edge.

Explicitly analyzing Ohm's law in its parallel component: $E_\parallel = \eta j_\parallel$ and the induced parallel component of the electric field $\frac{\mathbf{E}\cdot\mathbf{B}}{B} = \frac{E_\phi B_\phi}{B}$ is proportional to the toroidal magnetic field, which reverses sign at the edge. $\eta j_\parallel$ instead, never changes its sign across the radius so the existence of an additive E_{dynamo} term is necessary.

4.2.2 Discrete vs continuous dynamo

As we have already anticipated, in a laboratory plasma the relaxation phenomenon can occur in either a continuous or cyclic way. If the plasma resistivity is finite, tearing instabilities are triggered whenever the magnetic configuration has an excess of free energy. The dynamo term sustains the reversed field, while the resistive diffusion would tend to unavoidably loose the configuration.

In some experimental plasmas, the net result is that these effects are nearly balanced at all times; thus, the plasma mean field remains approximately steady. In other experimental plasmas, the two effects are separated in time [16]. During the drive period, the plasma slowly evolves away from a diffusive state, led by the applied loop voltage. Then, due to the dynamo effect, the plasma rapidly crosses metastable

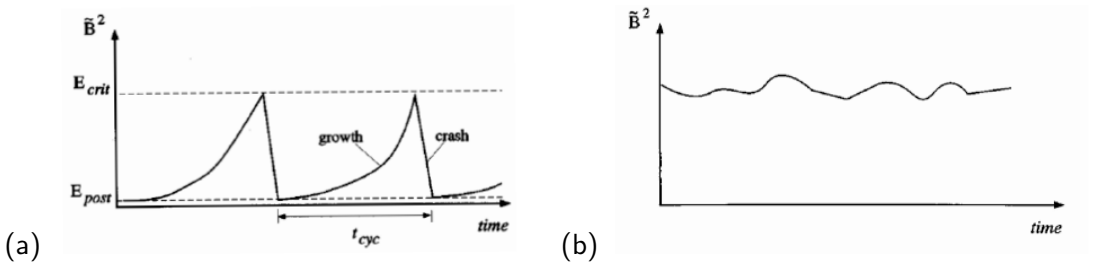

FIGURE 4.4: Evolution of fluctuation energy *(a)* in the discrete dynamo and *(b)* in the continuous dynamo. This figure is taken from [83].

configurations and eventually returns to a diffusive state. If the effects of this relaxation process are characterized by cyclical growth and crash phases then the dynamo is termed *discrete* and it is believed that to occur whenever there are a few unstable tearing modes. On the other hand a steady-state saturated turbulence that destabilizes several dynamo modes corresponds to a *continuous* dynamo. These two limits are shown in Figure 4.4, where the temporal evolution of the fluctuating magnetic energy is sketched.

4.3 Spontaneous reconnection in RFP configuration

In RFP plasmas, the role of local reconnection in the global relaxation phenomena has been experimentally studied. In Madison Symmetric Torus, a RFP device located in the United States, simultaneous reconnections are observed at different radii corresponding to different n with the same poloidal number, $m = 1$ [78].

Generally, when the current density profile becomes highly peaked, tearing modes develop reconnecting magnetic field lines and the plasma itself rapidly reorganizes, with an abrupt conversion of poloidal magnetic flux to toroidal flux that implies a lowering of the total magnetic energy (see Figure 4.5). Another implication is that the ion temperature increases significantly at the expenses of magnetic energy with the development of a non-Maxwellian tail in the ion temperature distribution.

During a reconnection event in MST, a sheared rotation of the plasma has also been observed to suddenly change during relaxation events. Though for all RFP plasmas, it has been found that the space and time varying fluctuations associated with the reconnection produce a large-scale Lorentz force that alters the plasma rotation.

In all RFP devices, the reversal parameter F is characterized by periodic crashes that drive the plasma away from the equilibrium state (Taylor state). In Figure 4.6 we

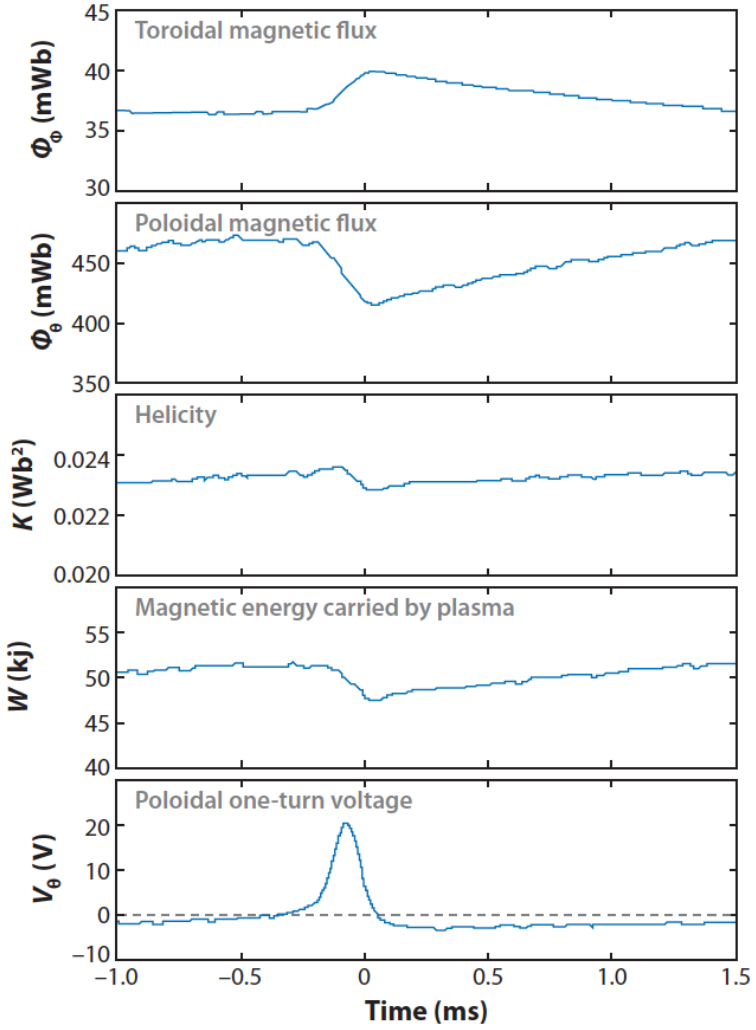

FIGURE 4.5: A discrete magnetic reconnection event in Madison Symmetric Torus. In figure is shown the time evolution of toroidal magnetic flux, poloidal magnetic flux, helicity, magnetic energy carried by plasma, and poloidal one-turn voltage [84].

report an example for an arbitrary chosen discharge on RFX-mod. If the RFP did not have the dynamo mechanism, then the F time trace would be almost steady as it partially is during the rise time of the discharge but the jagged time trace is assumed as the signature of discrete relaxation events (DREs). The *rise time* and the *crash time* last respectively a tenth of milliseconds and a few ones.

The dynamo is evident also in the flux time traces in RFX-mod, analogously to the MST case in Figure 4.5. As long as the plasma stays in the relaxed state (the F parameter is constant), the toroidal flux diminishes while the poloidal one follows an opposite trend; that is because only the toroidal plasma current is efficiently driven externally, while the poloidal component is internally generated by the plasma. The field conversion occurs at each crash by means of magnetic reconnection, the poloidal

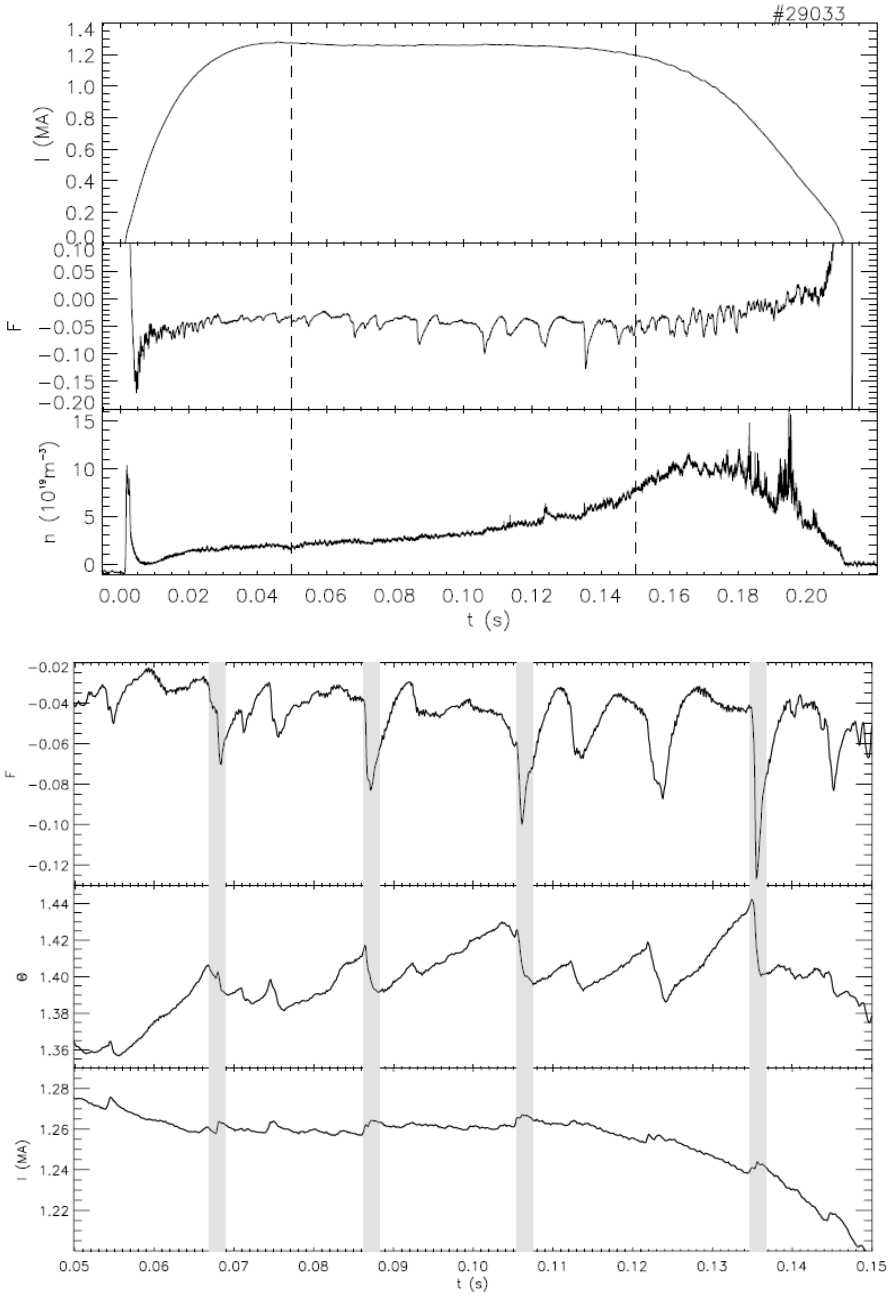

FIGURE 4.6: (shot 29033) (up) plasma current, reversal parameter and density evolution, (down) enlargement of the reversal and the pinch parameter and the plasma current for the time interval enclosed by dashed lines in the plot above [85].

flux grows till a threshold value, then the plasma triggers the relaxation that in turn generates the toroidal flux.

Therefore, the reversal parameter F can be used as a probe to locate the beginning and the end of the crash events: it quantifies the steepening of the toroidal field profile, the deeper F is, the greater is the paramagnetic field generated by the plasma to sustain the RFP magnetic configuration.

4.3.1 Current sheets during spontaneous reconnections

The spontaneous discrete, almost cyclic, rearrangements of the magnetic topology (relaxations) to new MHD equilibria, through reconnection of magnetic field lines are indeed manifestations of self-organization processes inside a RFP device.
It is common to observe the development of field aligned current structures [86] apart from the possibility to characterize two types of sudden relaxation events [87]: one related to large reconnection, where the main initial role is played by $m = 1$ unstable dynamo modes that non-linearly drive the growth of $m = 0$ modes and the second one, corresponding to small reconnection events, where the $m = 0$ are linearly unstable.
In RFX-mod, recent studies [88, 89] have shown that reconnection events lead to the formation of a toroidally localized $m = 0$ perturbation [90] which moves toroidally with the plasma in the opposite direction with respect to the toroidal current (towards decreasing toroidal angles) and strongly perturbs edge plasma profiles. It has been found that this toroidal localized perturbation corresponds to a spontaneous generation of a poloidal *current sheet*. In particular, in order to describe current sheets in terms of magnetic fluctuations, the use of a diagnostic able to collect high frequency data is required. In RFX-mod, to this aim, it was exploited a large set of electrostatic and magnetic probes located inside the vacuum vessel, which constitute the Integrated System of Internal Sensors (ISIS) diagnostic [91]. ISIS pick-up coils measure the time derivative of the toroidal component of the magnetic field with a sampling frequency of 2 MHz. If we analyze a large database of high current experiments both in MH and QSH regime, we can observe an increased activity of the internally resonant $m = 1$ dynamo modes, with an energy cascade from $n = -7$ towards higher $|n|$ modes[3], cfr. Figure 4.7.
This energy cascade in the Fourier space corresponds to a toroidally localized magnetic perturbation becoming narrower. The localized perturbation is due to the non-linear coupling of the $m = 1$ modes, which have a natural tendency to lock in phase and form the *locked mode* at a fixed toroidal position, ϕ_{lock}. A further deformation induced by the consequent locking in phase of $m = 0$ modes tends to increase plasma wall interaction at ϕ_{lock} and enhance particle transport [92].
The common feature of all these experiments is the growth of the $m = 1$ modes, rapidly followed by an abrupt decrease (*crash*) in their amplitude, with a large part of magnetic energy transferred to an $m = 0$ perturbation.

[3] Negative n values correspond to perturbations resonating internally with respect to the reversal surface.

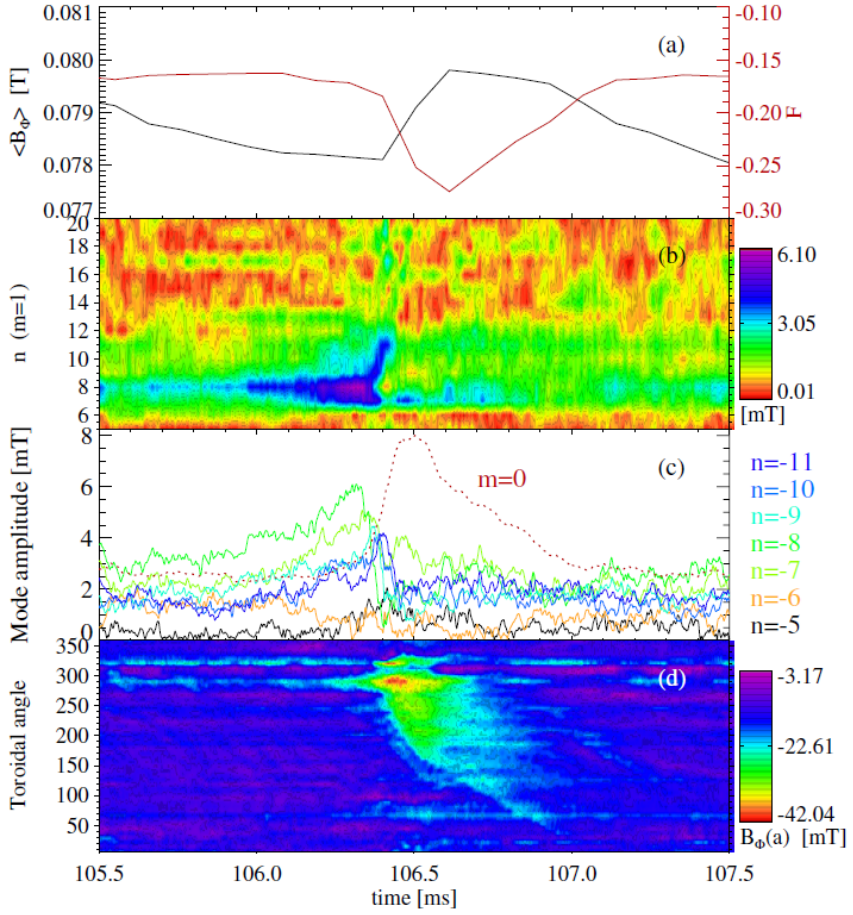

FIGURE 4.7: Time evolution of a single relaxation event: (a) average toroidal magnetic field and reversal parameter F; (b) contour plot of the amplitude of the internally resonant $m = 1$ dynamo modes; (c) amplitude of single $m/n = 1/n$ modes and total energy of $m = 0$ modes; (d) contour plot of $m = 0$ components of magnetic toroidal signals on a toroidal array. Figure is taken from [89].

4.4 Topological analysis

The interest in studying the modifications to the magnetic topology induced by the afore-described relaxation events driven by magnetic reconnections and related to the formation of toroidally localized perturbations has led to the topological analysis performed on the discharge # 99999 of RFX-mod.

In our analyses we start from an ensemble of discharges performed at high plasma current ($I_p \sim 1.5\ MA$), both in MH and QSH regime, that show the typical crashes in the reversal parameter as in Figure 4.6. The aim is to isolate the effect of the dynamics common to all these discharges and, if possible, to try to evince the surface on which the reconnection happens and hence generates the field-aligned current structures, as reported in [89].

In order to fulfill these intentions, it has been performed an average over the signals coming from the external pick-up coils, although we know that external magnetic measurements are shielded by the vacuum vessel and are not able to fully account for the fast dynamics of magnetic reconnections[4]. Nevertheless, these magnetic probes provide information on the toroidal and radial component of magnetic field and are currently used as boundary conditions for the reconstruction of Newcomb's eigenmodes in FLiT[5]. The FLiT code has been fully exploited in the analysis of # 99999 in order to obtain a temporal evolution of the magnetic topology changes around the crash event.

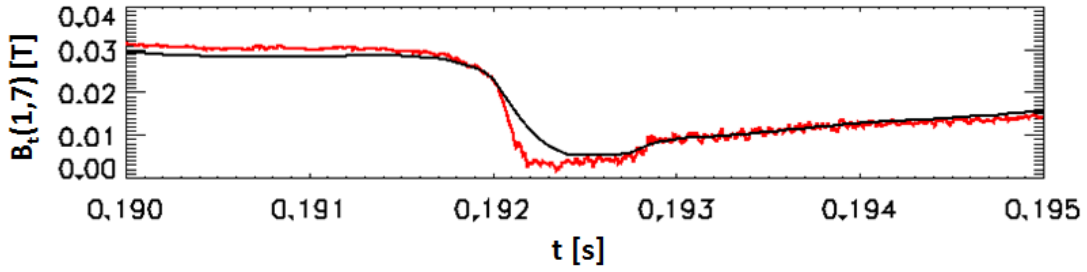

FIGURE 4.8: Amplitude of the dominant mode ($m = 1$, $n = 7$) for a representative discharge. In red the signal coming from ISIS diagnostic while in black the one coming from external measurements. The black line is smoother then the red one, indicating that the fast dynamics is not "seen" by the external pick-up coils.

According to [89], we know that magnetic reconnection events are characterized by high frequency magnetic perturbations that would be better accounted for through the ISIS diagnostic. Unfortunately, at the time of this analysis we lacked the possibility of including the signals coming from ISIS as boundary conditions for Newcomb's eigenfunctions reconstruction in the whole plasma volume.

The subsequently upgraded code adds the internal measurements as boundary conditions and further on we will show some preliminary result.

As first approach, we create the # 99999 discharge through an averaging process of magnetic signals coming from the external pick-up coils in order to evince the underlying magnetic topology of RFP crash events.

Each crash event is identified in the F profile of different discharges in the RFX-mod database. Then, each crash is re-scaled in time in order to define a common $t = t_0$ that would correspond to the crash in the dominant mode's amplitude ($m = 1$). Signals are re-scaled also in space to set the toroidal position ϕ_{lock} at which the crash

[4] The higher is the toroidal number n of the perturbation, the higher the shielding of the vacuum vessel will be. Frequencies beyond 10 Hz are almost totally shielded.

[5] As reference, see paragraph 2.4.2

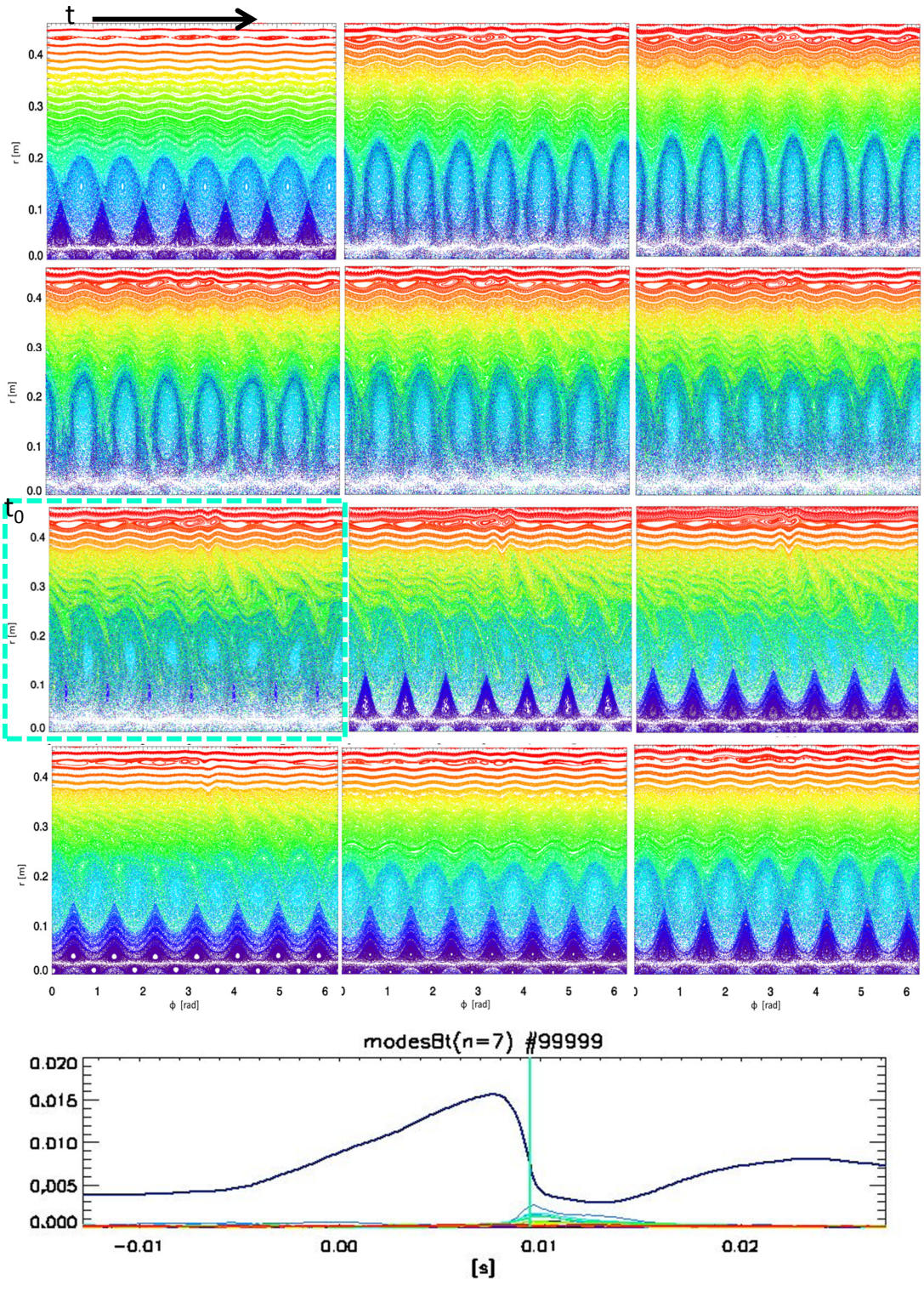

FIGURE 4.9: Time evolution of # 99999 discharge. The black arrow at the top left corner indicates the temporal evolution. The cyan dashed panel depicts the topology at the crash instant t_0. As a reference we also draw the amplitude of the dominant (m, $n = 7$) mode (the toroidal component, as the deep blue line) and the secondary modes (colored lines). The cyan vertical line represents t_0.

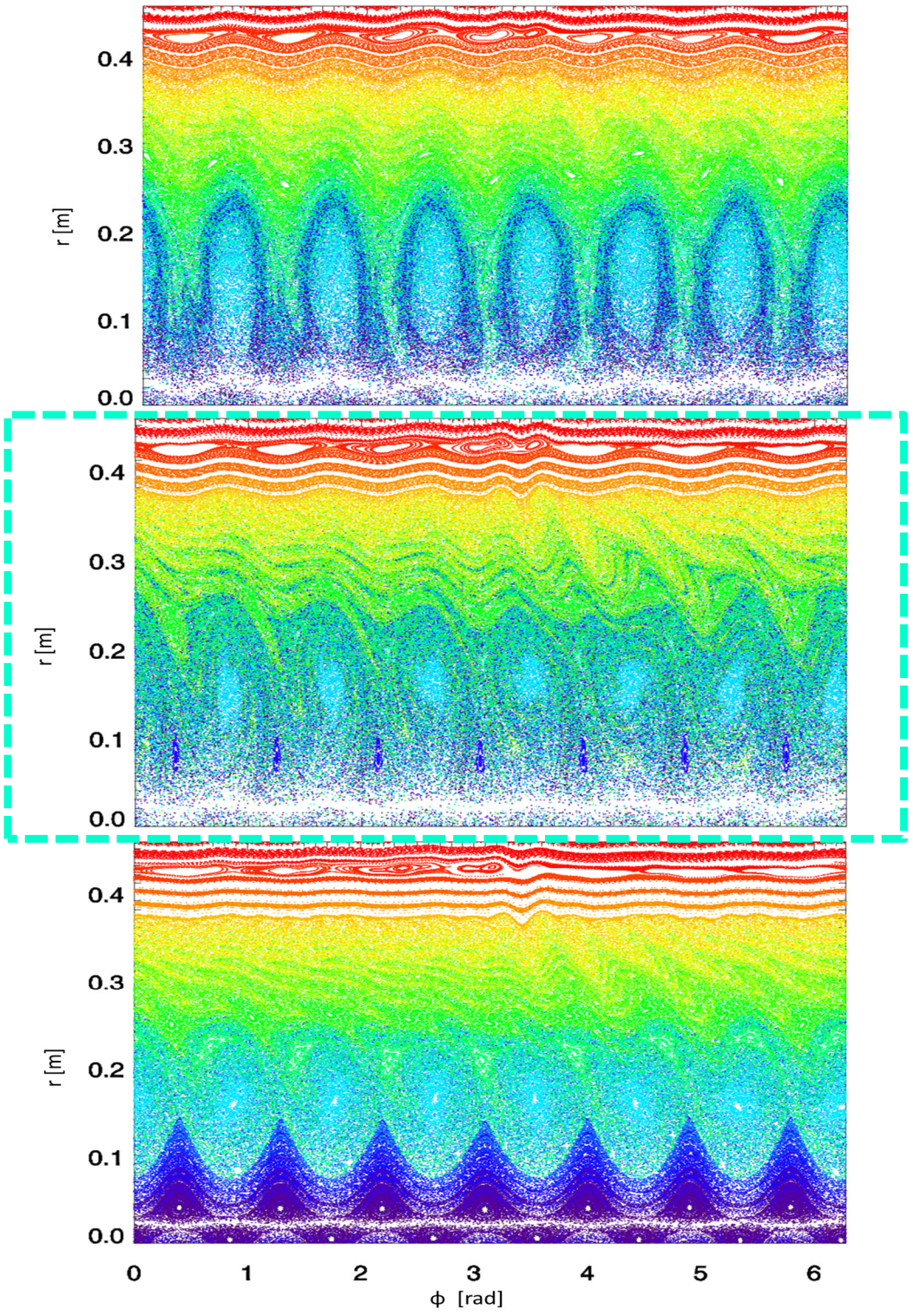

FIGURE 4.10: Three Poincaré plots for the # 99999 discharge. The cyan dashed panel depicts the topology at the crash instant. The upper reconstruction refers to the topology 2 ms before the crash and the bottom one refers to the topology reconstructed 2 ms after the crash event. We can see how the topology changes before and after the crash event, with the emergence of new diffusive structures that propagate from the core toward the plasma edge.

events take place. Eventually, we have an unique fictitious discharge, the $\#\ 99999$, defined in terms of averaged and re-scaled signals coming from the external pick-up coils.

In Figure 4.9 we try to give a description of how the reconstructed magnetic topology for the $\#\ 99999$ evolves in time: we show a series of Poincaré maps in the (r, ϕ) plane at $\theta = 0°$ and for chosen points in time. The cyan dashed panel depicts the topology when the dominant mode's amplitude crashes. In the bottom panel, we show as a reference the amplitude of the dominant mode and the secondary modes with a smaller in amplitude. The vertical cyan line represents the crash instant t_0.
In Figure 4.10 we present a selection of three Poincaré plots where the cyan dashed panel depicts the topology at t_0 while the upper reconstruction refers to the topology 2 ms before and the bottom one refers to the reconstruction 2 ms after the crash event. At this point, we should take a closer look at the corresponding reconstructed eigenfunction (successively integrated by the FLiT code in order to obtain the Poincaré plots). From the bottom panel of Figure 4.9 we can state that although there is not a complete suppression of the dominant's amplitude, at $t = t_0$ secondary modes are growing. Their growth is associated to the growth of chaos that progressively degrades the SHAx condition as can be seen in Figure 4.10. In the same figure we can see the emergence, after the crash event, of new diffusive structures converging towards the edge in correspondence of the toroidal angle, ϕ_{lock}, position of locking in phase of $m = 1$ modes. These structures can be related to the radial diffusion of magnetic field lines starting from the X-point at the plasma core, running through its volume, toward its edge.

4.4.1 Comparison with a real discharge

A better understanding of the evolution in time of the crash event can be obtained by comparison with a real case, the discharge # 29255, analyzed adding ISIS signals as boundary conditions for the eigenmodes reconstruction.

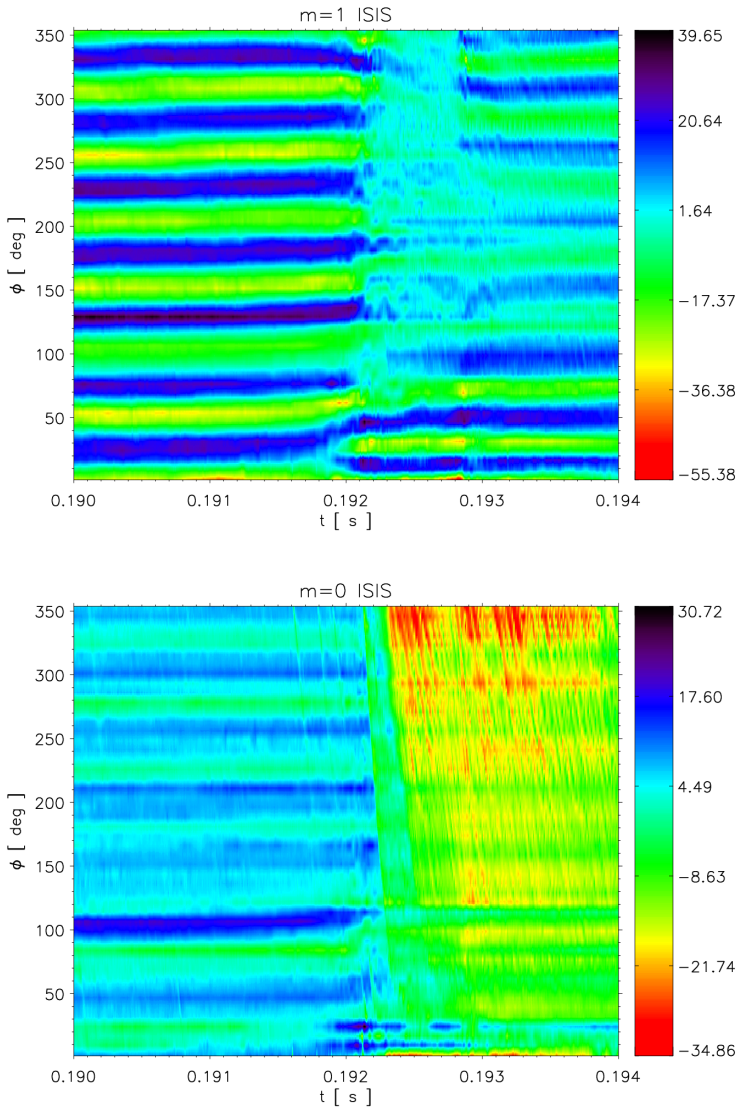

FIGURE 4.11: Contour plot of $m = 1$ (upper panel) and $m = 0$ (lower panel) components of magnetic toroidal signals measured by two toroidal arrays of 48 coils.

In Figure 4.11 we show the $m = 1$ and $m = 0$ ($n = 7$) toroidal magnetic field components measured in time by the two toroidal arrays of 48 coils of ISIS diagnostic.

It is clear that a significant change exists in the structure of the dominant $n = 7$ magnetic signals before and after the crash event similar to what has been observed in [89] and already shown in Figure 4.7. In Figure 4.12 we show ISIS signals zoomed in

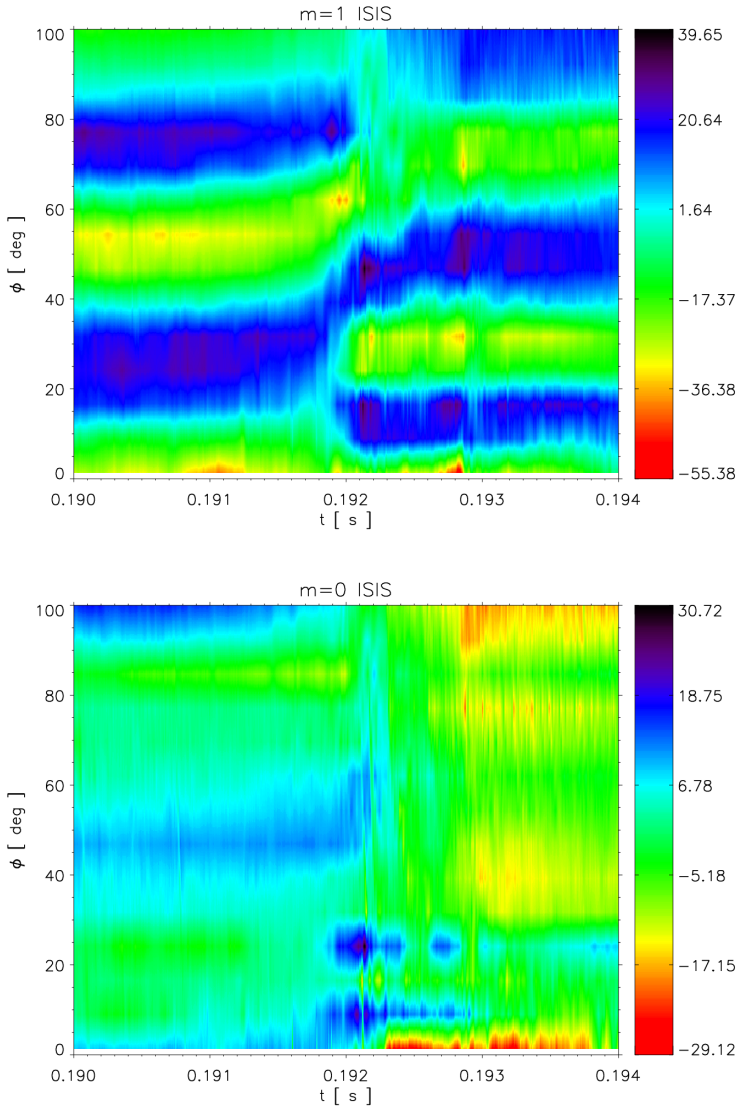

FIGURE 4.12: Contour plot of $m = 1$ (upper panel) and $m = 0$ (lower panel) components of magnetic toroidal signals measured by two toroidal arrays of 48 coils, zoomed in the range $0° < \phi < 100°$.

the toroidal angle, between 0° and 100°, in order to better highlight the region where modifications happen.

The locking in phase at $\phi = \phi_{lock}$ of the $m = 1$ modes seems to forerun the crash event, while after it (tens of milliseconds afterwards) it can be stated a likely transfer of magnetic energy from the $m = 1$ to the $m = 0$ modes. Actually, the latter show a very localized structure in correspondence of the locking of $m = 1$ modes with their consequent locking in phase at the same ϕ_{lock} and the formation of the known funnel-like arrangement [31].

The contour plots shown in Figure 4.11 and in Figure 4.12 cannot be extracted for the

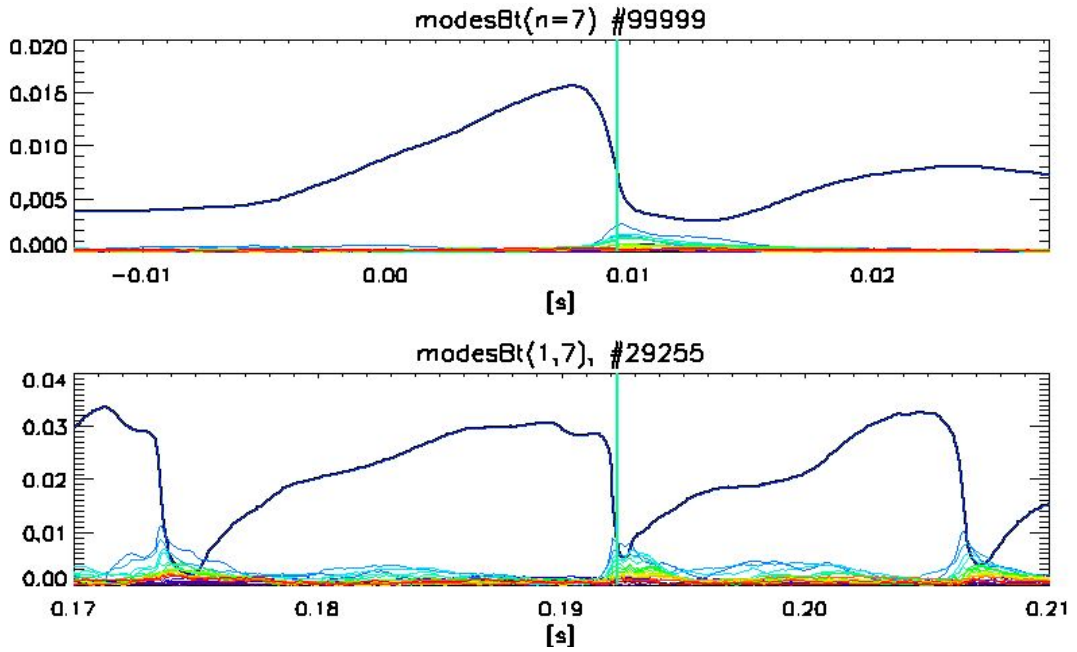

FIGURE 4.13: Amplitude of the dominant and secondary modes (in Tesla) for the discharge # 99999 and # 29255. The cyan vertical line represent the instant identified as the crash.

99999 discharge since the ISIS signals are not yet available for analyses. Nevertheless, we can compare the amplitude of the dominant and secondary modes and their behavior.

In Figure 4.13 we can see that there is not a complete suppression of the dominant's amplitude in the # 99999 discharge and, with respect to the *real* # 29255, the SHAx is better preserved during the crash event. If we take a closer look at the eigenfunctions, we can say that in both cases the most important secondary modes are the $m = 1$, $n = 8, 9, 10$ (though they are not the only ones) whose amplitude grows just before the crash event and than their locking-in-phase causes the crash of the dominant mode. In the real case the SHAx condition is progressively lost due to the chaos emerging with the growth of the secondary modes whose final main effect is the suppression of a single dominant helicity in favor of a Multiple Helicity condition.

In Figure 4.14 we show three representative Poincaré maps for the # 29255 discharge around the crash event, similarly to what we have done in Figure 4.10. Another topological characteristic that this discharge shares with the *averaged* # 99999 is the emergence of diffusive structures that move toward the edge converging at the toroidal position of the locking-in-phase of $m = 1$ (and also $m = 0$) modes.

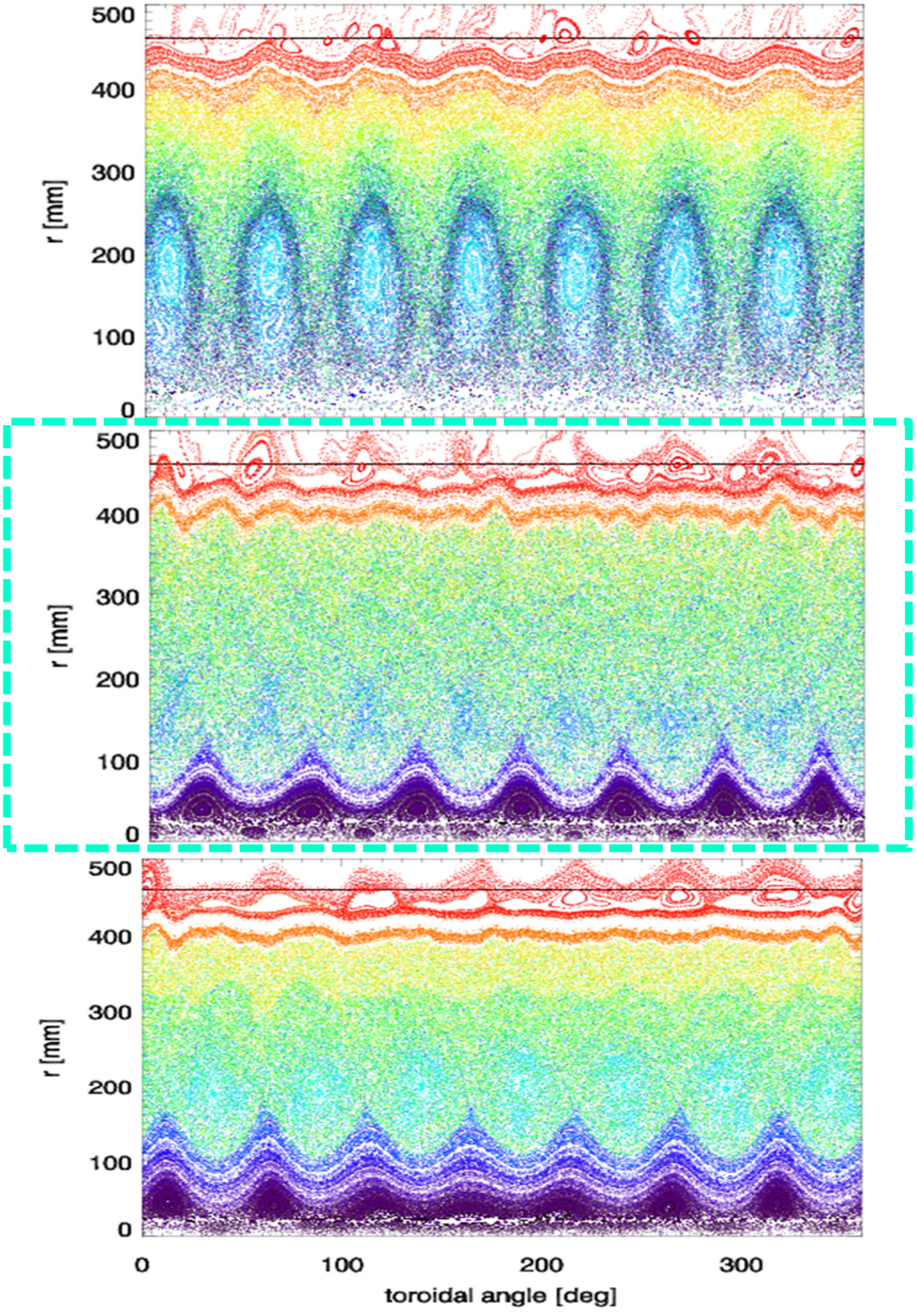

FIGURE 4.14: Three Poincaré plots for the # 29255 discharge. The cyan dashed panel depicts the topology at the crash instant. The upper reconstruction refers to the topology 2 ms before the crash and the bottom one refers to the topology reconstructed 2 ms after the crash event.

4.5 Ion heating in magnetic reconnection

During magnetic reconnection plasmas can be accelerated to a speed comparable to the Alfvén velocity, as Petschek's model describes. Plasmas gain kinetic energy during reconnection and the energy can then be thermalized by ions through viscosity. Simultaneously, toroidal flux is generated while the poloidal flux is consumed. Consequently, the magnetic energy decrease during the relaxation process is a strong candidate for an ion-heating source.
In order to deeply investigate this mechanism, a reliable estimate of the ion temperature profile should be given. Nevertheless, ion temperature in the scrape-off layer is rarely measured with high temporal resolution: its measurements are indeed of high interest in order to fully understand plasma-wall interaction and transport processes at the edge. Furthermore, the habit exists of adopting a *cold ion* approximation (due to the lack of systematic experimental data) which is in contradiction with the measured T_i profiles in the SOL [93] and that typically exceeds the electron temperature profiles. In the past, various methods have been discussed for measuring ion energy (for example, by *Staib et al.* in [94]) but the estimate of ion temperature cannot be obtained using the standard sweeping Langmuir probe because of an excessive electron current that masks the changes of ion current for a probe potential above the plasma potential.

So as to ease fast T_i measurements, *Komm et al.* [95] recently refined the design of an $E \times B$ analyzer already used by *Matthews* in 1984 on *DITE* [96] and by *Staib* on *ASDEX* to measure the ion distribution in tokamak edge plasmas. The analyzer is based on the fact that in a region of uniform electric field $\mathbf{E}$ and uniform magnetic field $\mathbf{B}$ the guiding centre drift velocity of a charged particle $\mathbf{v}_D = (\mathbf{E} \times \mathbf{B})/B^2$ is independent of its velocity parallel to $\mathbf{B}$. Application of an electric field within the probe normal to the magnetic field dominant at the plasma edge achieves a spatial dispersion of the ions which is a function of the ion parallel velocity distribution.

Measurements of fast ions temperature have been performed during ELMs in the scrape-off layer of ASDEX-Upgrade tokamak to demonstrate the successful operations of the probe. A similar campaign has been conducted on the smaller COMPASS tokamak operating at IPP.CR in Prague, Czech Republic. In the framework of the EUROfusion Enabling Research project WP14-ER-01/ENEA-RFX-02 "Magnetic reconnection in fusion plasmas", the author has participated visiting IPP.CR in Prague

during May 2014. The purpose of the visit has been to perform data analysis of experiments with the $\mathbf{E} \times \mathbf{B}$ analyzer on COMPASS, and to work on the detection of fast ions from the magnetic reconnections caused by RMP system.
In June 2014 the $\mathbf{E} \times \mathbf{B}$ analyzer was sent from IPP.CR in Prague to Consorzio RFX, still as a deliverable of the ER project, in order to be exploited during experimental campaigns featuring tokamak and low-current RFP discharges.

Let us first introduce how the analyzer works and then discuss the results obtained and the issues encountered during the experiments.

4.5.1 $\mathbf{E} \times \mathbf{B}$ analyzer and T_i profile

The analyzer consists of an entrance slit, which is negatively biased and as such repels electrons but allows ions to pass inside a cavity, where two planar electrodes biased at potentials V_{top} and V_{bottom} create an electric field $E = (V_{top} - V_{bottom})/d$ (d is distance between the electrodes). This field combines with the tokamak magnetic field and results in an $E \times B$ drift, which is deflecting ions from line-of-sight trajectory of length L towards an array of 12 collectors on the back plate of the cavity.
The equations of motion for an ion in this region are given by [96]:

$$\begin{aligned} x &= \rho\ sin\psi_0 - \rho\ sin(\psi_0 + \omega t) + v_D t \\ y &= \rho\ cos\psi_0 - \rho\ cos(\psi_0 + \omega t) \\ z &= v_{\|} t \\ \omega \times \rho &= [(U_x - v_D)^2 + U_y^2]^{1/2} \\ sin\psi_0 &= U_y/(\omega \times \rho) \end{aligned} \tag{4.4}$$

where U_x and U_y are the initial components of velocity perpendicular to $\mathbf{B}$, $|v_D| = E/B$ is the guiding centre drift, $v_{\|}$ is the velocity parallel to $\mathbf{B}$ and ω is the angular frequency. The ion guiding centre displacement on the collector plane is inversely proportional to their parallel velocity:

$$\Delta_x = \frac{E}{B_{loc}} L \frac{1}{v_{\|}} \tag{4.5}$$

where L is the length of the electrodes inside the cavity. The ions are accelerated when they pass from plasma into the cavity by speed v_{acc}

$$v_{\parallel} = v_i + v_{acc} = v_i + \sqrt{\frac{2e(V_{plasma} - V_{mid})}{m_i}} \tag{4.6}$$

where V_{mid} is the potential between the electrodes

$$V_{mid} = (V_{top} + V_{bottom})/2 \tag{4.7}$$

Since usually $|V_{mid}| \gg |V_{plasma}|$, we assume the plasma potential to be zero. It should be noted that the potential of the slit does not influence the acceleration of the ions. During the experiment, the collector currents are measured and transformed to velocities using Equation 4.5 and Equation 4.6:

$$I_c(\Delta_x) = I_0 exp\left(\frac{E^2L^2}{B^2\Delta_x^2 T_i}\right) \tag{4.8}$$

The ion temperature is then reconstructed by the fit of tail of the velocity distribution function, considered to be a Maxwellian distribution. When useful signals are found only on 2 collectors (a and b), the ion temperature is calculated directly by using the formula

$$T_i = \frac{m_i EL}{2eB_{loc}}\left(\frac{1}{\Delta_x^2(a)} - \frac{1}{\Delta_x^2(b)}\right)/log\left(\frac{I_{col}(b)}{I_{col}(a)}\right) \tag{4.9}$$

The measurement does not involve any sweeping and so the temporal resolution is only limited by the frequency of the data acquisition system or frequency of induced noise.

Design of the analyzer

The refined version of $\mathbf{E}\times\mathbf{B}$ analyzer has first been designed for mid plane reciprocating manipulators on AUG and COMPASS, which have identical interface. The analyzer as shown in Figure 4.16 is contained within a 5 mm thick graphite cylindrical housing of 60 mm in diameter and 150 mm length. The housing presents an orifice in it which serves as the entrance for the ion flux. Since its dimensions (approximately 53 mm) are larger than ion Larmor radius ($\rho_L < 1\ mm$), it is possible to assume that the ion flux arriving into the slit is not attenuated by the housing. The orifice area as an effective collecting area for ions falling onto the slit plate, neglecting possible finite

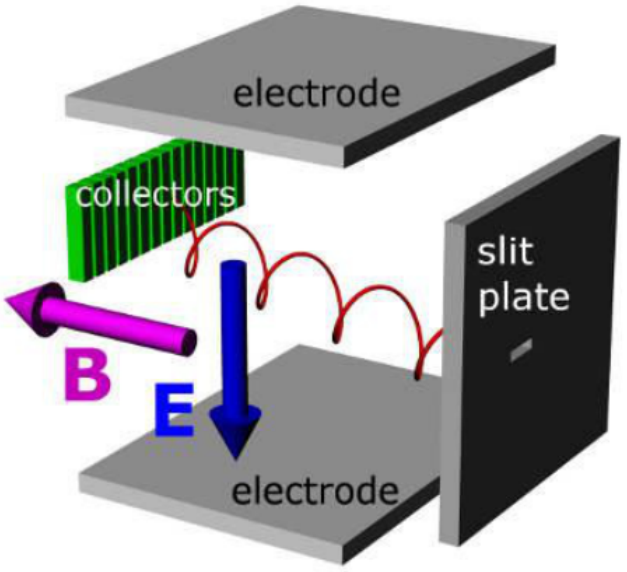

FIGURE 4.15: Conceptual sketch of the ExB analyzer.

Larmor effects.

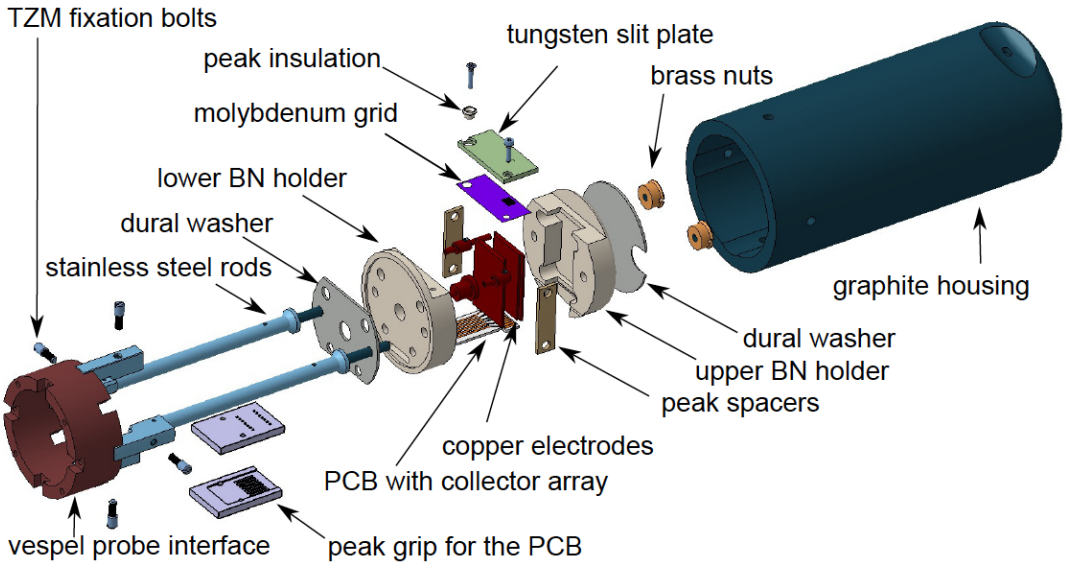

FIGURE 4.16: Schematic view of the ExB analyzer probe head.

Inside the housing there is the entrance slit to the proper cavity where collectors are placed. The entrance slit is machined into a 2 mm thick tungsten plate with knife-edge shape. The slit is oriented with its longer side along the collector array and this ensures that all ions inside the cavity pass through the same potential imposed by the electrodes.

The internal cavity is made of BN (Borum-Nitride) parts with two copper planar

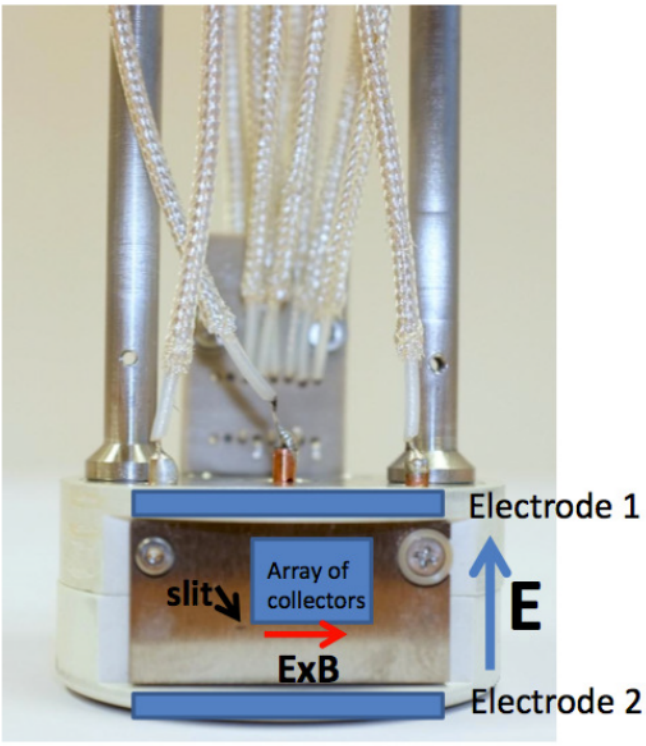

FIGURE 4.17: Front view of the analyzer with the tungsten slit plate in front. This figure is taken from [95]

electrodes. In principle, the electrodes should create sufficient path for the $\mathbf{E} \times \mathbf{B}$ drift to disperse the ions along the collectors. The number of segments is limited by the number of pins in the manipulator interface and number of available channels in fast data acquisition system.

Experimental issues

In order to measure displacement of ions and their parallel velocity, it is essential to know the precise orientation of the probe head with respect to the local magnetic field. Misalignment of few degrees (within the manufacturing precision) results in systematic shift in measured energies. Since energy depends on $1/\Delta_x^2$, the effects of misalignment can be dramatic.

The adopted technique for a correct alignment consists in a modulation of the slit and electrode voltages by short pulses, with the voltages dropped to respectively fixed values. This allows an electron beam to enter the cavity and sharp electron signal on one of the collectors helped to calibrate probe position.

Another issue is encountered in the arcing on slit plates.

Then, although the analyzer should measure only positive collector currents, negative currents were also experimentally observed. Since electrons from plasma are much faster than ions, they are not affected by the drift and so their footprint should be observed only on collectors facing the slit. However, the negative signals were present on all collectors. One hypothesis might be that the signal comes from secondary electrons, which are created within the cavity. One possible source could be the PCB with collector array. Electrons emitted either from the collectors or from the substrate (collectors are separated by 0.3 mm gaps) could be repelled by potential between electrodes and bounced to the neighboring collector. Another source could be the back side of the slit, where some ions may impact. It was observed that the negative currents diminish when the potential between electrodes is sufficiently low (-200 V). However, such low potential accelerates ions, which are then less affected by the drift and consequently less dispersed on the collectors. This is the reason why useful signals are not always found on all collectors. Further investigation should be dedicated to this matter.

In the following subsections, we are giving on overview of the results obtained from experimental campaigns on ASDEX-Upgrade, COMPASS and RFX-mod. As part of the Ph.D. research project, the author actively participated to campaigns performed on the last two devices.

Experiments on AUG

The first experiments with measurements coming from the $\mathbf{E} \times \mathbf{B}$ analyzer were performed on ASDEX-Upgrade and COMPASS.
On ASDEX-Upgrade, measurements were carried on by *Komm et al.* [97] using multiple reciprocations of the mid plane manipulator in a typical discharge with $B_\phi = 2.45\,T$ and $I_p = 800\ kA$, heated by 0.4 MW of ECRH.
In Figure 4.18 we show time traces of signals coming from the $\mathbf{E} \times \mathbf{B}$ analyzer during small ELMs on AUG. Collector currents can be resolved and ion temperature can be calculated by fittiing the signals, which correspond to the tail of the distribution function. Since the pick-up noise on AUG is minimal, the T_i measurements were sampled at 500 kHz. High temporal resolution is essential to obtain ion temperature fluctuations. The distribution of measured T_i samples is shown in Figure 4.19 and shows the presence two distinctive ion populations. The cold population has mean temperature 5 eV, while the hot population has mean T_i around 30 eV. It is possible to attribute the low temperature population to ions originating from plasma fueling and the hot

population to ions transported by turbulence from the separatrix. The ratio of the two population changes during the density ramp up, which corresponds to more intensive fueling due to the ECRH heating.

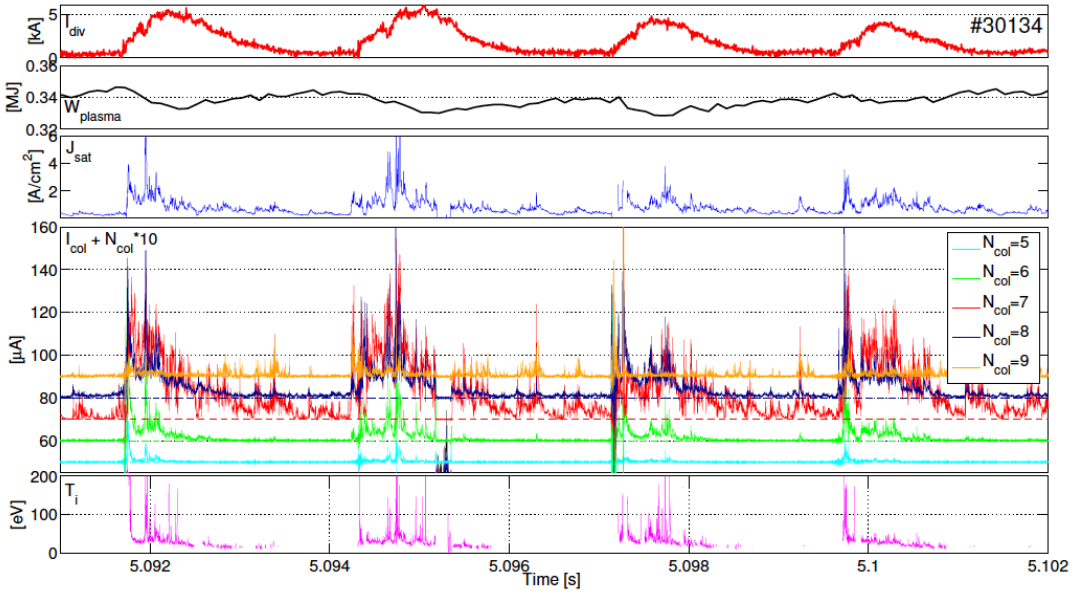

FIGURE 4.18: From top to bottom: Inner divertor shunt current, plasma energy, ion saturation current density, currents to $\mathbf{E} \times \mathbf{B}$ analyzer collectors and ion temperature measured by the $\mathbf{E} \times \mathbf{B}$ analyzer during small ELMs on AUG. The figure is taken from [95]

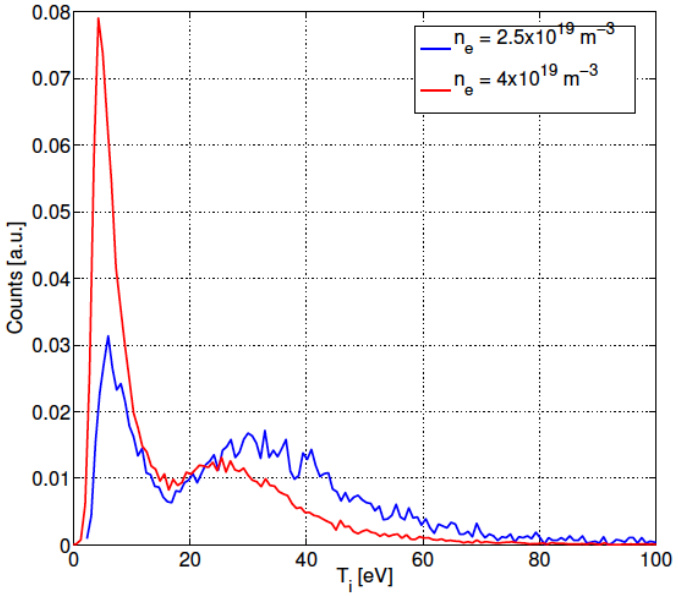

FIGURE 4.19: Histogram of measured T_i at low ($n_e = 2.5\ 10^{19}\ m^{-3}$) and high ($n_e = 4\ 10^{19}\ m^{-3}$) density. The figure is taken from [97].

4.5.2 Experiments on COMPASS

On COMPASS, measurements were obtained during the flat-top of diverted L-mode discharges with $B_\phi = 1.5\ T$ and $I_p = 160\ kA$. The $\mathbf{E} \times \mathbf{B}$ analyzer was mounted on the reciprocating manipulator at outer midplane and used both in reciprocating and fixed position modes during a series of discharges with varying density.

Due to presence of the high-frequency noise the time resolution of the measurements was limited to 20 kHz. Example distribution of acquired ion temperatures at low density discharge # 7114 ($n_e = 3\ 10^{19}\ m^{-3}$) is shown in left panel of Figure 4.20: the entrance slit was located 17 mm from the separatrix position calculated by EFIT.

Only samples with relative error of the fit lower than 50% were considered for the analysis, which discarded 20% of the samples. The distribution shows a non-Maxwellian intermittent nature of the fluctuations. Despite relatively low mean temperature at 24 eV, 8% of fluctuations surpass double of the value. Although there is some trend of increasing T_i with increasing J_{sat} measured by the entrance slit (see right panel of Figure 4.20), the correlation is rather weak.

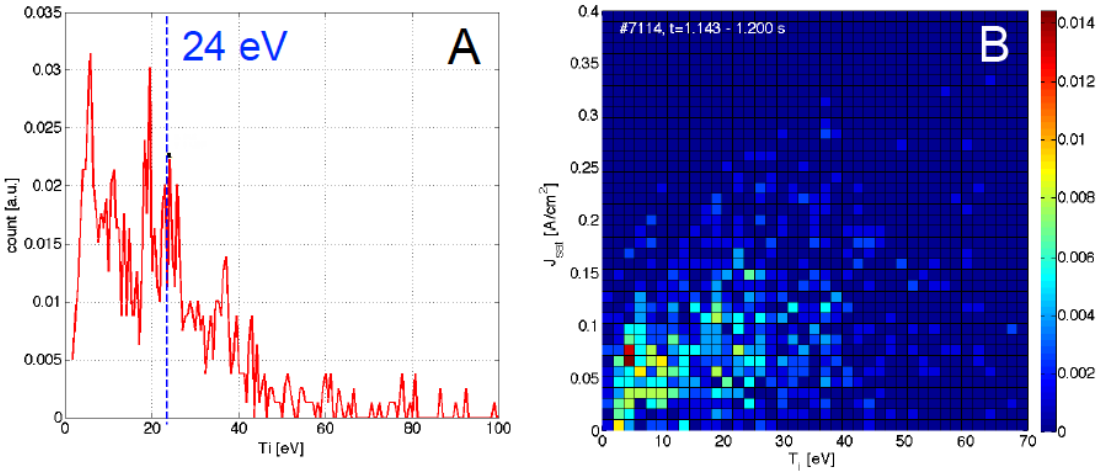

FIGURE 4.20: Left: distribution of measured T_i in COMPASS discharge # 7114 . Right: T_i dependence on J_{sat}. The figure is taken from [97].

In the end, both on COMPASS and AUG, measurements show that the ion temperature fluctuations are in general non-Maxwellian, with high-energy tail, which is expected to have impact on plasma-wall interaction mechanisms, such as sputtering. Measurements at AUG have also shown the presence of two ion populations with distinctive temperatures, which might be attributed to ions carried by turbulence from the separatrix and ions from fueling.

Analyses of the experiments with application of RMP fields on COMPASS tokamak are still under investigation.

4.5.3 Experiments on RFX-mod

The $\mathbf{E} \times \mathbf{B}$ ion energy analyzer was sent from Prague to Padova in May 2014, following preliminary preparation work, and exploited in experimental campaigns featuring low-current ($I_p \leq 400\ kA$) RFP discharges during July 2014.
The first issue encountered was that the analyzer's cavity was not suitable for the relatively low magnetic field in RFX-mod: the ion's Larmor orbit was too large to actually reach the collectors and nearly all the ions hit the electrodes. The probe was originally designed for AUG operating at 2 Tesla and adaptation in the measurement scheme was applied in order to observe the high energy ions.
Despite a considerable effort during the experimental campaign there was no evidence of the fast ions in the plasma edge. In Figure 4.21 we show the characteristic signals

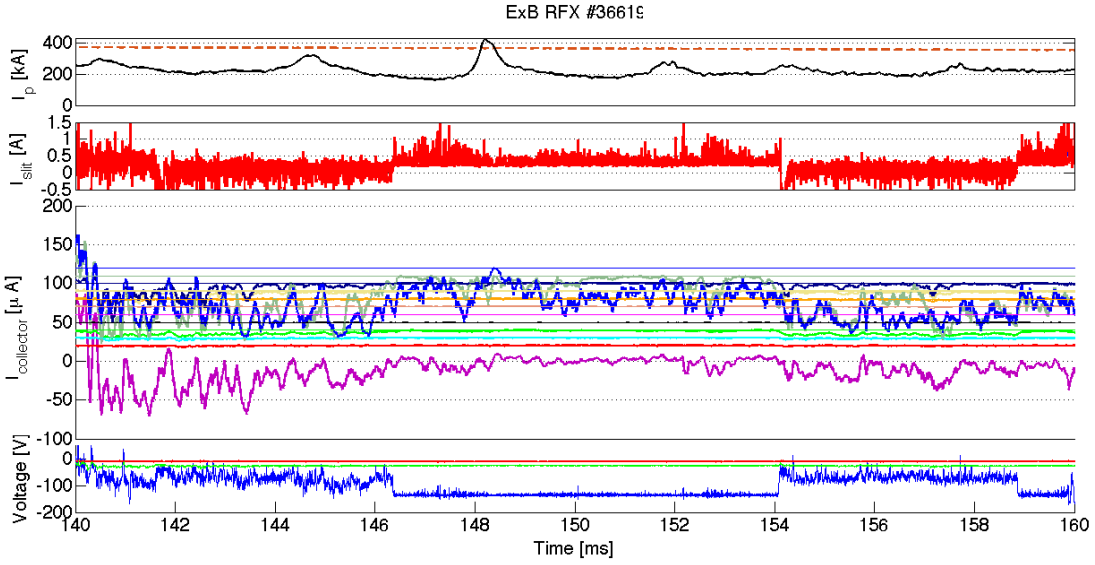

FIGURE 4.21: From top to bottom: plasma current, ion saturation current, currents to $\mathbf{E} \times \mathbf{B}$ analyzer collectors and voltage on the slit measured by the $\mathbf{E} \times \mathbf{B}$ analyzer during low-current RFP discharges on RFX-mod.

obtained in one of the discharges were the analyzer had been exploited: the signal from one of the electrodes (here shown as segment 1) is not showing any significant correlation with the signal showing the reconnection events.
The measurements were also hampered by a significant amount of pick-up noise induced on the current measurements and by a large amount of electrons inside the

analyzer's cavity, whose origin is still unknown. Furthermore, issues concerning a correct biassing of the slit might also exist in order to explain the amount of electrons inside the cavity.

As a consequence, a new $\mathbf{E} \times \mathbf{B}$ analyzer with larger cavity has been built to perform measurements specifically at the edge of RFX-mod. The exploitation of this device is foreseen in future campaigns.

Part IV

Conclusions

Chapter 5

Conclusions

In this chapter we collect all the results obtained in the development of the thesis in order to give the reader a detailed report of each argument we have investigated. In the very last section, entitled *Summary and future perspectives*, we will schematically and tautly describe our results together with an outline of open questions and future studies.

5.1 Transport analysis

The studies on the modifications of transport channels at the edge of the RFX-mod plasma have been developed both in RFP and in tokamak configuration, during experiments with application of external 3D magnetic perturbations. RMPs have shown to be able to completely suppress ELMs in several existing devices and they will be fully exploited in the ITER experimental reactor. It is widely accepted the importance of understanding the fundamental transport mechanisms at the edge and how transport channels are affected by the application of 3D magnetic fields.
More in detail, the study of edge plasma transport properties requires measurements with high spatial and temporal resolution. The insertable *U-probe* has been exploited for this purpose, though its use is limited to low plasma current discharges in order to avoid damages to its components caused by an excessive heat load. The U-probe provided detailed information about electrostatic fluctuations of temperature, density and therefore particle and energy fluxes.
Analyses have been discussed first in RFP and then in tokamak configuration thanks to the versatility of the RFX-mod device, while trying to develop an analogy between

the two magnetic configurations. We will present first the RFP and then the tokamak results.

5.1.1 RFP

In the RFP case it has been possible to extract radial profiles of electrostatic fluxes due to an abundant statistics: after choosing the region in r/a where their contribution is peaked, the fluxes have been spectrally analyzed both in frequency and as a function of the transverse wave number $k_\perp$, as discussed in Section 3.3.
The results suggest that both energy and particle transport driven by electrostatic fluctuations are concentrated in the range:

$$20\ m^{-1} \leq k_\perp \leq 60\ m^{-1}$$

with a maximum peaked around $k_\perp \sim 40\ m^{-1}$ which corresponds to $k_\perp \rho_i \sim 0.1$, where ρ_i is the ion Larmor radius.
An estimate of the phase velocity for the fluctuations is given:

$$v_{phase} \sim 9.5\ km\ s^{-1}\ .$$

The estimated phase velocity has been compared to the electron diamagnetic and the $\mathbf{E} \times \mathbf{B}$ velocity. We have eventually concluded that the fluctuations tend to propagate in the same direction of the electron diamagnetic flow but with a higher velocity, although lower than the $\mathbf{E} \times \mathbf{B}$ one. This latter observation might be a first rough approximation, since the extrapolated dispersion relation is strongly dependent on the fit technique used to extract the phase velocity.
Our investigations have included studies to relate transport properties with the underlying magnetic topology at the edge, exploiting Poincaré maps obtained through the field line tracing code FLiT. In presence of a rotating (1, 7) magnetic perturbation, measured plasma parameters have exhibited a sinusoidal time evolution: this oscillatory behavior of the PWI as a function of time can be better understood when the modulation on fluctuating values of transport properties is considered as a function of the local helical angle

$$u(\theta, \phi; t) = \bar{m}\theta - \bar{n}\phi + \varphi_{\bar{m},\bar{n}}(t)\ .$$

All the profiles, presented in Section 3.4 and 3.4.1, were exhibiting a maximum in the region $\pi/2 \leq u_{1,-7} \leq \pi$ and a minimum around $u_{1,-7} \sim 3\pi/2$, corresponding to different topological regions where the $m = 0$ island's O- and X-point of the externally applied magnetic perturbation lie, as shown in the Poincaré map in 3.4.1.
The following step, as discussed in 3.4.1, has been to analyze the behavior of the electrostatic fluxes around the O- and X-point of the applied perturbation in order to extract the typical transverse wave numbers for the small scale fluctuations. Distributions show a peak for $30\ m^{-1} \leq k_\perp \leq 60\ m^{-1}$ followed by a consequent reduction: the fluxes show a similar behavior, nevertheless their distribution around the X-point is quenched with respect to the O-point distribution due to a reduction in the fluctuations amplitude. Hence we computed both the power spectra of density and potential fluctuations and their relative phase $\alpha_{n\phi}$ as a function of the transverse wave number. The results suggest no difference between the O- and the X-point contribution in the phase relation given by $\alpha_{n\phi}(k_\perp)$, whereas the power spectra confirm that the reason why the fluxes are lowered around the X-point region is linked to a reduction in the fluctuations amplitude and not to profile of the relative phase.

5.1.2 Tokamak

While discussing the tokamak configuration, we have performed analyses similar in all aspects to the RFP case: measurements were taken during the first part of the discharge, where $q_a \simeq 2.1$ and with an applied (2, 1) magnetic perturbation. Spectral analyses of the electrostatic fluxes were presented in Section 3.5 and have shown a negative peak around $f \sim 20\ kHz$ and an *outward* contribution mainly concentrated in the range $80\ kHz \leq f \leq 120\ kHz$.
The successive step in the analyses has dealt with the investigation on transverse wave numbers that mostly contribute to transport driven by electrostatic fluctuations at the edge. We have found that fluctuations tend to propagate in the same direction of the electron diamagnetic flow and that both energy and particle transport are concentrated at values of $|k_\perp|$ in the range

$$30\ m^{-1} \leq |k_\perp| \leq 90\ m^{-1}$$

with a maximum peak around $|k_\perp| \sim 70\ m^{-1}$, which corresponds to peaks around $|k_\perp|\rho_i \sim 0.06$. In RFP configuration electrostatic fluxes showed peaks around $k_\perp\rho_i \sim 0.1$, which is almost twice the value found in the tokamak case.

Subsequently, we extrapolated a dispersion relation for the tokamak case from which we have estimated a phase velocity for the fluctuations:

$$v_{phase} \sim 8\ km\ s^{-1}\ .$$

We have therefore concluded that fluctuations tend to propagate in the same direction of the electron diamagnetic flow with approximately a phase velocity of the order of the $\mathbf{E} \times \mathbf{B}$ one.

Thereafter, in Section 3.6 we have inferred the poloidal maps of various transport relevant quantities. In this case, the poloidal angle of the perturbation has been chosen as a reference frame consistent with the rotation of the perturbation, under the assumption of a rigid body rotation. Profiles of electron density, radial electric field, electrostatic particle and energy flux and the diffusion coefficient are found to follow the symmetry of the dominant ($m = 2$, $n = 1$) perturbation. The depletions around $\theta_{2,-1} \simeq \pi/2$, $\theta_{2,-1} \simeq 3\pi/2$ and the enhancement at $\theta_{2,-1} \simeq \pi$ correspond to the poloidal locations of the two X-points and the O-point of the ($m = 2$, $n = 1$) island, visible in the Poincaré map in 3.6.1.

To carry on the analogy, in 3.6.1 we have analyzed the behavior of the electrostatic fluxes around the O- and X-point of the applied perturbation; in particular, the applied (2, 1) magnetic perturbation leads to an increase in the fluctuation level in the discharge phase when $\theta_{2,-1} \sim \pi$.

In this case, analyzing the phase relation between $k_\perp$ and frequency, we can see a clear difference in the phase velocity of the fluctuations when we compare the O- with the X-point distribution. In accordance with the RFP case, the differences between the O- and X-point distributions of the electrostatic fluxes depend on the amplitude of the fluctuations and not on the relative phase. Profiles of electrostatic fluxes show a consistent accumulation of points for $20\ m^{-1} \leq |k_\perp| \leq 100\ m^{-1}$ for both distributions, then the O-point contribution reduces to zero while profiles display an *inward* contribution around the X-point region, observation which will deserve further investigations in the future.

5.2 Topology analysis

In this part of the thesis we have focused our interest in the description of the underlying magnetic topology in presence of spontaneous 3D effects such as magnetic

reconnections.
In RFX-mod, recent studies have shown that reconnection events lead to the formation of a toroidally localized perturbation (with poloidal number $m = 0$) that strongly perturbs edge plasma profiles. It has been found that this toroidal localized perturbation corresponds to a spontaneous generation of a poloidal *current sheet*. The localized perturbation is due to the non-linear coupling of tearing modes with $m = 1$.
The common feature of the reconnection events we have studied is the growth of the $m = 1$ modes, rapidly followed by an abrupt decrease (*crash*) in their amplitude, with a large part of magnetic energy transferred to an $m = 0$ perturbation.

We have therefore considered an ensemble of discharges performed at high plasma current, showing the crash traces in the reversal parameter profile as discussed in Section 4.4. Since we wanted to isolate the fast dynamics common to all these experiments and dependent on the reconnection mechanism discussed throughout Chapter 4, we created the $\#\ 99999$ discharge through an averaging process over the signals coming from the external pick-up coils. At this point we exploited the field line tracing code FLiT to obtain a temporal evolution of the magnetic topology changes around the crash event in the $\#\ 99999$ dynamics. From the temporal evolution described through Poincaré plots we have seen the emergence, after the crash event, of new diffusive structures converging towards the edge in correspondence of the toroidal angle where $m = 1$ modes lock in phase. These structures have been related to the radial diffusion of magnetic field lines starting from the X-point at the plasma core, running through its volume, toward its edge.
Analyses carried on with the discussion of the comparison with a real discharge. The most important remark regards the dominant's amplitudes as compared between the two cases. In the $\#\ 99999$ discharge, the dominant's amplitude is not completely suppressed and therefore the SHAx is better preserved during the crash event. In the *real* case the SHAx condition is progressively lost due to the chaos emerging with the growth of the secondary modes whose final main effect is the suppression of a single dominant helicity in favor of a Multiple Helicity condition[1].
At last, the averaged $\#\ 99999$ and the real discharge share a topological characteristic which is the emergence of diffusive structures that move toward the edge converging at the toroidal position of the locking-in-phase of $m = 1$ (and also $m = 0$) modes.

The last step in our analyses has been the investigation of the distribution of ion

[1] A description of SH and MH conditions is given in Section 2.3.

energy at the edge through the $\mathbf{E} \times \mathbf{B}$ analyzer.

During magnetic reconnection, plasmas can be accelerated and gain kinetic energy at the expenses of magnetic energy; the magnetic energy decrease during the relaxation process is a strong candidate for the ion-heating process. In order to deeply investigate this mechanism, a reliable estimate of the ion temperature profile should be given. Nevertheless, ion temperature in the scrape-off layer is rarely measured with high temporal resolution: its measurements are indeed of high interest in order to fully understand plasma-wall interaction and transport processes at the edge.

We have exploited the $\mathbf{E} \times \mathbf{B}$ analyzer, whose design has been refined by *Komm et al.* as discussed throughout Section 4.5 and 4.5.1, in experiments performed in COMPASS tokamak in Prague and in RFX-mod.

On COMPASS, the experiments showed an ion distribution with a non-Maxwellian intermittent nature of temperature fluctuations. In the end, COMPASS measurements have shown that the ion temperature fluctuations are in general non-Maxwellian with high-energy tail, which is expected to have impact on plasma-wall interaction mechanisms, such as sputtering. Measurements on COMPASS eventually agreed with previous experiments performed on ASDEX-Upgrade.

The $\mathbf{E} \times \mathbf{B}$ ion energy analyzer was sent from Prague to Padova in May 2014 and exploited in experimental campaigns featuring low-current RFP discharges during July 2014. The experiments were not successful due to technical issues, plus the measurements were also affected by a significant amount of pick-up noise. As a consequence a new $\mathbf{E} \times \mathbf{B}$ analyzer, designed specifically for RFX-mod, has been built to perform measurements at the edge of RFX-mod.

Summary and future perspectives

The work presented in this thesis has focused on the characterization of 3D effects at the plasma edge in the reversed-field pinch and tokamak configurations for the magnetic confinement of fusion plasmas in RFX-mod. The characterization of such physical properties of the edge was performed following a dual path: investigation through insertable probes and modeling through a field line tracing code. The obtained results will be synthetically described in the next paragraphs and certainly provide a further step toward a qualitative description of transport mechanisms at the edge of fusion plasmas.

In this work we have first drawn the attention on transport modifications driven by electrostatic fluctuations only, considering that these properties have not been completely addressed in present MP experiments.
The most important outcome of these studies is the understanding that at the edge transport mechanisms driven by electrostatic fluctuations are deeply affected by the application of MPs, both in the reversed-field pinch and tokamak configurations.
In both configurations we have related probe measurements to the underlying topology by using a reference frame consistent with the rotation of the applied MP. We have obtained profiles of transport properties (*electron temperature, density, radial electric field, electrostatic fluxes and diffusion coefficients*) as a function of the *helical angle* in the RFP case and of the *poloidal angle of the perturbation* in the tokamak case. The major outcome has been the identification of accumulation and reduction regions in the profiles of analyzed transport properties and their connection to the underlying topology. We have seen that macroscopic properties, as electron temperature and density, are indeed modulated by the application of MPs but we have also identified the typical transverse wave numbers for the small scale fluctuations of electrostatic particle and energy fluxes. More in detail, we have given a specific description of transport around the O- and X-point regions of the applied perturbation: independently of the magnetic coniguration and of the origin of fluctuations, transport is modulated with

an increasing close to the O-point. Transport scales are strongly reduced close to the X-point due to a reduction of fluctuations in a precise wave-vector space.
It is important to underline that our major results are independent of the adopted magnetic configuration: the modulation of transport profiles manifests itself with an increasing around the O-point and a reduction in the X-point region due to the fluctuations level and not due to the relative phase. We can therefore conclude that the physics we have described is common to both the reversed-field pinch and the tokamak configuration and involves multi-scale interactions and effects [98].
In the tokamak case, we have also compared the obtained results for the fluxes profiles as a function of frequency to analyses performed before the application of the external magnetic perturbation. The fluxes have shown a lower *outward* contribution in the same examined frequency range. It is indeed possible to deduce that transport increases also due to electrostatic fluctuations when a stochastic layer is applied and this confirms the main effects of RMPs application: RMPs modify and increase turbulent transport.

In the second part of the analyses, we have dealt with the modeling of magnetic topology through the field line tracing code FLiT when spontaneous 3D effects are present in RFX-mod in RFP configuration. The main conclusions we can draw are summarized in the following: analyses of the *averaged* $\# 99999$ discharge have evidenced the emergence of global effects after the crash event as the new diffusive structures that propagate from the core to the edge region. These structures indicate also the predominance of a transport driven by magnetic turbulence. By comparison with a real discharge we know that the *crash* event implies a complete suppression of the dominant mode's amplitude: this is not clearly visible in the *averaged* $\# 99999$.

The last part of the thesis has regarded the $\mathbf{E} \times \mathbf{B}$ ion energy analyzer and the investigations on ion temperature distribution in the scrape-off layer. Successful results have been obtained first on ASDEX-Upgrade; then, experiments were performed on the COMPASS tokamak and on RFX-mod in RFP configuration to which the author has participated. The former were found to be in agreement with AUG outcome, while experiments on RFX-mod in RFP discharges have not led to the extrapolation of an ion temperature distribution due to technical issues of the analyzer and a high amount of pick-up noise in the signals.

Open questions and future work

The outline of future work, together with few interesting open questions, is given in the following.

- ◇ Both RFP and tokamak analyses presently lack a connection with power deposition analyses on first wall. If, in the future, specific diagnostic as calorimeters or infrared cameras will be installed on RFX-mod it will be possible to connect the observed turbulent fluxes modulation to the heat flux deposited on the Plasma Facing Components.

- ◇ In RFP configuration we have chosen a set of discharges at the same shallow equilibrium. Analyses at different equilibria, in particular at deep q_a ($q_a \lesssim -0.01$), would expand our knowledge in terms of characterization of transport properties. Modifying q_a corresponds to changing the radial position of the reversal surface and has as an effect also on the radial location of the islands of the externally applied perturbation. In particular, it will be possible to distinguish the case where the $m = 0$ islands are completely detached from the first wall with respect to the analyzed case where they are intercepting the graphite tiles. Consequently, we could implement in our codes the reliable identification of the position of the *last closed flux surface* (LCFS) that would give a precise contour of the underlying topology.

- ◇ Tokamak analyses have been limited to the discussion of one discharge with a fixed set of experimental parameters. In order to obtain radial profiles of the fluxes, experiments at different radial insertions of the probe would be needed. By varying density and collisionality in a tokamak discharge we can explore different operational scenarios and their effects on transport mechanisms. Furthermore, we have seen that thanks to the MHD control system we can vary helical boundary conditions within the same discharge through a transition from $q_a < 3$ to $q_a > 3$. An interesting path to follow to continue the analyses would be the comparison of transport properties in presence of a non resonant (2, 1) magnetic perturbation (at $q_a < 2$) and in the region where $q_a > 3$.
  In tokamak configuration, the profiles of electrostatic fluxes as function of the transverse wave number have evidenced the presence of an *inward* contribution at $k_\perp > 0$, moving in the ion diamagnetic flow direction. More in detail, the *inward* contribution has been identified in the X-point distribution of both particle

and energy fluxes. This result should be the subject of further investigations in order to be fully understood.

- ◇ The possibility of having a simultaneous acquisition of current and potentials active on different rows of the *U-probe*, hence the possibility of extracting the electron density gradient, would give us information about the diamagnetic flow but also information about the shear of the electric field in relation with the underlying topology.
  Through these probe's ameliorations it would be accessible also the investigation on possible driving mechanisms for the generation of poloidal turbulent flow.

- ◇ Ion dynamics has been neglected so far, and information on electron temperature species only has been investigated. A full exploitation of $\mathbf{E} \times \mathbf{B}$ analyzer would give us information on eventual ion temperature evolution in presence of magnetic perturbations, considering that ion dynamics is foreseen to be different in presence of magnetic field due to the larger Larmor orbits.

- ◇ In both RFP and tokamak configuration we have identified which transverse wave numbers contribute to small-scale turbulence at the edge. It would be interesting to explore the link with instabilities that drive turbulent transport: in other studies, drift and interchange instabilities have been found responsible of turbulent regimes at the plasma edge. In particular, in tokamak profiles we can evince a change in the direction of propagation of fluctuations velocity, from the electron diamagnetic flow to the ion one. This implies also a connection with different instabilities that would rise and affect transport. A theoretical study would indeed be needed in order to fully understand the origins of electrostatic turbulence that drives transport at the edge in both reversed-field pinch and tokamak configuration.

- ◇ So far, we have neglected the transport contribution coming from magnetic fluctuations, the so-called *magnetic flutter*. Previous studies [99] have investigated this transport channel and the related radial energy flux at the plasma edge of the RFX experiment in reversed-field pinch configuration. Measurements were showing the increase in the radial magnetic field fluctuations inside the plasma but close to the wall the magnetic fluctuation-driven flux decreased abruptly, so that another mechanism must be responsible. These results cannot be considered as conclusive, yet. They were obtained in experiments performed on a different device and in different experimental conditions with respect to the environment

of the analyses of this thesis. The investigation on transport driven by magnetic fluctuations at the edge of RFX-mod is still an open question, considering moreover that energy transport cannot be ascribed to electrostatic turbulence only.

- ◇ $\#\ 99999$ analyses should be completed with the inclusion of ISIS signals as boundary conditions in order to evidence the fast dynamics that characterizes the reconnection events we have studied. We foresee a complete suppression of the dominant mode's amplitude when including ISIS signals in the boundary conditions for the eigenfunctions reconstruction in the *averaged* $\#\ 99999$. It should be stressed, however, that reconnection events associated to the crash in the dominant mode's amplitude are possibly 3D mechanisms which might develop in regions at least partially chaotic. Therefore, recalling the original intentions that led to the $\#\ 99999$ analyses, the definition of the separatrix of the reconnection event and the surface on which it develops might not be possible.

- ◇ A new $\mathbf{E} \times \mathbf{B}$ analyzer has been specifically designed for RFX-mod and its exploitation is foreseen in future campaigns on RFX-mod both in RFP and tokamak configurations.

Part V

Appendixes

Appendix A

Magnetohydrodynamics

Fusion plasmas consist of two charged species positively charged nuclei and negatively charged electrons, ionized apart from the nuclei and can be separated for distances comparable to the *Debye length*[1]:

$$\lambda_D = \sqrt{\frac{\epsilon_0 k_B T_e}{n_e T_e^2}} \tag{A.1}$$

The analysis of plasma's macroscopic equilibrium and stability is then based on a single-fluid model known as *MagnetoHydroDynamics*. The MHD model is a reduction of a two-fluid model derived by focusing attention on the length and time scales characteristic of macroscopic behavior. Specifically, the appropriate length scale L is the plasma radius ($L \sim a$) while the appropriate time scale τ is the ion thermal transit time across the plasma ($\tau \sim a/v_{T_i}$). This leads to a characteristic velocity $u \sim L/\tau \sim v_{T_i}$, which is the fastest macroscopic speed that the plasma can achieve the ion sound speed. The original two-fluid model describes the self-consistent behavior of a fusion plasma including all the main phenomena: macroscopic equilibrium and stability, transport, and heating and current drive and treating the plasma as consisting of an ion and electron particle's fluid. The model is a closed system of equations and presents an accurate description of most plasma phenomena except for those in which a behaviour parallel to the magnetic field is dominant. The model consists of a complicated set of coupled non-linear partial differential equations. In practice, depending upon the application under consideration, one can often make a number of further simplifications that substantially reduce its complexity, eventually leading to

[1]The Debye sheath is discussed in paragraph 3.2.1.

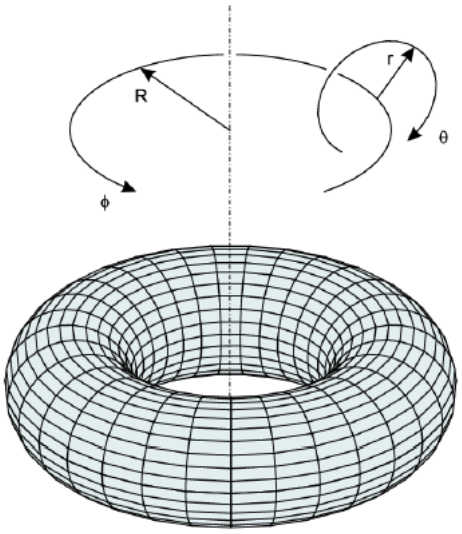

FIGURE A.1: The (r, θ, ϕ) coordinate system exploited to parametrize a toroidal device.

MHD equations:

$$\rho[\frac{\partial \mathbf{v}}{\partial t} + (\mathbf{v} \cdot \nabla)\mathbf{v}] = -\nabla p + \mathbf{j} \times \mathbf{B} + \rho\nu\nabla^2\mathbf{v} + \rho_c\mathbf{E} \quad \text{(momentum eq.)} \quad \text{(A.2)}$$

$$\frac{\partial \rho}{\partial t} + \nabla \cdot (\rho\mathbf{v}) = 0 \quad \text{(continuity eq.)} \quad \text{(A.3)}$$

$$\mathbf{E} + \mathbf{v} \times \mathbf{B} = \eta\mathbf{j} \quad \text{(Ohm's law)} \quad \text{(A.4)}$$

$$\nabla \cdot \mathbf{E} = \frac{\rho_c}{\epsilon_0} \quad \text{(Poisson's eq.)} \quad \text{(A.5)}$$

$$\frac{\partial \mathbf{B}}{\partial t} = -\nabla \times \mathbf{E} \quad \text{(Faraday's law)} \quad \text{(A.6)}$$

$$\nabla \cdot \mathbf{B} = 0 \quad \text{(solenoidality eq.)} \quad \text{(A.7)}$$

$$\mu_0\mathbf{j} = \nabla \times \mathbf{B} - \mu_0\epsilon_0\frac{\partial \mathbf{E}}{\partial t} \quad \text{(Ampere's law)} \quad \text{(A.8)}$$

ρ is the plasma mass density, ρ_c the charge density, **v** the velocity, **j** the current density, **B** the magnetic field, p the pressure, ν the viscosity, **E** the electric field and η the resistivity. In order to get a self-consistent system, the equations above have to be coupled to an equation of state for p.
The assumptions to be made are the followings:

- plasma quasi-neutrality,
- small Larmor radius approximation.

The first one allows us to discard the electric force from the momentum equation and the displacement term from Maxwell equations while the latter, $\frac{\rho_{i,e}e}{L} << 1$ corresponds

to a condition on a particle performing several gyrations before leaving the plasma.
Considering the MHD equations written above, we can see the presence of the kinematic viscosity ν and the plasma resistivity η and the ideal MHD equations can be derived from this system by simply considering a null resistivity. Ideal MHD is important to describe some unavoidable phenomena as the so-called *ideal instabilities* but η plays a fundamental role in the description of many phenomena taking place in the fusion devices, i.e. discreet relaxation events, tearing instabilities and dynamo effect.
A good estimation of the plasma resistivity η for a fully ionized plasma with ions of charge Ze is given by the *Spitzer resistivity*, formulated as:

$$\eta = \frac{\pi^{3/2} m_e^{1/2} Z e^2}{\gamma_E 2 (k_B T_e)^{3/2}} ln\Lambda \tag{A.9}$$

where γ_E is a numerical factor depending on Z and for $Z = 1$ is equal to 0.582, while $\Lambda = \frac{3}{2Ze^2}\sqrt{\frac{(k_B T_e)^3}{\pi n}}$.
When the conductivity is hypothetically infinite the plasma reaches the *ideal MHD limit*. The proximity of this limit can be parametrized by means of the *Lundquist number*:

$$S = \frac{v_A L}{\eta} \tag{A.10}$$

where $v_A = B/\sqrt{\mu_0 \rho}$ is the Alfvén velocity and L a characteristic length scale. This parameter is often replaced by the *magnetic Reynolds number*, which differs from S in the velocity term, the typical plasma speed substitutes the Alfvén one. Therefore, S characterizes an ideal plasma or a more resistive one. A fundamental property of ideal MHD is the *Alfvén freezing-in-flux theorem*, stating that the magnetic flux linked with the surface Γ that is moving together with the plasma, remains constant. In other words, the theorem states that magnetic field lines always move with the plasma, preserving the initial topological configuration in the limit of ideal MHD. If two plasma elements are connected by a field line, they will always remain connected during any plasma motions as if they were frozen into the plasma. Under this point of view, magnetic field lines can be regarded as a plastic material which can be bent and distorted by making the plasma move appropriately.
Ideal MHD deals with highly conductive plasmas ($\eta \to 0$), hence it does not account for events as magnetic reconnection of field lines. Nevertheless, magnetic reconnection bypasses the costraints of the Alfvén freezing-in-flux theorem by means of resistive dissipation: it increases as the current is localized in smaller regions, thus the ideal MHD limit is violated just in a small-scale structure with a consequent local non-ideal effect. Possible models that account for the violation of the Alfvén freezing-in-flux

theorem are briefly introduced in Section 4.1

A.1 Equilibrium and stability

Grad-Shafranov equation

Eq.(A.15) can be written also in a different form, which provides a useful analytical tool for equilibria calculation in the case or toroidal configuration. Approximating the torus as a cylinder, and thus using cylindrical coordinates (R, ϕ, Z), the axisymmetric equilibria can be described by a two-dimensional non-linear elliptic partial differential equation, called Grad-Shafranov equation (GSE). The GSE can be written as:

$$\Delta^* \psi_p = -2\pi F \frac{dF}{d\psi_p} - 2\pi\mu_0 R^2 \frac{dp}{d\psi_p} \tag{A.11}$$

where Δ^* is an elliptic operator defined as

$$\Delta^* = R\frac{\partial}{\partial R}\left(\frac{1}{R}\frac{\partial}{\partial R}\right) + \frac{\partial^2}{\partial Z^2} \tag{A.12}$$

GSE specifies the toroidal equilibrium (magnetic field and flux, current density, and pressure profiles) when the two free functions $F(\psi_p) = RB_\phi(\psi_p)$ and $p = p(\psi_p)$, i.e. the pressure, are given. Here $\psi_p(R, \phi, Z)$, the poloidal magnetic flux is used as variable, it permits to univocally label magnetic flux surfaces.
Because of the non-linearity of the Eq.(A.11), its solution generally involves numerical calculations, which use as input explicit expressions for $p = p(\psi_p)$ and $F(\psi_p)$. Note that the flux surfaces are not concentric: there is a shift of each flux surface toward external radial regions. The flux surface displacement is the result of toroidal effects: the displacement of the axis is called *Shafranov shift* [3].
The solution of GSE can be performed through asymptotic expansion considerations, including simplifications that could arise from a specific ordering of fields and pressure characteristic of a certain device. For example, using in the formulation of Eq.(A.11) the approximation of a high-β device, operating with a small safety factor, in which poloidal and toroidal magnetic field are of the same order of magnitude, and hence characterized by

$$\beta \sim 1 \qquad q \sim \frac{rB_\phi}{RB_\theta} \sim \frac{a}{R_0} < 1 \qquad \frac{B_\phi}{B_\theta} < 1 \tag{A.13}$$

the solution of GSE turns out to be the reveersed-field pinch (RFP) equilibrium. Using instead an asymptotic ordering in $\epsilon = a/R_0$ that defines an ohmically heated tokamak given by the equation below, it is possible to obtain the usial tokamak profiles and magnetic flux surfaces.

$$\beta_\phi = \frac{2\mu_0 p}{B_\phi^2} \qquad \beta_\theta = \frac{2\mu_0 p}{B_\theta^2} \qquad q \sim 1 \qquad \frac{B_\phi}{B_\theta} \sim \epsilon \tag{A.14}$$

Ideal instabilities and tearing modes

From (A.2) at the equilibrium where $\partial/\partial t = 0$ and $\mathbf{v} = 0$, the equation of force balance is obtained:

$$\nabla p = \mathbf{j} \times \mathbf{B} \tag{A.15}$$

It is important noting that pressure is constant along the magnetic field and that current density lies on the same surfaces too, since: $\mathbf{B} \cdot \nabla p$ and $\mathbf{j} \cdot \nabla p$. In presence of a toroidal geometry (Fig.(A.1)) these well defined magnetic surfaces are nested forming poloidally a set of closed curves. Some of these surfaces are called *rational surfaces* and are characterized by the fact that the magnetic field lines close upon themselves after a definite time number of transit around the machine. It is possible to introduce a parameter that effectively measures the toroidal loops needed by a field line to complete a poloidal loop, the *safety factor* $q = \Delta\phi/2\pi$, useful also to describe the stability of a toroidal configuration. In the limit of large aspect ratio ($R/a \gg 1$) of a toroidal device, it can be also written as:

$$q(r) = \frac{rB_\phi(r)}{R_0 B_\theta(r)} \tag{A.16}$$

where r is the radial coordinate, R_0 is the major radius of the torus, B_ϕ and B_θ the toroidal and poloidal component of the magnetic field. In RFP q is typically $a/(2R)$ in the centre and decreases towards a negative value at the edge. Whereas in a Tokamak discharge q is typically close to one in the centre and goes beyond two as long as r approaches the edge. Both these trends can be seen in Figure 1.7.

In the MHD framework any perturbation $\tilde{\mathbf{B}}$ of a quantity $\mathbf{B}$ in a toroidal plasma is usually Fourier analyzed and the decomposition of the perturbations present upon

the equilibrium is:

$$\tilde{\mathbf{B}}(\mathbf{r}) = \sum_{\mathbf{k}} \tilde{\mathbf{B}}_{\mathbf{k}}(r) e^{i(\mathbf{k}\cdot\mathbf{r}-\omega t)} = \sum_{\mathbf{k}} \tilde{\mathbf{B}}_{\mathbf{k}}(r) e^{i(m\theta+n\phi-\omega t)} \tag{A.17}$$

with, *m* and *n* the poloidal and toroidal mode number. Each couple of $(m\ ,n)$ values represents a helical perturbation or mode. The angular frequency ω is a complex quantity $\omega = \omega_R + i\omega_I$, of which the real part describes the propagation velocity, while the imaginary part represents an exponential growth, if $\omega_I > 0$, or damping of the perturbation amplitude, if $\omega_I < 0$.

It can be promptly seen that the resonance condition: $q = -m/n$ corresponds to the situation in which the magnetic perturbation and the field lines have the same pitch. This means: $\mathbf{k} \cdot \mathbf{B}_0 = 0$, where $\mathbf{B}_0$ is the equilibrium field and **k** is the wave vector. This is where MHD instabilities can develop and grow at radial position r_{res}, *resonant surfaces*, where the safety factor assumes rational values. Any perturbation that deforms $\mathbf{B}_0$ field lines will increase the magnetic energy.

Ideal instabilities (those appearing not considering the resistivity η in the model) can be driven by two main factors: a term proportional to $\nabla p \sim \mathbf{j}_\perp \times \mathbf{B}$ and a term proportional to the parallel current $j_\parallel$. These are sources of free energy used for the growth of the instability, leading respectively to *pressure driven* and *current driven* modes. Ideal modes are present both in tokamak and RFP magnetic configurations but can usually be stabilised by different means. In a tokamak device, the combination of a monotonically growing q profile together with the value at the axis, $q(0) > 1$, helps stabilise the configuration (not taking into account toroidicity). In a RFP device, these modes are damped by means of flux conserver that surrounds the torus: the characteristic penetration time of the conserver is high enough to avoid plasma deformations induced by instabilities.

When taking into account resistivity, another family of instabilities can grow. Starting from resistive MHD equations, it is possible to show that the radial component for the magnetic field can set up:

$$\gamma \tilde{b}_r = i\mathbf{k} \cdot \mathbf{B}_0 + \tilde{u}_r + \frac{\eta}{\mu_0}\left(\frac{d^2\tilde{b}_r}{dr^2} - k^2\tilde{b}_r\right) \tag{A.18}$$

where $\mathbf{k}$ is the wave vector that can assume only discrete values,i.e. $k_\phi = n/R_0$ and $k_\theta = m/a$.

The main effect of resistivity is that magnetic field lines tear and reconnect during their evolution, see Figure A.2. The magnetic configuration is sheared, i.e. its radial

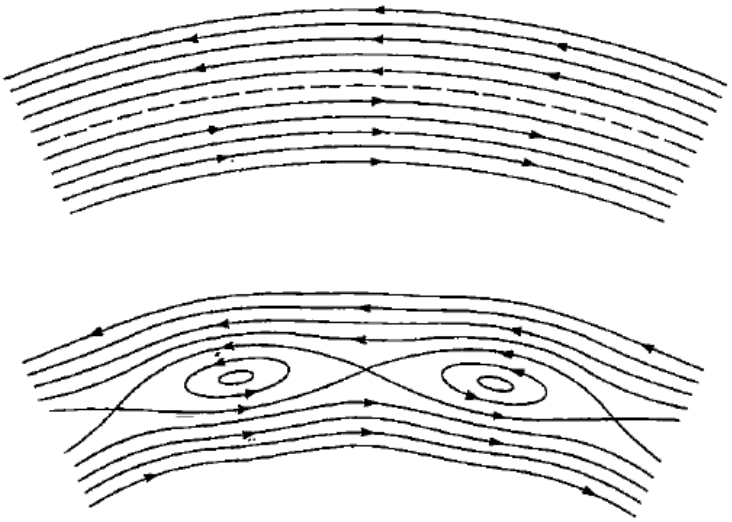

FIGURE A.2: Reconnection of magnetic field producing magnetic islands.

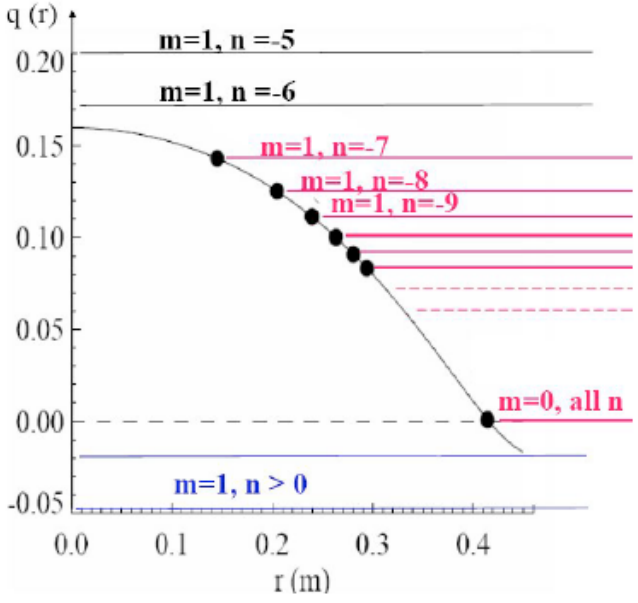

FIGURE A.3: Possible global MHD instabilities in RFX-mod. This sketch is taken from [85].

component varies in space due to a current profile with a gradient localized where the θ component of the magnetic field field changes its sign. When this gradient is sufficiently high, a tearing instability is triggered, which causes the magnetic field lines to bend and reconnect, changing the topology as represented in the figure. The resultant magnetic configuration is characterized by the presence of a so called *magnetic island*.

At low plasma current, a wide spectrum of tearing modes is present in RFP devices in regimes called Multiple Helicity. The largest tearing modes are mostly in the $m = 1$ and $m = 0$ MHD spectra.

In Figure A.3 possible kink modes in a RFP are superimposed on the typical RFX-mod safety factor profile. There are several resonances for modes having $m = 1$ and $-\infty > n > -7$, each of these resonances is linked to an unstable mode the most internal ($n = -7$) being also the most unstable. In the real device operation all of these modes grow to a saturated level, producing a large magnetic chaos, large plasma-wall interaction and poor confinement into the plasma core. We redirect to Section 2.3 for a complete detailed description of the implications of MH regime and the transition to QSH/SH regimes.

Also non-resonant modes are usually present in RFPs, one branch has $m = 1$ and negative n values, i.e. the same winding direction as resonant modes inside the toroidal field reversal surface; the other has positive n, and the same winding direction as modes resonant outside the reversal surface. In presence of a resistive wall surrounding the plasma the former are called Internal Resistive Wall Modes (IRWMs), while the latter are called External Resistive Wall Modes (ERWMs). One of the two branches is usually unstable and the other stable, but which of the two depends on plasma equilibrium.

Appendix B

Transport equations

B.1 Vlasov equation

By choosing a perturbative approach, it is possible to write every physical entity as a composition of its mean value plus the fluctuating part. For example, the electric field can be written as:

$$\mathbf{E}(r) =< \mathbf{E}(r) > +\tilde{\mathbf{E}} \tag{B.1}$$

where $< \cdots >$ stands for an average over temporal evolution and r represents a generic spatial dimension. Using the system of coordinates (r,θ,ϕ), the *Vlasov equation* [70] will be:

$$\frac{\partial F}{\partial t} + \mathbf{v} \cdot \nabla F + \frac{q}{m}(\mathbf{E} + \mathbf{v} \times \mathbf{B}) \cdot \nabla_{\mathbf{v}} F = 0 \tag{B.2}$$

Applying a time averaging and considering that the distribution function F is a function of just the variable r, then:

$$\frac{\partial < F >}{\partial t} + v_r \frac{\partial < F >}{\partial r} + \frac{q}{m}(< \mathbf{E} > + \mathbf{v} \times < \mathbf{B} >) \cdot \nabla_{\mathbf{v}} < F > + \frac{q}{m}\left[\left\langle \tilde{\mathbf{E}} \cdot \frac{\partial \tilde{F}}{\partial \mathbf{v}} \right\rangle\right] = 0 \tag{B.3}$$

If we use the definition:

$$(\mathbf{v} \times \mathbf{B}) \frac{\partial < F >}{\partial \mathbf{v}} = \frac{\partial}{\partial \mathbf{v}} \cdot [(\mathbf{v} \times < \mathbf{B} >) < F >] \tag{B.4}$$

in the end we obtain:

$$\frac{\partial < F >}{\partial t}+\frac{\partial}{\partial x}(v_x < F >)+\frac{q}{m}\nabla_{\mathbf{v}}\cdot[(< \mathbf{E} > +\mathbf{v}\times < \mathbf{B} >) < F >]+\frac{q}{m}\nabla_{\mathbf{v}}\cdot\left[\left\langle \tilde{\mathbf{E}}\tilde{F}\right\rangle\right] = 0 \tag{B.5}$$

In order to obtain the moments of Equation B.2 we should introduce the moments of the distribution function F:

- the particle density and its fluctuation:

$$n = \int < F > d_3v \qquad \tilde{n} = \int \tilde{F} d_3v \tag{B.6}$$

- and accordingly the temperature and its fluctuation, linked to pressure and density by:

$$T =< p > /n \qquad \tilde{T} = \frac{1}{n}(\tilde{p} - \tilde{n}T) \tag{B.7}$$

- the particle flux and its fluctuation:

$$\mathbf{\Gamma} = \int \mathbf{v} < F > d_3v \qquad \tilde{\Gamma} = \int \mathbf{v}\tilde{F} d_3v \tag{B.8}$$

- the energy flux and its fluctuation:

$$\mathbf{Q} = \int \frac{1}{2}mv^2\mathbf{v} < F > d_3v \qquad \tilde{Q} = \int \frac{1}{2}mv^2\mathbf{v}\tilde{F} d_3v \tag{B.9}$$

B.1.1 Continuity equation

The zeroth-order momentum of the Vlasov equation gives us the *continuity equation* under the form:

$$\frac{\partial n}{\partial t} + \frac{\partial \Gamma_r}{\partial r} = 0 \tag{B.10}$$

By using a fluid approximation, defining an *ad hoc* mass density in a *quasi-neutrality* condition ($n_{ion} \approx n_{el} \approx n$):

$$\rho = n_i m_i + n_e m_e \approx n(m_i + m_e) \tag{B.11}$$

we would have obtained the continuity equation in the form:

$$\frac{\partial \rho}{\partial t} + \nabla \cdot \rho\mathbf{v} = 0 \tag{B.12}$$

B.2 Particle and energy flux

The first-order momentum of Equation B.2 can be re-written as (cit):

$$\frac{\partial \Gamma}{\partial t} + \frac{\partial}{\partial r}\int v_r \mathbf{v} < F > d_3 v - \frac{q}{m}(< \mathbf{E} > n + \Gamma \times < \mathbf{B} >) - \frac{q}{m} < \tilde{\mathbf{E}}\tilde{n} >= 0 \quad \text{(B.13)}$$

Assuming that the magnetic field is mainly poloidal, true at the edge of a reversed-field pinch configuration, so $\mathbf{B} = B_\theta$, the calculation for the particle flux will involve only the radial component of it and if we want to re-write Equation B.13 then:

$$(\Gamma \times < \mathbf{B} >)_\phi = -\Gamma_r B_\theta \quad \text{(B.14)}$$

Now, if we consider only the toroidal component of Equation B.13 we obtain:

$$\frac{\partial \Gamma_\phi}{\partial t} + \frac{\partial}{\partial r}\int v_r v_\phi < F > d_3 v + \frac{q}{m}\Gamma_r B_\theta - \frac{q}{m} < E_\phi > n - \frac{q}{m} < \tilde{E}_\phi \tilde{n} >= 0 \quad \text{(B.15)}$$

Defining τ as the time scale for the variation of the perturbation and recalling the definition of cyclotron frequency $\omega_c = qB/m$, we can adopt some approximation and deduce:

$$\frac{\partial}{\partial t} v_\phi < F > \sim \frac{v_\phi < F >}{\tau}; \qquad \frac{q}{m} < F > \mathbf{v} \times < \mathbf{B} > \sim v < F > \omega_c \quad \text{(B.16)}$$

We experimentally observe that typical frequencies for the variation of the perturbation satisfy the condition $\omega_c \gg 1/\tau$ so that it is possible not taking into account the first term of Equation B.15. Similarly, if L is the typical scale length of the variation of perturbation, the following approximations stand:

$$\frac{\partial}{\partial r} v_r v_\phi < F > \sim \frac{v^2 < F >}{L}; \qquad \frac{q}{m} < F > \mathbf{v} \times < \mathbf{B} > \sim \frac{v^2 < F >}{\rho_L} \quad \text{(B.17)}$$

where ρ_L is the Larmor radius. Considering $\rho_L \ll L$ we can neglect also the second term in Equation B.15. In the end we can obtain the contribution to the flux deriving only from the fluctuating terms:

$$\Gamma_r = \frac{< \tilde{E}_\phi \tilde{n} >}{B_\theta} \quad \text{(B.18)}$$

In order to obtain the radial component of the energy flux as the effect of turbulent mechanisms, we should evaluate the third-order momentum of Equation B.2 and by

using the same approximations $\omega_c \gg 1/\tau$ and $\rho_L \ll L$, supposing isotropic pressure fluctuations and neglecting the contributions not coming from turbulent transport, we obtain (cit):

$$Q_r = \frac{3}{2}\frac{< \tilde{E}_\phi \tilde{p} >}{B_\theta} \tag{B.19}$$

Tokamaks and RFPs as plasma confinement systems are conceived in their idealized form as symmetrical about the major axis and possessing a set of nested magnetic surfaces. The plasma equilibrium satisfies this set of equations:

$$\nabla \cdot \mathbf{B} = 0, \qquad \nabla \times \mathbf{B} = 4\pi \mathbf{j}, \qquad \mathbf{j} \times \mathbf{B} = \nabla p, \qquad \mathbf{B} \cdot \mathbf{n} = 0 \tag{B.20}$$

where **n** is the normal to the magnetic field. This equilibrium is topologically toroidal . The existence of magnetic surface can only be proved theoretically for a system with complete symmetry. Departure from symmetry may cause several different effects on the topology of the nested surfaces, such as their distortion or destruction. These changes can lead to increased particle and energy transport perpendicular to the mean magnetic field. If magnetic surfaces do not strictly exists then there will be a component of magnetic field in the direction of the equilibrium density and temperature gradient. The importance of these components may be emphasized by noting that the classical electron thermal conductivity χ parallel and perpendicular to the magnetic field are in the approximate ratio :

$$\frac{\chi_\parallel}{\chi_\perp} \simeq \omega_c^2 \tau_c^2 \tag{B.21}$$

where ω_c is the electron cyclotron frequency defined ($\omega_c = eB/m$) and τ_c the collision time. For typical tokamak parameters ($T_e = 1\ keV$, $n = 5 \cdot 10^{19}\ m^{-3}$ and $B \sim 1\ T$) this ratio is 10^{13}.

Classical theory on particle and energy transport based on inter-particle collision does not explain the rate of transport observed in toroidally confined plasmas as tokamaks and RFPs which is typically one or two orders of magnitude higher. This phenomenon known as **anomalous transport** is still an unanswered question and represents one of the main obstacle to the achievement of fusion energy.

Bibliography

[1] O. A. Hurricane, D. A. Callahan, D. T. Casey, P. M. Celliers, C. Cerjan, E. L. Dewald, T. R. Dittrich, T. Doppner, D. E. Hinkel, L. F. Berzak Hopkins, J. L. Kline, S. Le Pape, T. Ma, A. G. MacPhee, J. L. Milovich, A. Pak, H. S. Park, P. K. Patel, B. A. Remington, J. D. Salmonson, P. T. Springer, and R. Tommasini. Fuel gain exceeding unity in an inertially confined fusion implosion. *Nature*, 506 (7488):343–348, 02 2014. URL http://dx.doi.org/10.1038/nature13008.

[2] Jeffrey P. Freidberg. *Plasma Physics and Fusion Energy*. Cambridge University Press, 2008.

[3] J. Wesson. *Tokamaks*. Clarendon Press, Oxford, 2004.

[4] C. Pérez von Thun. *MHD analysis of edge instabilities in the JET tokamak*. PhD thesis, 2004.

[5] Eric Nardon. *Edge Localized Modes control by Resonant Magnetic Perturbations*. PhD thesis, 2007.

[6] P.C. Stangeby. *The plasma boundary of magnetic fusion devices*. Plasma Physics Series, Institute of Physics Publishing, Bristol, 2000.

[7] P. Sonato, G. Chitarin, P. Zaccaria, F. Gnesotto, S. Ortolani, A. Buffa, M. Bagatin, W.R. Baker, S. Dal Bello, P. Fiorentin, L. Grando, G. Marchiori, D. Marcuzzi, A. Masiello, S. Peruzzo, N. Pomaro, and G. Serianni. Machine modification for active MHD control in RFX. *Fusion Engineering and Design*, 66–68(0):161 – 168, 2003. ISSN 0920-3796. doi: http://dx.doi.org/10.1016/S0920-3796(03)00177-7. URL http://www.sciencedirect.com/science/article/pii/S0920379603001777. 22nd Symposium on Fusion Technology.

[8] P. Piovesan, M. Zuin, A. Alfier, D. Bonfiglio, F. Bonomo, A. Canton, S. Cappello, L. Carraro, R. Cavazzana, M. Gobbin, L. Marrelli, E. Martines, R. Lorenzini,

R. Pasqualotto, M. Spolaore, M. Valisa, N. Vianello, and P. Zanca. Magnetic order improvement through high current and MHD feedback control in RFX-mod. *35th EPS Conference on Plasma Physics*, 32D, 2008.

[9] Paolo Zanca, Lionello Marrelli, Gabriele Manduchi, and Giuseppe Marchiori. Beyond the intelligent shell concept: the clean–mode–control. *Nuclear Fusion*, 47 (11):1425, 2007. URL http://stacks.iop.org/0029-5515/47/i=11/a=004.

[10] L Marrelli, P Zanca, M Valisa, G Marchiori, A Alfier, F Bonomo, M Gobbin, P Piovesan, D Terranova, M Agostini, C Alessi, V Antoni, L Apolloni, F Auriemma, O Barana, P Bettini, T Bolzonella, D Bonfiglio, M Brombin, A Buffa, A Canton, S Cappello, L Carraro, R Cavazzana, M Cavinato, G Chitarin, S Dal Bello, A De Lorenzi, D F Escande, A Fassina, P Franz, G Gadani, E Gaio, E Gazza, L Giudicotti, F Gnesotto, L Grando, S C Guo, P Innocente, R Lorenzini, A Luchetta, G Malesani, G Manduchi, D Marcuzzi, P Martin, S Martini, E Martines, A Masiello, F Milani, M Moresco, A Murari, L Novello, S Ortolani, R Paccagnella, R Pasqualotto, S Peruzzo, R Piovan, A Pizzimenti, N Pomaro, I Predebon, M E Puiatti, G Rostagni, F Sattin, P Scarin, G Serianni, P Sonato, E Spada, A Soppelsa, G Spizzo, M Spolaore, C Taccon, C Taliercio, V Toigo, N Vianello, P Zaccaria, B Zaniol, L Zanotto, E Zilli, G Zollino, and M Zuin. Magnetic self organization, MHD active control and confinement in RFX–mod. *Plasma Physics and Controlled Fusion*, 49(12B):B359, 2007. URL http://stacks.iop.org/0741-3335/49/i=12B/a=S33.

[11] R. Cavazzana O. Kudlacek G. Manduchi L. Marrelli F. Villone P. Zanca L. Zanotto A. Cenedese P. Merlo G. Marchiori, C. Finotti. Model based feedback control system of plasma shape in RFX–mod Tokamak discharges. *41st EPS Conference on Plasma Physics*, 2014.

[12] Paolo Zanca and David Terranova. Reconstruction of the magnetic perturbation in a toroidal reversed field pinch. *Plasma Physics and Controlled Fusion*, 46(7): 1115, 2004. URL http://stacks.iop.org/0741-3335/46/i=7/a=011.

[13] K. Moffatt. *Magnetic field generation in electrically conducting fluids*. Monograph in CUP series on Mechanics and Applied Mathematics, 1978.

[14] L. Woltjer. A theorem on force–free magnetic fields. *Proceedings of the National Academy of Sciences of the United States of America*, 44(6):489, 1958.

[15] J. B. Taylor. Relaxation of toroidal plasma and generation of reverse magnetic fields. *Phys. Rev. Lett.*, 33:1139–1141, Nov 1974. doi: 10.1103/PhysRevLett.33.1139. URL http://link.aps.org/doi/10.1103/PhysRevLett.33.1139.

[16] J. B. Taylor. Relaxation and magnetic reconnection in plasmas. *Rev. Mod. Phys.*, 58:741–763, Jul 1986. doi: 10.1103/RevModPhys.58.741. URL http://link.aps.org/doi/10.1103/RevModPhys.58.741.

[17] D F Escande, S Cappello, F D'Angelo, P Martin, S Ortolani, and R Paccagnella. Single helicity: a new paradigm for the reversed field pinch. *Plasma Physics and Controlled Fusion*, 42(12B):B243, 2000. URL http://stacks.iop.org/0741-3335/42/i=12B/a=319.

[18] S Cappello and R Paccagnella. Nonlinear plasma evolution and sustainment in the reversed field pinch. *Phys. Fluids*, B(4):611, 1992. URL http://dx.doi.org/10.1063/1.860471.

[19] S Cappello. Bifurcation in the MHD behaviour of a self-organizing system: the reversed field pinch (RFP). *Plasma Physics and Controlled Fusion*, 46(12B):B313, 2004. URL http://stacks.iop.org/0741-3335/46/i=12B/a=027.

[20] S. Cappello and D. F. Escande. Bifurcation in Viscoresistive MHD: The Hartmann Number and the Reversed Field Pinch. *Phys. Rev. Lett.*, 85:3838–3841, Oct 2000. doi: 10.1103/PhysRevLett.85.3838. URL http://link.aps.org/doi/10.1103/PhysRevLett.85.3838.

[21] R. Lorenzini, E. Martines, P. Piovesan, D. Terranova, P. Zanca, M. Zuin, A. Alfier, D. Bonfiglio, F. Bonomo, A. Canton, S. Cappello, L. Carraro, R. Cavazzana, D. F. Escande, A. Fassina, P. Franz, M. Gobbin, P. Innocente, L. Marrelli, R. Pasqualotto, M. E. Puiatti, M. Spolaore, M. Valisa, N. Vianello, and P. Martin. Self-organized helical equilibria as a new paradigm for ohmically heated fusion plasmas. *Nat Phys*, 5(8):570–574, 08 2009. URL http://dx.doi.org/10.1038/nphys1308.

[22] Barbara Momo. *Investigation of the magnetic topology of helical RFP plasmas*. PhD thesis, 2012.

[23] Marco Veranda. *3D nonlinear magnetohydrodynamics of fusion plasmas: helical regimes and magnetic topology*. PhD thesis, 2013.

[24] M.E. Puiatti, M. Valisa, M. Agostini, F. Auriemma, F. Bonomo, L. Carraro, A. Fassina, M. Gobbin, R. Lorenzini, B. Momo, A. Scaggion, B. Zaniol, A. Alfier, L. Apolloni, M. Baruzzo, T. Bolzonella, D. Bonfiglio, A. Canton, S. Cappello, R. Cavazzana, S. Dal Bello, G. De Masi, D.F. Escande, P. Franz, E. Gazza, S. Guo, P. Innocente, G. Marchiori, L. Marrelli, P. Martin, E. Martines, S. Martini, S. Menmuir, L. Novello, R. Paccagnella, P. Piovesan, L. Piron, I. Predebon, A. Ruzzon, F. Sattin, P. Scarin, A. Soppelsa, G. Spizzo, S. Spagnolo, M. Spolaore, D. Terranova, M. Veranda, N. Vianello, P. Zanca, L. Zanotto, and M. Zuin. Internal and external electron transport barriers in the RFX–mod reversed field pinch. *Nuclear Fusion*, 51(7):073038, 2011. URL http://stacks.iop.org/0029-5515/51/i=7/a=073038.

[25] P. Martin, J. Adamek, P. Agostinetti, M. Agostini, A. Alfier, C. Angioni, V. Antoni, L. Apolloni, F. Auriemma, O. Barana, S. Barison, M. Baruzzo, P. Bettini, M. Boldrin, T. Bolzonella, D. Bonfiglio, F. Bonomo, A.H. Boozer, M. Brombin, J. Brotankova, A. Buffa, A. Canton, S. Cappello, L. Carraro, R. Cavazzana, M. Cavinato, L. Chacon, G. Chitarin, W.A. Cooper, S. Dal Bello, M. Dalla Palma, R. Delogu, A. De Lorenzi, G. De Masi, J.Q. Dong, M. Drevlak, D.F. Escande, F. Fantini, A. Fassina, F. Fellin, A. Ferro, S. Fiameni, A. Fiorentin, P. Franz, E. Gaio, X. Garbet, E. Gazza, L. Giudicotti, F. Gnesotto, M. Gobbin, L. Grando, S.C. Guo, Y. Hirano, S.P. Hirshman, S. Ide, V. Igochine, Y. In, P. Innocente, S. Kiyama, S.F. Liu, Y.Q. Liu, D. Lòpez Bruna, R. Lorenzini, A. Luchetta, G. Manduchi, D.K. Mansfield, G. Marchiori, D. Marcuzzi, L. Marrelli, S. Martini, G. Matsunaga, E. Martines, G. Mazzitelli, K. McCollam, S. Menmuir, F. Milani, B. Momo, M. Moresco, S. Munaretto, L. Novello, M. Okabayashi, S. Ortolani, R. Paccagnella, R. Pasqualotto, M. Pavei, G.V. Perverezev, S. Peruzzo, R. Piovan, P. Piovesan, L. Piron, A. Pizzimenti, N. Pomaro, N. Pomphrey, I. Predebon, M.E. Puiatti, V. Rigato, A. Rizzolo, G. Rostagni, G. Rubinacci, A. Ruzzon, H. Sakakita, R. Sanchez, J.S. Sarff, F. Sattin, A. Scaggion, P. Scarin, W. Schneider, G. Serianni, P. Sonato, E. Spada, A. Soppelsa, S. Spagnolo, M. Spolaore, D.A. Spong, G. Spizzo, M. Takechi, C. Taliercio, D. Terranova, V. Toigo, M. Valisa, M. Veranda, N. Vianello, F. Villone, Z. Wang, R.B. White, D. Yadikin, P. Zaccaria, A. Zamengo, P. Zanca, B. Zaniol, L. Zanotto, E. Zilli, G. Zollino, and M. Zuin. Overview of the RFX fusion science program. *Nuclear Fusion*, 51(9):094023, 2011. URL http://stacks.iop.org/0029-5515/51/i=9/a=094023.

[26] H.Y.W. Tsui, C.P. Ritz, G. Miller, J.C. Ingraham, C.P. Munson, K.F. Schoenberg, and P.G. Weber. Fluctuations and transport in a reversed field pinch edge plasma. *Nuclear Fusion*, 31(12):2371, 1991. URL http://stacks.iop.org/0029-5515/31/i=12/a=009.

[27] V. Antoni, R. Cavazzana, D. Desideri, E. Martines, G. Serianni, and L. Tramontin. Electrostatic turbulence and transport in the velocity shear layer of a Reversed Field Pinch plasma. *Phys. Rev. Lett.*, 80:4185–4188, May 1998. doi: 10.1103/PhysRevLett.80.4185. URL http://link.aps.org/doi/10.1103/PhysRevLett.80.4185.

[28] A Möller. Edge resonant fluctuations and particle transport in a reversed–field pinch. *Physics of Plasmas*, 5:4321, 1998. URL http://dx.doi.org/10.1063/1.873170.

[29] E. Martines, V. Antoni, D. Desideri, G. Serianni, and L. Tramontin. Energy flux driven by electrostatic turbulence in the RFX edge plasma. *Nuclear Fusion*, 39 (5):581, 1999. URL http://stacks.iop.org/0029-5515/39/i=5/a=302.

[30] G. Spizzo, N. Vianello, R. B. White, S. S. Abdullaev, M. Agostini, R. Cavazzana, G. Ciaccio, M. E. Puiatti, P. Scarin, O. Schmitz, M. Spolaore, D. Terranova, RFX, and TEXTOR Teams. Edge ambipolar potential in toroidal fusion plasmas. *Physics of Plasmas (1994-present)*, 21(5):056102, 2014. doi: http://dx.doi.org/10.1063/1.4872173. URL http://scitation.aip.org/content/aip/journal/pop/21/5/10.1063/1.4872173.

[31] E. Martines, R. Lorenzini, B. Momo, S. Munaretto, P. Innocente, and M. Spolaore. The plasma boundary in single helical axis RFP plasmas. *Nuclear Fusion*, 50(3): 035014, 2010. URL http://stacks.iop.org/0029-5515/50/i=3/a=035014.

[32] P. Zanca, E. Martines, T. Bolzonella, S. Cappello, S. C. Guo, P. Martin, S. Martini, S. Ortolani, R. Paccagnella, D. Terranova, and M. Viterbo. Analysis of phase locking of tearing modes in reversed field pinch plasmas. *Physics of Plasmas*, 8: 516, 2001. URL http://dx.doi.org/10.1063/1.1339835.

[33] Richard Fitzpatrick and Paolo Zanca. Phase-locking of tearing modes in the reversed field experiment. *Physics of Plasmas*, 9:2707, 2002. URL http://dx.doi.org/10.1063/1.1481057.

[34] P. Innocente, R. Lorenzini, D. Terranova, and P. Zanca. FLiT: A field line trace code for magnetic confinement devices. Submitted to Comput. Phys. Commun., 2015.

[35] P. Scarin, N. Vianello, M. Agostini, G. Spizzo, M. Spolaore, M. Zuin, S. Cappello, L. Carraro, R. Cavazzana, G. De Masi, E. Martines, M. Moresco, S. Munaretto, M. E. Puiatti, M. Valisa, and the RFX-mod Team. Topology and transport in the edge region of RFX–mod helical regimes. *Nuclear Fusion*, 51(7):073002, 2011. URL http://stacks.iop.org/0029-5515/51/i=7/a=073002.

[36] Gianluca Spizzo, Paolo Scarin, Matteo Agostini, Alberto Alfier, Fulvio Auriemma, Daniele Bonfiglio, Susanna Cappello, Alessandro Fassina, Paolo Franz, Lidia Piron, Paolo Piovesan, Maria Ester Puiatti, Marco Valisa, and Nicola Vianello. Investigation on the relation between edge radial electric field asymmetries in RFX–mod and density limit. *Plasma Physics and Controlled Fusion*, 52(9):095011, 2010. URL http://stacks.iop.org/0741-3335/52/i=9/a=095011.

[37] Allen H. Boozer. Plasma equilibrium with rational magnetic surfaces. *Phys. Fluids*, 24:1999, 1981. URL http://dx.doi.org/10.1063/1.863297.

[38] John M. Finn, Rick Nebel, and Charles Bathke. Single and multiple helicity Ohmic states in reversed-field pinches. *Phys. Fluids B*, 4:1262, 1992. URL http://dx.doi.org/10.1063/1.860082.

[39] R.B. White. *The Theory of Toroidally Confined Plasmas 2nd edition*. (London: Imperial College Pres, 2006.

[40] E Martines, R Lorenzini, B Momo, D Terranova, P Zanca, A Alfier, F Bonomo, A Canton, A Fassina, P Franz, and P Innocente. Equilibrium reconstruction for single helical axis reversed field pinch plasmas. *Plasma Physics and Controlled Fusion*, 53(3):035015, 2011. URL http://stacks.iop.org/0741-3335/53/i=3/a=035015.

[41] B Momo, E Martines, D F Escande, and M Gobbin. Magnetic coordinate systems for helical SHAx states in reverse field pinch plasmas. *Plasma Physics and Controlled Fusion*, 53(12):125004, 2011. URL http://stacks.iop.org/0741-3335/53/i=12/a=125004.

[42] F. Wagner, G. Becker, K. Behringer, D. Campbell, A. Eberhagen, W. Engelhardt, G. Fussmann, O. Gehre, J. Gernhardt, G. v. Gierke, G. Haas, M. Huang, F. Karger,

M. Keilhacker, O. Klüber, M. Kornherr, K. Lackner, G. Lisitano, G. G. Lister, H. M. Mayer, D. Meisel, E. R. Müller, H. Murmann, H. Niedermeyer, W. Poschenrieder, H. Rapp, H. Röhr, F. Schneider, G. Siller, E. Speth, A. Stäbler, K. H. Steuer, G. Venus, O. Vollmer, and Z. Yü. Regime of improved confinement and high beta in neutral–beam–heated divertor discharges of the ASDEX tokamak. *Phys. Rev. Lett.*, 49:1408–1412, Nov 1982. doi: 10.1103/PhysRevLett.49.1408. URL http://link.aps.org/doi/10.1103/PhysRevLett.49.1408.

[43] H Zohm. Edge localized modes (ELMs). *Plasma Physics and Controlled Fusion*, 38(2):105, 1996. URL http://stacks.iop.org/0741-3335/38/i=2/a=001.

[44] J W Connor. Edge–localized modes – physics and theory. *Plasma Physics and Controlled Fusion*, 40(5):531, 1998. URL http://stacks.iop.org/0741-3335/40/i=5/a=002.

[45] W Suttrop. The physics of large and small edge localized modes. *Plasma Physics and Controlled Fusion*, 42(5A):A1, 2000. URL http://stacks.iop.org/0741-3335/42/i=5A/a=301.

[46] M Bécoulet, G Huysmans, Y Sarazin, X Garbet, Ph Ghendrih, F Rimini, E Joffrin, X Litaudon, P Monier-Garbet, J-M Ané, P Thomas, A Grosman, V Parail, H Wilson, P Lomas, P deVries, K-D Zastrow, G F Matthews, J Lonnroth, S Gerasimov, S Sharapov, M Gryaznevich, G Counsell, A Kirk, M Valovic, R Buttery, A Loarte, G Saibene, R Sartori, A Leonard, P Snyder, L L Lao, P Gohil, T E Evans, R A Moyer, Y Kamada, A Chankin, N Oyama, T Hatae, N Asakura, O Tudisco, E Giovannozzi, F Crisanti, C P Perez, H R Koslowski, T Eich, A Sips, L Horton, A Hermann, P Lang, J Stober, W Suttrop, P Beyer, S Saarelma, and Contributors to JET-EFDA Workprogramme. Edge localized mode physics and operational aspects in tokamaks. *Plasma Physics and Controlled Fusion*, 45(12A):A93, 2003. URL http://stacks.iop.org/0741-3335/45/i=12A/a=007.

[47] G T A Huysmans. ELMs: MHD instabilities at the transport barrier. *Plasma Physics and Controlled Fusion*, 47(12B):B165, 2005. URL http://stacks.iop.org/0741-3335/47/i=12B/a=S13.

[48] M.E. Fenstermacher, T.E. Evans, T.H. Osborne, M.J. Schaffer, J.S. deGrassie, P. Gohil, R.A. Moyer, and the DIII-D Team. Suppression of type–I ELMs using a single toroidal row of magnetic field perturbation coils in DIII–D. *Nuclear Fusion*, 48(12):122001, 2008. URL http://stacks.iop.org/0029-5515/48/i=12/a=122001.

[49] M Lehnen, S Abdullaev, W Biel, M F M de Bock, S Brezinsek, C Busch, I Classen, K H Finken, M von Hellermann, S Jachmich, M Jakubowski, R Jaspers, H R Koslowski, A Krämer-Flecken, Y Kikuchi, Y Liang, A Nicolai, A Pospieszczyk, T Van Rompuy, U Samm, O Schmitz, G Sergienko, B Unterberg, R Wolf, O Zimmermann, and the TEXTOR team. Transport and divertor properties of the dynamic ergodic divertor. *Plasma Physics and Controlled Fusion*, 47(12B):B237, 2005. URL http://stacks.iop.org/0741-3335/47/i=12B/a=S18.

[50] Ph Ghendrih, A Grosman, and H Capes. Theoretical and experimental investigations of stochastic boundaries in tokamaks. *Plasma Physics and Controlled Fusion*, 38(10):1653, 1996. URL http://stacks.iop.org/0741-3335/38/i=10/a=002.

[51] A. B. Rechester and M. N. Rosenbluth. Electron heat transport in a tokamak with destroyed magnetic surfaces. *Phys. Rev. Lett.*, 40:38–41, Jan 1978. doi: 10.1103/PhysRevLett.40.38. URL http://link.aps.org/doi/10.1103/PhysRevLett.40.38.

[52] J. C. Vallet, L. Poutchy, M. S. Mohamed-Benkadda, D. Edery, E. Joffrin, P. Lecoustey, A. L. Pecquet, A. Samain, and M. Talvard. Stabilization of tokamak Ohmic discharges at the density limit by means of the ergodic divertor. *Phys. Rev. Lett.*, 67:2662–2665, Nov 1991. doi: 10.1103/PhysRevLett.67.2662. URL http://link.aps.org/doi/10.1103/PhysRevLett.67.2662.

[53] A. W. Leonard. Edge-localized-modes in tokamaks. *Physics of Plasmas (1994-present)*, 21(9):090501, 2014. doi: http://dx.doi.org/10.1063/1.4894742. URL http://scitation.aip.org/content/aip/journal/pop/21/9/10.1063/1.4894742.

[54] O. Schmitz, M.W. Jakubowski, H. Frerichs, D. Harting, M. Lehnen, B. Unterberg, S.S. Abduallaev, S. Brezinsek, I. Classen, T. Evans, Y. Feng, K.H. Finken, M. Kantor, D. Reiter, U. Samm, B. Schweer, G. Sergienko, G.W. Spakman, M. Tokar, E. Uzgel, R.C. Wolf, and the TEXTOR Team. Identification and analysis of transport domains in the stochastic boundary of TEXTOR–DED for different mode spectra. *Nuclear Fusion*, 48(2):024009, 2008. URL http://stacks.iop.org/0029-5515/48/i=2/a=024009.

[55] O. Schmitz, T. E. Evans, M. E. Fenstermacher, E. A. Unterberg, M. E. Austin, B. D. Bray, N. H. Brooks, H. Frerichs, M. Groth, M. W. Jakubowski, C. J.

Lasnier, M. Lehnen, A. W. Leonard, S. Mordijck, R. A. Moyer, T. H. Osborne, D. Reiter, U. Samm, M. J. Schaffer, B. Unterberg, and W. P. West. Resonant pedestal pressure reduction induced by a thermal transport enhancement due to stochastic magnetic boundary layers in high temperature plasmas. *Phys. Rev. Lett.*, 103:165005, Oct 2009. doi: 10.1103/PhysRevLett.103.165005. URL http://link.aps.org/doi/10.1103/PhysRevLett.103.165005.

[56] T. Eich, D. Reiser, and K.H. Finken. Two dimensional modelling approach to transport properties of the TEXTOR–DED laminar zone. *Nuclear Fusion*, 40 (10):1757, 2000. URL http://stacks.iop.org/0029-5515/40/i=10/a=307.

[57] F. Nguyen, P. Chendrih, and A. Grosman. Interaction of stochastic boundary layer with plasma facing components. *Nuclear Fusion*, 37(6):743, 1997. URL http://stacks.iop.org/0029-5515/37/i=6/a=I03.

[58] H. Stoschus, O. Schmitz, H. Frerichs, D. Reiser, M.W. Jakubowski, B. Unterberg, M. Lehnen, D. Reiter, U. Samm, and the TEXTOR team. Impact of rotating resonant magnetic perturbation fields on plasma edge electron density and temperature. *Nuclear Fusion*, 52(8):083002, 2012. URL http://stacks.iop.org/0029-5515/52/i=8/a=083002.

[59] M. W. Jakubowski, O. Schmitz, S. S. Abdullaev, S. Brezinsek, K. H. Finken, A. Krämer-Flecken, M. Lehnen, U. Samm, K. H. Spatschek, B. Unterberg, and R. C. Wolf. Change of the magnetic–field topology by an ergodic divertor and the effect on the plasma structure and transport. *Phys. Rev. Lett.*, 96:035004, Jan 2006. doi: 10.1103/PhysRevLett.96.035004. URL http://link.aps.org/doi/10.1103/PhysRevLett.96.035004.

[60] N Vianello, C Rea, M Agostini, R Cavazzana, G Ciaccio, G De Masi, E Martines, A Mazzi, B Momo, G Spizzo, P Scarin, M Spolaore, P Zanca, M Zuin, L Carraro, P Innocente, L Marrelli, M E Puiatti, and D Terranova. Magnetic perturbations as a viable tool for edge turbulence modification. *Plasma Physics and Controlled Fusion*, 57(1):014027, 2015. URL http://stacks.iop.org/0741-3335/57/i=1/a=014027.

[61] N. Vianello, G. Spizzo, M. Agostini, P. Scarin, L. Carraro, R. Cavazzana, G. De Masi, E. Martines, B. Momo, C. Rea, S. Spagnolo, M. Spolaore, M. Zuin, and the RFX-Mod Team. 3D effects on the RFX–mod boundary. *Nuclear Fusion*, 53(7): 073025, 2013. URL http://stacks.iop.org/0029-5515/53/i=7/a=073025.

[62] I.T. Chapman, D. Brunetti, P. Buratti, W.A. Cooper, J.P. Graves, J.R. Harrison, J. Holgate, S. Jardin, S.A. Sabbagh, K. Tritz, the MAST, NSTX Teams, and EFDA-JET Contributors. Three–dimensional distortions of the tokamak plasma boundary: boundary displacements in the presence of saturated MHD instabilities. *Nuclear Fusion*, 54(8):083007, 2014. URL http://stacks.iop.org/0029-5515/54/i=8/a=083007.

[63] P. Piovesan, D. Bonfiglio, F. Auriemma, F. Bonomo, L. Carraro, R. Cavazzana, G. De Masi, A. Fassina, P. Franz, M. Gobbin, L. Marrelli, P. Martin, E. Martines, B. Momo, L. Piron, M. Valisa, M. Veranda, N. Vianello, B. Zaniol, M. Agostini, M. Baruzzo, T. Bolzonella, A. Canton, S. Cappello, L. Chacón, G. Ciaccio, D. F. Escande, P. Innocente, R. Lorenzini, R. Paccagnella, M. E. Puiatti, P. Scarin, A. Soppelsa, G. Spizzo, M. Spolaore, D. Terranova, P. Zanca, L. Zanotto, and M. Zuin. RFX–mod: A multi–configuration fusion facility for three-dimensional physics studies. *Physics of Plasmas (1994-present)*, 20(5):056112, 2013. doi: http://dx.doi.org/10.1063/1.4806765. URL http://scitation.aip.org/content/aip/journal/pop/20/5/10.1063/1.4806765.

[64] M. Spolaore, N. Vianello, M. Agostini, R. Cavazzana, E. Martines, G. Serianni, P. Scarin, E. Spada, M. Zuin, and V. Antoni. Magnetic and electrostatic structures measured in the edge region of the RFX-mod experiment. *Journal of Nuclear Materials*, 390–391(0):448–451, 2009. ISSN 0022–3115. doi: http://dx.doi.org/10.1016/j.jnucmat.2009.01.132. URL http://www.sciencedirect.com/science/article/pii/S0022311509001548. Proceedings of the 18th International Conference on Plasma-Surface Interactions in Controlled Fusion Device Proceedings of the 18th International Conference on Plasma-Surface Interactions in Controlled Fusion Device.

[65] H. Y. W. Tsui, R. D. Bengtson, G. X. Li, H. Lin, M. Meier, Ch. P. Ritz, and A. J. Wootton. A new scheme for Langmuir probe measurement of transport and electron temperature fluctuations. *Review of Scientific Instruments*, 63(10):4608, 1992. doi: http://dx.doi.org/10.1063/1.1143683. URL http://scitation.aip.org/content/aip/journal/rsi/63/10/10.1063/1.1143683.

[66] P.C. Stangeby. *The interpretation of plasma probes for fusion experiments, in Plasma Diagnostic Surface Analysis and Interaction*. Academic Press, 1989.

[67] V. Antoni, D. Desideri, E. Martines, G. Serianni, and L. Tramontin. Plasma flow in the outer region of the RFX reversed field pinch experiment. *Nuclear Fusion*, 36 (11):1561, 1996. URL http://stacks.iop.org/0029-5515/36/i=11/a=I09.

[68] H. Ji, H. Toyama, K. Yamagishi, S. Shinohara, A. Fujisawa, and K. Miyamoto. Probe measurements in the REPUTE-1 reversed field pinch. *Review of Scientific Instruments*, 62(10):2326, 1991. doi: http://dx.doi.org/10.1063/1.1142294. URL http://scitation.aip.org/content/aip/journal/rsi/62/10/10.1063/1.1142294.

[69] E.J. Powers. Spectral techniques for experimental investigation of plasma diffusion due to polychromatic fluctuations. *Nuclear Fusion*, 14(5):749, 1974. URL http://stacks.iop.org/0029-5515/14/i=5/a=020.

[70] Paul H. Rutherford Robert J. Goldston. *Introduction to Plasma Physics*. Institute of Physics Publishing, 1995.

[71] G. Spizzo, M. Agostini, P. Scarin, N. Vianello, R. B. White, S. Cappello, M. E. Puiatti, M. Valisa, and the RFX-mod Team. Edge topology and flows in the reversed–field pinch. *Nuclear Fusion*, 52(5):054015, 2012. URL http://stacks.iop.org/0029-5515/52/i=5/a=054015.

[72] H.W. Müller, J. Adamek, R. Cavazzana, G.D. Conway, C. Fuchs, J.P. Gunn, A. Herrmann, J. Horaček, C. Ionita, A. Kallenbach, M. Kočan, M. Maraschek, C. Maszl, F. Mehlmann, B. Nold, M. Peterka, V. Rohde, J. Schweinzer, R. Schrittwieser, N. Vianello, E. Wolfrum, M. Zuin, and the ASDEX Upgrade Team. Latest investigations on fluctuations, ELM filaments and turbulent transport in the SOL of ASDEX Upgrade. *Nuclear Fusion*, 51(7):073023, 2011. URL http://stacks.iop.org/0029-5515/51/i=7/a=073023.

[73] Y. Suzuki, K. Ida, K. Kamiya, M. Yoshinuma, S. Sakakibara, K.Y. Watanabe, H. Yamada, and the LHD Experiment Group. 3D plasma response to the magnetic field structure in the Large Helical Device. *Nuclear Fusion*, 53(7):073045, 2013. URL http://stacks.iop.org/0029-5515/53/i=7/a=073045.

[74] Masaaki Yamada, Russell Kulsrud, and Hantao Ji. Magnetic reconnection. *Rev. Mod. Phys.*, 82:603–664, Mar 2010. doi: 10.1103/RevModPhys.82.603. URL http://link.aps.org/doi/10.1103/RevModPhys.82.603.

[75] Institute of Physics Publishing Nature Publishing Group. *Encyclopedia of Astronomy and Astrophysics*. Taylor and Francis, UK, 2001.

[76] Ellen G. Zweibel and Masaaki Yamada. Magnetic reconnection in astrophysical and laboratory plasmas. *Annu. Rev. Astron. Astrophys.*, 2009. doi: 10.1146/annurev-astro-082708-101726.

[77] E.N. Parker. Sweet's mechanism for merging magnetic fields in conducting fluids. *Astrophys. J.*, 62:509, 1957.

[78] Hantao Ji, Masaaki Yamada, Scott Hsu, and Russell Kulsrud. Experimental test of the Sweet–Parker Model of Magnetic Reconnection. *Phys. Rev. Lett.*, 80:3256–3259, Apr 1998. doi: 10.1103/PhysRevLett.80.3256. URL http://link.aps.org/doi/10.1103/PhysRevLett.80.3256.

[79] M Giubbilei, P Martin, and S Ortolani. A mechanism for plasma heating in driven relaxing magnetic field configurations. *Plasma Physics and Controlled Fusion*, 32 (5):405, 1990. URL http://stacks.iop.org/0741-3335/32/i=5/a=008.

[80] P. A. Cassak, M. A. Shay, and J. F. Drake. Scaling of Sweet–Parker reconnection with secondary islands. *Physics of Plasmas (1994-present)*, 16(12):120702, 2009. doi: http://dx.doi.org/10.1063/1.3274462. URL http://scitation.aip.org/content/aip/journal/pop/16/12/10.1063/1.3274462.

[81] D. Bonfiglio, S. Cappello, and D. F. Escande. Dominant electrostatic nature of the Reversed Field Pinch Dynamo. *Phys. Rev. Lett.*, 94:145001, Apr 2005. doi: 10.1103/PhysRevLett.94.145001. URL http://link.aps.org/doi/10.1103/PhysRevLett.94.145001.

[82] D. C. Robinson and R. E. King. *Proceedings of the 3rd International Conference on Plasma Physics and Controlled Nuclear Fusion Research, Novosibirsk*, page 263, 1969.

[83] Nathan Mattor. Scaling of magnetic turbulence with Lundquist number in relaxed state devices. *Physics of Plasmas (1994-present)*, 3(5):1578–1584, 1996. doi: http://dx.doi.org/10.1063/1.872016. URL http://scitation.aip.org/content/aip/journal/pop/3/5/10.1063/1.872016.

[84] H. Ji, S. C. Prager, and J. S. Sarff. Conservation of Magnetic helicity during Plasma Relaxation. *Phys. Rev. Lett.*, 74:2945–2948, Apr 1995. doi: 10.1103/PhysRevLett.74.2945. URL http://link.aps.org/doi/10.1103/PhysRevLett.74.2945.

[85] Chiara Piron. Study of magnetic reconnection events in fusion plasmas. Master's thesis, 2011.

[86] N. A. Crocker, G. Fiksel, S. C. Prager, and J. S. Sarff. Measurement of the current sheet during magnetic reconnection in a toroidal plasma. *Phys. Rev. Lett.*, 90:035003, Jan 2003. doi: 10.1103/PhysRevLett.90.035003. URL http://link.aps.org/doi/10.1103/PhysRevLett.90.035003.

[87] S. Choi, D. Craig, F. Ebrahimi, and S. C. Prager. Cause of sudden magnetic reconnection in a laboratory plasma. *Phys. Rev. Lett.*, 96:145004, Apr 2006. doi: 10.1103/PhysRevLett.96.145004. URL http://link.aps.org/doi/10.1103/PhysRevLett.96.145004.

[88] P. Piovesan, A. Almagri, B.E. Chapman, D. Craig, L. Marrelli, P. Martin, S.C. Prager, and J.S. Sarff. Filamentary current structures in the Madison Symmetric Torus. *Nuclear Fusion*, 48(9):095003, 2008. URL http://stacks.iop.org/0029-5515/48/i=9/a=095003.

[89] M Zuin, N Vianello, M Spolaore, V Antoni, T Bolzonella, R Cavazzana, E Martines, G Serianni, and D Terranova. Current sheets during spontaneous reconnection in a current–carrying fusion plasma. *Plasma Physics and Controlled Fusion*, 51(3):035012, 2009. URL http://stacks.iop.org/0741-3335/51/i=3/a=035012.

[90] R. B. Howell, J. C. Ingraham, G. A. Wurden, P. G. Weber, and C. J. Buchenauer. Asymmetric magnetic flux generation, m=1 activity, and edge phenomena on a reversed–field pinch. *Physics of Fluids (1958-1988)*, 30(6):1828–1838, 1987. doi: http://dx.doi.org/10.1063/1.866198. URL http://scitation.aip.org/content/aip/journal/pof1/30/6/10.1063/1.866198.

[91] G. Serianni, T. Bolzonella, R. Cavazzana, G. Marchiori, N. Pomaro, L. Lotto, M. Monari, and C. Taliercio. Development, tests, and data acquisition of the integrated system of internal sensors for RFX. *Review of Scientific Instruments*, 75(10):4338–4340, 2004. doi: http://dx.doi.org/10.1063/1.1789624. URL http://scitation.aip.org/content/aip/journal/rsi/75/10/10.1063/1.1789624.

[92] R. Lorenzini, D. Terranova, F. Auriemma, R. Cavazzana, P. Innocente, S. Martini, G. Serianni, and M. Zuin. Toroidally asymmetric particle transport caused by

phase–locking of MHD modes in RFX–mod. *Nuclear Fusion*, 47(11):1468, 2007. URL http://stacks.iop.org/0029-5515/47/i=11/a=008.

[93] M. Kočan, J.P. Gunn, S. Carpentier-Chouchana, A. Herrmann, A. Kirk, M. Komm, H.W. Müller, J.-Y. Pascal, R.A. Pitts, V. Rohde, and P. Tamain. Measurements of ion energies in the tokamak plasma boundary. *Journal of Nuclear Materials*, 415(1, Supplement):S1133 – S1138, 2011. ISSN 0022-3115. doi: http://dx.doi.org/10.1016/j.jnucmat.2010.08.036. URL http://www.sciencedirect.com/science/article/pii/S0022311510004277. Proceedings of the 19th International Conference on Plasma-Surface Interactions in Controlled Fusion.

[94] P. Staib. Probe measurements in the plasma boundary layer. *Journal of Nuclear Materials*, 111–112(0):109 – 122, 1982. ISSN 0022-3115. doi: http://dx.doi.org/10.1016/0022-3115(82)90193-3. URL http://www.sciencedirect.com/science/article/pii/0022311582901933.

[95] M. Komm, M. Kočan, D. Carralero, J. Stöckel, A. Herrmann, and R. Pánek. ExB analyzer for fast ion temperature in scrape–off layer of the ASDEX Upgrade and COMPASS tokamaks. to be published.

[96] G F Matthews. A combined retarding field analyser and ExB probe for measurement of ion and electron energy distribution in tokamak edge plasmas. *Journal of Physics D: Applied Physics*, 17(11):2243, 1984. URL http://stacks.iop.org/0022-3727/17/i=11/a=011.

[97] M. Komm, M. Kočan, D. Carralero, H.W. Müller, J. Stöckel, C. Rea, COMPASS team, and the ASDEX Upgrade Team. Fast measurements of ion temperature fluctuations in COMPASS and AUG scrape–off layer. *41st EPS Conference on Plasma Physics*, 2014.

[98] Carlos Hidalgo. Multi-scale physics and transport barriers in fusion plasmas. *Plasma Physics and Controlled Fusion*, 53(7):074003, 2011. URL http://stacks.iop.org/0741-3335/53/i=7/a=074003.

[99] G Serianni, A Murari, G Fiksel, V Antoni, M Bagatin, D Desideri, E Martines, and L Tramontin. Magnetic fluctuations and energy transport in RFX. *Plasma Physics and Controlled Fusion*, 43(7):919, 2001. URL http://stacks.iop.org/0741-3335/43/i=7/a=306.